CHAPTER 1

INTRODUCTION

This Chapter is an introduction to solid-state lasers and solid-state laser materials. In particular it is discussed, active media (host materials and active ions), pump sources and laser cavities that were used in this Thesis. Included is a historical overview of the laser action of Yb^{3+} *in monoclinic* $KRE(WO_4)_2$ *and some references to the laser action of* Er^{3+} *in* $KRE(WO_4)_2$.
Following this introduction it is outlined the main objectives of this work.

Table of contents

1.1 Overview of Solid-State Lasers (SSL)

The principle of the laser was first known in 1917, when *Einstein* described the theory of stimulated emission. However, it was not until the late 1940s that engineers began to use this principle for practical purposes. At the onset of the 1950's several engineers were working towards the harnessing of energy using the principal of stimulated emission. Among these engineers, were *Townes* (University of Columbia), *Weber* (University of Maryland) and *Prokhorov* and *Basov* (Lebedev Laboratories in Moscow). The conditions for laser action at optical frequencies were first described by *Schalow* and *Townes* [1] in 1958.

At this stage the engineers were working towards the creation of what was termed a MASER (Microwave Amplification by the Stimulated Emission of Radiation). This device amplified microwaves as opposed to light and soon found use in microwave communication systems. *Townes* and the other engineers believed it was possible to create an optical maser, a device for creating powerful beams of light using higher frequency energy to stimulate what was to be termed the lasing medium. Despite the pioneering work of *Townes* and *Prokhorov*, it was left to *Maiman* in 1960 to first demonstrate of laser action using a lasing medium of ruby (Cr^{3+}:Al_2O_3), a crystalline solid system that was stimulated using high energy flashes of intense light [2]. The next step in the development of solid-state lasers was the operation of trivalent uranium and divalent samarium in CaF_2 by *Sorokin* and *Stevenson* [3]. In 1961 *Snitzer* demonstrated [4] laser action in Nd^{3+} -doped glass. The first continuously operating crystal laser was reported in 1961 by *Johnson* and *Nassau* [5] using Nd^{3+}:$CaWO_4$. Since then laser action has been achieved from trivalent lanthanides (Nd^{3+}, Er^{3+}, Ho^{3+}, Ce^{3+}, Tm^{3+}, Pr^{3+}, Eu^{3+}, Yb^{3+}), divalent lanthanides (Sm^{2+}, Dy^{2+}, Tm^{2+}), transition metals (Cr^{3+}, Ni^{2+}, Co^{2+}, Ti^{3+}, V^{2+}), and the actinide ion U^{3+} embedded in various host materials. Optically pumped laser action has been demonstrated in hundreds of ion-host crystal combinations covering a spectral range from the ultraviolet to the mid-infrared.

Both *Townes* and *Prokhorov* were later awarded the Nobel Science Prize in 1964 for their endeavours.

The exceptionally favourable characteristics of the trivalent Nd^{3+} ion for laser action in solid-state laser materials were recognised at a relatively early stage. Nd^{3+} ion has a reasonably long fluorescence lifetime and narrow fluorescence linewidths in crystals and possesses a terminal state for the laser transition that is high enough above the ground state to allow continuous wave

(CW) operation at room temperature. This ion was therefore incorporated as a dopant in a variety of host materials such as glasses and crystals ($CaWO_4$, $CaMoO_4$, CaF_2, LaF_3, etc.), in an effort to use its great potential. However, most of these hosts displayed undesirable shortcomings, either for their intrinsic physical properties or for the way in which they interacted with the Nd^{3+} ions. Yttrium aluminium garnet, $Y_3Al_5O_{12}$ (known as YAG) was first explored by *Geusic* et al. [6] as a host for Nd^{3+} lasers. Nd^{3+}:YAG displayed the lowest thresholds for CW operation at room temperature of any then known host-dopant combination, and became a reference for solid-state laser materials from the very beginning.

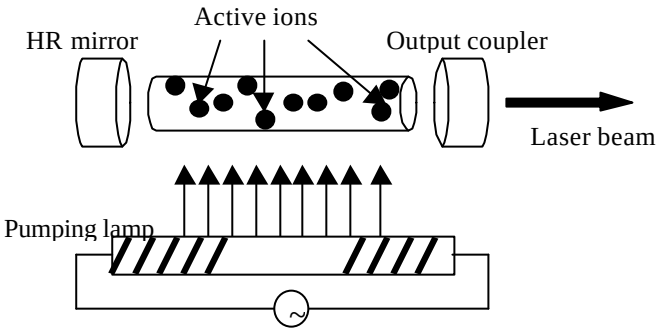

Figure 1.1 General scheme of a solid-state laser

The general scheme of a solid-state laser is shown in Fig. 1.1 composed by the laser cavity with two mirrors, the active medium with the active ions as generators of light and the pumping source. All these elements are discussed later for the case of laser operation of Yb^{3+} in $KRE(WO_4)_2$.

1.1.1 Stimulated emission

To understand the operation of a laser, some of the principles governing the interaction of radiation with matter have to be known.

Atomic systems such as atoms, ions and molecules can exist only in discrete energy states. A change from one energy level to another, called a transition, is associated with either the emission or the absorption of a photon. The wavelength of the absorbed or emitted radiation is given by Bohr's frequency relation

$$E_2 - E_1 = h\nu_{21} \qquad [1.1]$$

where E_2 and E_1 are two discrete energy levels, ν_{21} is the frequency, and *h* is Planck's constant. An electromagnetic wave whose frequency ν_{21} corresponds to an energy gap of such an atomic system can interact with it. To the approximation required in this context, a solid-state material can be considered an ensemble of very many identical atomic systems. At thermal equilibrium, the lower energy levels in the material are more heavily populated than the higher energy levels. A wave interacting with the substance will raise the atoms or molecules (in the case of solid-state lasers, the active elements are ions) from lower to higher energy levels and thereby experience absorption.

The operation of a laser requires that the energy equilibrium of a laser material be changed such that energy is stored in the ions of this material. This is achieved by an external pump source, which transfers electrons from a lower energy level to a higher one. The pump radiation thereby causes a 'population inversion'. An electromagnetic wave of appropriate frequency incident on a material in conditions of population inversion, will be amplified because the incident photons cause the ions in the higher level to drop to a lower level and thereby emit additional photons in an stimulated emission. As a result, energy is extracted from the atomic system and supplied to the radiation field.

Einstein stated that when a system is excited in conditions of population inversion, this will be capable of amplifying radiation at the frequency corresponding the energy level difference. The stimulated radiation has the same directional properties, same polarisation, same phase, and same spectral characteristics as the stimulating emission. These facts are responsible for the extremely high degree of coherence, which characterises the emission from lasers. In solid-state lasers, the energy levels and the associated transition frequencies result from the different quantum energy levels or allowed quantum states of the electrons orbiting about the nuclei of ions.

1.1.2 Continuous-wave (CW) and Pulsed lasers

Lasers may be operated in CW or Pulsed modes. With CW lasers, energy is continuously applied, or pumped into a lasing medium, producing a continuous laser output.

Quasi-CW operation (also called long-pulse or normal-mode operation) refers to a pulsed laser with a pulse duration long enough for all relevant parameters within the system to approach their

equilibrium values. Although the behaviour of the system is CW-like at the end of the pulse, it is, in general, quite different at the beginning of the pulse.

The most direct method of obtaining pulsed light from a laser is to use a CW laser in conjunction with an external switch or modulator that transmits the light only during selected short time interval. This simple method has two distinct disadvantages, however. First, the scheme is inefficient since it blocks (and therefore wastes the light) energy during the off-time of the pulse train. Second, the peak power of the pulses cannot exceed the steady power of the CW source.

More efficient pulsing schemes are based on turning the laser itself on and off by means of an internal modulation process, designed so that energy is stored during the off-time and released during the on-time. Energy may be stored either in the resonator, in the form of light that is periodically permitted to escape, or in the atomic system, in the form of a population inversion that is released periodically by allowing the system to oscillate. These schemes permit short laser pulses to be generated with peak powers far in excess of the constant power deliverable by CW lasers.

In a typical pulsed laser, intense pumping at the beginning of the energy pulse causes a population inversion, with high gain and creation of a standing wave in the optical cavity, which depletes the population inversion, and essentially stops the laser output. This process repeats itself until pumping ceases, thus, the laser output consists of a series of intense overlapping energy spikes. In a CW laser, this process essentially stabilizes into a steady state, resulting in true continuous output. For maximum efficiency, the composition and concentration of the lasing medium, as well as the construction of the laser cavity and mirrors must be optimised in a different way for pulsed or CW operation.

In this work, laser experiments in CW and pulsed regimes were performed on Yb:KLuW and KYbW cystals, respectively.

1.1.3 Solid-State Laser components

A solid-state laser, generally, consists of three components: an active medium with energy levels that can be selectively populated, a pump to excite the active medium and to produce population inversion between some of these levels and a resonant electromagnetic cavity that contains the active medium and provides feedback to amplify and maintain the coherence of the emitted light.

1.1.3.1 Active medium

The energy-level structure of a laser material plays an important role in obtaining inversion of population required for laser action. The main features can be understood through the familiar three-level or four-level idealisations as shown in Fig. 1.2.

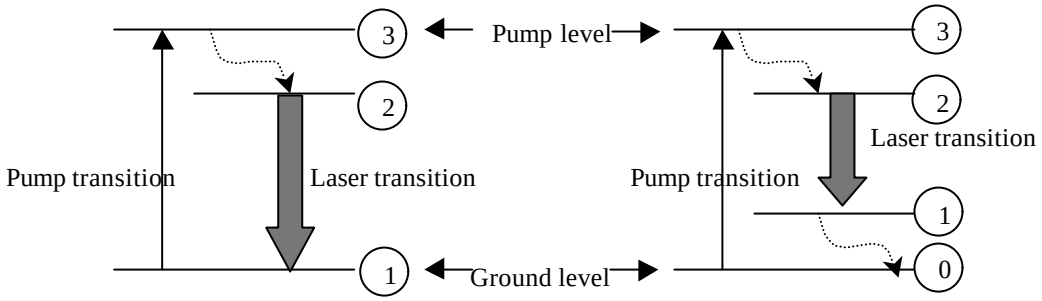

Figure 1.2 Simplified energy level diagram of a three-level laser (left). Simplified energy level diagram of a four-level laser (right)

Figure 1.2 (left) shows a diagram, which can be used to explain the operation of an optically pumped three-level laser, such as ruby. Initially, all ions of the laser material are in the lowest level 1. Excitation and absorption mechanisms populate level 3. In general, the pumping level 3, is actually made up of a number of bands, so that the optical pumping can be accomplished over a broad spectral range. Most of the excited ions are transferred by fast radiationless transitions into the intermediate level 2. In this process the energy lost by the electron is transferred to the lattice. Finally, the electron returns to the ground level by the emission of a photon. This last transition can be responsible for the laser action in favourable conditions. If pumping intensity is below laser threshold, atoms in level 2 predominantly return to the ground state by spontaneous emission. Ordinary fluorescence acts as a drain on the population of level 2. After the pump radiation is extinguished, level 2 is emptied by fluorescence at a rate that varies from material to material. When the pump intensity is above laser threshold, the decay from the fluorescent level consists of stimulated as well as spontaneous radiation; the stimulated radiation produces the laser output beam.

Since the terminal level of the laser transition is the highly populated ground state, a very high population must be reached in the level 2. For this reason, pumping of a three-level laser requires an extremely high-intensity source.

It is necessary, in general, that the rate of radiationless transfer from the uppermost level to the level at which the laser action begins be fast compared with the other spontaneous transition rates in a three-level laser. Therefore, the lifetime of the level 2 should be large in comparison with the relaxation time of the $3 \rightarrow 2$ transition.

Figure 1.2 (right) illustrates the four-level laser system. Note that a characteristic of the three-level laser material is that the laser transition takes place between the excited laser level 2 and the final ground state 1, the lowest energy level of the system. This leads to low efficiency. The four-level system avoids this disadvantage. The pump transition extends again from the ground state (level 0) to the absorption level 3. As in the case of the three-level system, the ions so excited will proceed rapidly to the level 2. The laser transition, however, proceeds now to a fourth, terminal level 1 above the ground state. From here the atom undergoes a rapid non-radiative transition to the ground level. In a true four-level system a material must possess a relaxation time between the terminal laser level and the ground level, which is fast compared to the fluorescent lifetime. In addition the terminal laser level must be far above the ground state so that its thermal population is small. If the energy gap between the lower laser level and the ground state is small, the material will be cooled to work as four-level lasers.

In a four-level system an inversion of the $2 \rightarrow 1$ transition can even occur at low pump power, and the high pump rate, necessary to maintain equilibrium population in the abovementioned three-level system, is no longer needed. In the most favourable case, the relaxation times of the $3 \rightarrow 2$ and $1 \rightarrow 0$ transitions in the four-level system are short compared with the spontaneous emission lifetime of the laser transition.

In this work, the lasing ion, Yb^{3+}, configures a quasi-three-level laser, which is discussed in Chapter 5.

1.1.3.2 Pump sources

Solid-state lasers are generally pumped optically. The pump source of a solid-state laser emits radiation in a spectral region that falls within the absorption bands of the lasing medium. Continuous or pulsed electrical energy is supplied to the pump source and converted into optical radiation. The light source and laser material are contained in a pumping arrangement that concentrates the light from the pump source onto the laser material.

The main objective in applying light sources for pumping lasers is to efficiently convert electrical energy into radiation and generate high-radiation fluxes in given spectral bands. The most efficient laser pump lamp will produce maximum emission at wavelengths that excite fluorescence in the laser material and produce minimal emission in all spectral regions outside the useful absorption bands. This may be from xenon flashlamps, which are probably larger by otherwise basically similar to those in photographic electronic flash units; via continuous arc xenon, krypton, or other discharge lamps, or more recently – and constantly growing in popularity – high power laser diodes or laser diode arrays. Of the various light sources used over the years to pump solid-state lasers, only flashlamps, CW arc lamps and laser diodes are today of practical interest.

Flashlamps are the method of choice where high peak power is required. None of the alternatives can produce the short, high intensity, burst of light needed to pump a solid-state laser for the generation of optical output pulses with peak power measured in Megawatts or more. While the xenon flashlamp is most common, other gas fills may be used to tailor the output spectrum to more closely match the absorption bands of the solid-state lasing medium.

In this work, a diode laser and Ti:sapphire laser were used as pump sources for laser operation of Yb:KLuW and KYbW.

Diode laser

At present, the most efficient pump source for solid-state lasers is the diode laser. The low power output, low packaging density, and extremely high cost of diode lasers prevented any serious applications for laser pumping until the mid 1980's.

With the rapid advances in laser-diode technology, there are now single diodes, 1-cm diode bars and stacked diode bars commercially available at power levels, which make these devices very attractive as pump sources for solid-state lasers. The emissions wavelengths of such lasers coincide very well with strong absorption bands of several lasing ions. Because of this excellent spectral match, the output from the diode pump is very efficiently utilised in producing a population inversion in the laser materials. Since the output of a diode laser is directional, the pump radiation can be transferred to the laser material with little loss, either in a close-coupled configuration, or by directing the radiation into the gain medium via optical elements. Moreover, because the diode pumps are partially coherent devices, their output beams may be tightly

focused or otherwise adjusted to spatially match the resonator modes of the solid-state laser.

The pumping of solid-state laser materials with single diodes or diode bars is a very rapidly emerging technology and new lasers and pumping configurations are reported.

The high pumping efficiency compared to flashlamps stems from the excellent spectral match between the laser-diode emission and the Yb^{3+} absorption band. A concomitant advantage derived from the spectral match between the diode-laser emission and the Yb^{3+} absorption band is a reduction in the amount of heat, which is deposited in the laser material. This reduces thermo-optic effects and therefore leads to better beam quality. In addition, the directionality of diode radiation allows designs with good spatial overlap between pump radiation and low-order modes in the resonator, which in turn, leads to a high-brightness laser output.

System lifetime and reliability is higher in laser diode pumped solid-state lasers as compared to flashlamps based systems. Laser-diode arrays exhibit lifetimes on the order of 10^4 h in CW operation and 10^9 shots in the pulsed mode. Flashlamp life is on the order of 10^8 shots, and about 500 h for CW operation.

Besides low repetition rate and CW operation covered also by flashlamps and CW arc lamps, quasi-CW laser diodes permit, in addition, pulsed operation of solid-state lasers in the regime from a few hundred Hz to a few kHz.

The absence of high-voltage pulses in diode-pumped lasers, high temperatures and UV radiation encountered with arc lamps lead to much more benign operating features of laser-diode-pumped systems. Furthermore, the high pump flux combined with a substantial UV content in lamp-pumped systems causes material degradation in the pump cavity and in the coolant, which lead to systems degradation and contribute to maintenance requirements.

The directionality of the diode output and the small emitting area, as compared to lamp pump sources, made it possible to design shole new classes of solid-state lasers, such as end-pumped systems, microchip lasers and fiber lasers. The flexibility of shaping and transferring the output beam from the pump source to the laser medium provides a great opportunity for the invention of new pump configurations and design architectures.

The most prominent laser materials, which are pumped with diode can also be pumped with flashlamp. However, a number of very useful materials such as Nd:YVO_4, Yb:YAG and Tm:YAG have only reached prominence as a result of diode pumps.

Depending on the output-power requirements of the laser and the particular pump configuration chosen, one can select a diode pump source from a number of standard commercial designs.

Ti:sapphire laser

The Ti:sapphire laser combines a broad tuning range of about 400 nm with a relatively large gain cross-section which is half of Nd:YAG at the peak of its tuning range. The energy level structure of the Ti ion is unique among transition-metal laser ions in that there are no *d*-state energy levels above the upper laser level. The simple energy-level structure ($3d^1$ configuration) eliminates the possibility of excited-state absorption of the laser radiation, an effect, which has limited the tuning range and reduced the efficiency of other transition-metal-doped lasers.

The broad, widely separated absorption and fluorescence bands are caused by the strong coupling between the ion and host lattice, and are the key to broadly tunable laser operation.

Besides having favourable spectroscopic and lasing properties, one other advantage of Ti:Al_2O_3 are the material properties of the sapphire host itself, namely very high thermal conductivity, exceptional chemical inertness and mechanical rigidity.

Titanium sapphire lasers have been pumped with a number of sources such as argon and copper vapour lasers, frequency doubled Nd:YAG and Nd:YLF, as well as flashlamps. Flashlamp pumping is very difficult to achieve in Ti:sapphire because a very high flux is required. The reason for that is the short fluorescence lifetime of 3.2 μs. Improvements in crystal quality which lead to the removal of residual absorption bands, in combination with special flashlamps have resulted in output energies of 3 J per pulse at 2% efficiency. Commercial Ti:sapphire lasers are pumped by argon lasers to obtain CW output, and by frequency-doubled Nd:YAG or Nd:YLF lasers for pulsed operation. In the CW mode, typical performance is close to 1 W output with a 5 W argon pump. Tuning ranges from about 700 nm to 1050 nm require several sets of cavity mirrors. For pulsed solid-state lasers as pump source, output energies range from a few mJ at repetition rates of around 1 kHz, to 100 mJ per pulse at 20 pps.

A very important application of Ti:sapphire lasers is the generation and amplification of femtosecond mode-locked pulses.

1.1.3.3 Laser cavity

Optical resonator

The efficiency in the transfer of radiation from the source to the laser element determines to a large extent the overall efficiency of the laser system. The pump cavity, besides providing good coupling between the source and the absorbing active material, is also responsible for the pump density distribution in the laser element which influences the uniformity, divergence, and optical distortions of the output beam.

In the development of solid-state lasers, many different optical designs have been employed to transfer the radiation from a light source to the active material.

Since the output beams of laser diodes can be shaped and focused, a major consideration is the design of a pump geometry, which maximises the overlap of the pumped volume with the volume occupied by a low-order resonator mode. The optimisation of the overlap is referred to as mode-matching. With the emergence of laser diodes as important pump sources for solid-state lasers, end-pumping has become a common technique in the design of low power solid-state lasers in front of side-pumped and face-pumped designs.

Typically two basic approaches have been followed in diode pumping of solid-state lasers, namely end-pumped and side-pumped configurations. In the end-pumped technique, pump radiation is introduced longitudinally into the active material, i.e. co-linear with the resonator axis. In the side-pumped configurations, which are similar in concept to flashlamp-pumped lasers, the radiation from the diode bars enters the active material transverse to the optical axis of the laser radiation. End-pumping is the more efficient method for generating diffraction-limited performance, as the pump radiation is spatially overlapped with the TEM_{00} lasing mode. Matching the high aspect ratio of the emitting area of diode bars to the intracavity mode size is a very challenging optical task and a number of beam shaping techniques have been developed. Although less efficient, side-pumping of laser rods and slabs is easily scaled and is therefore mainly employed for high-power systems. In side-pumping, the high aspect ratio of the emitting surface can easily be matched to the laser medium, and heat removal can be accomplished over a larger surface are which reduces thermally related problems.

Resonator mirrors

As with other types of lasers, the resonator in a solid-state laser will require mirrors at both ends. The high-reflective mirror (HR) may be dielectric, metal coated, or a corner or half-corner reflector, to name just a few possibilities depending on the lasing wavelength, presence of additional cavity optics (like a Q-swith), and applications. The output-coupler (OC) mirror will generally be either dielectric or resonant optic (one of its peak reflectances adjusted to coincide with the lasing line). Both mirrors are likely planar so there are no focused regions inside the gain medium. To focus the pump beam inside the gain medium, the folding mirrors are curved.

A maximum of output intensity will occur for a unique value of the output coupler reflectivity. The output coupling reflectivity is an interesting point for design parameters. For example, for higher gains (due, for example, to large stimulated-emission cross-sections) lower optimum reflectivities and higher output intensities are yielded, while perhaps higher internal loss also recommends lower optimum reflectivity.

The light emitted by most lasers contains several discrete optical frequencies separated from each other by frequency differences, which can be associated with different modes of the optical resonator. It is common practice to distinguish two types of resonator modes: 'longitudinal' modes that differ from one another only in their oscillation frequency and 'transverse' modes that differ from one another no only in their oscillation frequency, but also in their field distribution in a plane perpendicular to the direction of propagation. Corresponding to a given transverse mode are a number of longitudinal modes which have the same field distribution as the given transverse mode but which differ in frequency.

The spectral characteristics of a laser, such as linewidth and coherence length, are primarily determined by the longitudinal modes; whereas beam divergence, beam diameter, and energy distribution are governed by the transverse modes. In general, lasers are multimode oscillators unless specific efforts are made to limit the number of oscillating modes. The reason for this lies in the fact that a very large number of longitudinal resonator modes fall within the bandwidth exhibited by the laser transition, and a large number of transverse resonator modes can occupy the cross-section of the active material.

1.1.4 Issues in laser design

The design of a laser is dictated by many interdependent factors, including the requirements placed on the output beam (wavelength, spectral purity, tunability, divergence, polarisation, power, power stability), the operating environment (temperature, humidity, vibration, acceleration, externally applied forces), and practical considerations (size, cost, available power, pump-source characteristics). There is an increasingly large number of gain media, cavity designs, and pump configurations that have been employed in lasers, and several texts have been written on the subject of laser design. No one design is well suited to all applications; every laser is optimised for operation at one point in the multidimensional parameter space outlined above.

A very important issue in the design of many lasers is the extraction of heat from the gain medium. In the process of pumping the gain medium, heat is generated. As the temperature of the gain medium changes, so do its physical length and refractive index. Each of these contributes to changes in the optical length and resonant frequencies of the laser cavity (these changes are especially significant in miniature lasers where the active volume constitutes much of the resonator). Nonuniform heating results in a nonuniform refractive index and internal stress. Index gradients lead to thermal lensing, which changes the confocal parameters of the laser cavity and can destabilise an otherwise stable cavity. Internal stress leads to stress birefringence and, eventually, stress-induced fracture.

The optical pumping process in a solid-state laser material is associated with the generation of heat for a number of reasons: a) the energy difference of the photons between the pump level and the upper laser level is lost as heat to the host lattice and causes the so-called quantum defect heating; b) similarly, the energy difference between the lower laser level and the ground state is thermalised; c) since the quantum efficiency of the fluorescence processes involved in the laser transition is less than unity, heating due to quenching mechanisms takes place; and d) the broad spectral distribution of arc lamps or flashlamps is such that there is considerable absorption by the host material, mainly in the ultraviolet and infrared bands that is not transferred to laser radiation. Efficient heat removal, and the reduction of the thermal effects, which are caused by the temperature gradients across the active area of the laser medium usually dominate design considerations for high-average-power systems.

One of the advantages of diode-laser pumping for Yb^{3+} ions is that the waste heat dissipated in the laser medium is greatly reduced by the high efficiency of the pumping process. Quantum-defect

heating is reduced because the pump wavelength is closer to the laser-emission wavelength, and heating of the host material by pump radiation located outside the absorption bands of the active ions is completely eliminated.

Other issues that must be considered in high-power lasers are nonlinear optical effects and optical damage. The electrical field within the optical beam of a high-power laser can be large enough to damage optical components. This is particularly important in high-peak-power pulsed lasers. At optical intensities below the optical damage level, deleterious nonlinear optical interactions can still degrade the performance of the laser and even destroy the device.

The above sections were developed with the help of literature [7, 8, 9, 10, 11, 12].

1.2 Overview of Solid-State Laser Materials

Materials for laser operation must possess sharp fluorescent lines, strong absorption bands and reasonable high quantum efficiency for the fluorescent transition of interest. These characteristics are generally shown by solids (crystals or glasses), which incorporate small amounts of elements in which optical transitions can occur between states of inner of incomplete electron shells. In this connection, transition metals and rare-earth elements are interesting. The electrons involved in transitions in the optical regime are shielded by their outer shells from the surrounding crystal lattice, leading to narrow linewidth emissions spectra. The corresponding transitions are similar to those of the free ions. As well as a sharp fluorescence emission line, a laser material should possess pump bands within the emission spectrum of readily available pump sources.

The three principal elements leading to gain in a laser are:

The host material, with its macroscopic mechanical, thermal and optical properties and its unique microscopic lattice properties.

The activator/sensitiser ions, with their distinctive charge states and free-ion electronic configurations.

The optical pump source, with its particular geometry, spectral irradiance and temporal characteristic.

These elements are interrelated and must be selected self-consistently.

1.2.1 Host Materials

Solid-state host materials may be broadly grouped into crystalline solids and glasses. Many crystalline host materials have been investigated since the discovery of the ruby laser. The advantages of crystalline laser hosts over glasses are their higher thermal conductivity, narrower fluorescence linewidths, and, in some cases, their greater hardness. Their disadvantages, however, are their often poorer optical quality and doping homogeneity and their generally narrower absorption lines. The outstanding practical advantage of glass compared to crystalline materials is its strong capability for high-energy applications. In this work we focus on crystals as hosts for solid-state laser materials.

Several interactions between the host crystal and the additive ion restrict the number of useful material combinations. These include size disparity, valence and spectroscopic properties. Ideally, the size and valence of the additive ion should match those of the host ion it replaces, so as not to disturb the crystal lattice.

When selecting a crystal suitable for a laser ion host, the following key criteria must be considered.

i) The crystal must possess favourable optical properties. Variations in the refraction index lead to inhomogeneous propagation of light through the crystal. This results in poor beam quality.

ii) The crystal must possess mechanical and thermal properties that permit high-average-power operation without damaging the laser crystal. The most important parameters are thermal conductivity, hardness and fracture strength. The thermal expansion of the lattice is an important parameter in anisotropic crystals.

iii) The crystal must have lattice sites that can accept the dopant ions and have local crystal fields of symmetry and strength that are needed to induce the desired spectroscopic properties.

iv) It must be possible to scale the growth of the impurity-doped crystal while maintaining high optical quality and high yield. The greatest prospect for successful growth scaling seems to be for crystals that melt congruently at temperatures below 1300 ºC. This relatively low melting temperature enables a wide range of crucible materials and growth techniques to be used.

Other important properties to include are chemical stability, resistance to radiation-induced colour centres and ease of fabrication.

1.2.1.1 Monoclinic tungstates

$CaWO_4$ was the most popular material for Nd^{3+} before YAG became commercially available. The rare-earth substitutes for Ca, but only in the trivalent oxidation state, and hence charge compensation is needed. For optimum laser performance, it was better to substitute Na^+ for Ca^{2+} [13]. The material is very prone to fracture, even when well annealed, so considerable care is needed when laser rods are made from boules. Thermal conductivity is three-to-four times greater than that with glass.

Sodium rare-earth tungstates ($NaRE^{3+}(WO_4)_2$) have served as host materials for active ions. In these materials, which have similar properties to those of $CaWO_4$, half of the calcium atoms are randomly replaced with sodium and the other half are replaced with rare-earth. Laser action has been observed from Nd^{3+} in $NaGd(WO_4)_2$ and from $NaNd(WO_4)_2$.

The low-temperature phase of $KRE^{3+}(WO_4)_2$ crystals (where RE^{3+}= Y^{3+} and Ln^{3+}), which are object of this study, have a monoclinic structure and belong to the C2/c space group. The crystal structure of tungstates enables impurity ions to be introduced and these crystals to be used as hosts for laser-active elements. Their thermal, mechanical and optical properties make them suitable hosts for solid-state materials.

The laser properties of $KRE^{3+}(WO_4)_2$ doped with lanthanide ions were discovered in 1971 [14]. These crystals are convenient media for obtaining Stimulated Emission (SE) generation [15] and the Ln^{3+} ions in these hosts can also serve as sensitisers and deactivators [16]. Of all known inorganic laser materials, $KRE^{3+}(WO_4)_2$:Nd^{3+} single crystals provide the highest efficiency of SE generation at small pumping energies with both lamp [17] and laser-diode [18, 19] excitation. Monoclinic tungstates also have large nonlinear optical susceptibilities $\chi^{(3)}$, and can therefore be used in various laser experiments and applications that are based on the phenomenon of Stimulated Raman Scattering (SRS) [20, 21]. For example, a highly efficient room-temperature practical eye-safe self-SRS $KGd^{3+}(WO_4)_2$:Nd^{3+} laser was designed [22]. The observed Stokes shift of $\approx$ 900 cm^{-1} corresponds to the frequency of high-frequency vibrations of the covalent WO_4^{2-} group in the host. The discovery of SRS in $KRE^{3+}(WO_4)_2$:Ln^{3+} expands the spectral range of potential laser generation with these crystals. Monoclinic double tungstates have a very high degree of physical anisotropy, then polarised laser radiation can be generated.

1.2.2 Active Ions

In solid-state laser systems, the laser emissions can be produced by electronic transitions in the active ions. The active ions belong to the lanthanide and actinide series or are transition metals. In crystalline hosts, the active ions are placed in the host and substitute some ions of their own lattice.

The lanthanide ions are natural candidates to serve as active ions in solid-state laser materials because they exhibit a wealth of sharp fluorescent transitions ranging from the ultraviolet region to the near-infrared region of the electromagnetic spectrum. The ground state electronic configuration of a lanthanide atom comprises a core, which is identical to xenon, plus additional electrons in higher orbits. In xenon, the shells with quantum numbers n = 1, 2, 3 are completely filled. The shell n = 4 has its s, p and d subshells filled, whereas the 4f subshell, which is capable of accommodating 14 electrons, is completely empty. However, the n = 5 shell acquires its first 8 electrons, which fill the 5s and 5p orbits. Lanthanide elements begin with the filling of the inner vacant 4f orbits. In crystals, lanthanide ions are normally trivalent, but under appropriate conditions the valence state can also be divalent. When a trivalent ion is formed, the atom gives up its outermost 6s electrons, the atom also loses its 5d electron if it has one, if not, it loses one of the 4f electrons.

The fluorescence spectra of lanthanide ions arise from electronic transitions between levels of the partially filled 4f shell, which are well shielded by the filled 5s and 5p outer shells. As a result, emission lines are relatively narrow and the energy level structure varies only slightly from one host to another. The effect of the crystal field is normally treated as a perturbation on the free-ion levels. The perturbation is small compared to spin-orbit and electrostatic interactions among the 4f electrons. The primary change in the energy levels is a splitting of each of the free-ion levels (manifolds) in many closely spaced levels, which is caused by the Stark effect of the crystal field.

1.2.2.1 Ytterbium (Yb^{3+})

The past decade has witnessed a veritable revolution in the types and performance levels of solid-state lasers, largely due to the development of high-power (>50 W/cm), high-efficiency (>50%), high-temperature (>300 K) laser diodes and laser diode arrays. Such pump sources were first realised using AlGaAs active quantum wells emitting at ~808 nm, suitable for pumping neodymium -doped laser materials.

Compared to traditional broadband arc or flashlamps pump sources, a laser diode pump source possesses greatly increased spectral brightness, with an emission bandwidth of typically a few nanometers. The availability of such narrowband bright pump sources precipitated major advances in the design and performance of solid-state lasers. With conventional pump sources such as flashlamps, the threshold is very high which eliminated the Yb^{3+} -doped materials from any serious considerations. With the emergence of powerful InGaAs laser diodes, which match the absorption band of Yb^{3+}, several researchers recognised the potential of Yb^{3+} -doped materials.

Yb^{3+} doped materials are attractive as efficient active media because they have several important advantages over the widely used Nd^{3+}. For example, emission lifetime is 3-4 times longer, depending on the host, which increases the energy-storage time, the Stokes shift between absorption and emission (laser quantum defect) is considerably smaller, which reduces the thermal load, and the two-level electronic structure is extremely simple, which eliminates the possibility of unwanted competitive processes such as excited–state absorption and up-conversion. Also, laser efficiency is not degraded by concentration quenching, and a very high doping level is possible. This can considerably reduce the requirements to the beam quality of the laser diodes used for pumping. The Yb^{3+} ion is recognised as a potentially interesting dopant for diode-pumped solid-state lasers in the 1 µm region [23, 24, 25]. InGaAs diode lasers can be used to excite Yb^{3+} ions between 0.9 and 1.0 µm and have significant advantages over lamp-pumped solid-state lasers and the direct use of diodes. Moreover, compared with Nd-doped media, Yb^{3+}-doped media have broader emission bandwidths, most of which are sufficient to support subpicosecond pulses. Several Yb^{3+}-based femtosecond mode-locked oscillators, including Yb:glass [26, 27, 28], Yb:YAG [29], Yb:KGW [30] and $Yb:Ca_4GdO(BO_3)_3$ [31], have been demonstrated in recent years.

The low heating (low quantum defect), broad absorption at the InGaAs wavelength and long lifetime have raised the prospect of high power generation with good beam quality. The applications of Yb^{3+}-doped materials could be the same that for Nd -doped materials (e.g. Nd:YAG).

Ytterbium has the $[Xe]4f^{13}$ electronic configuration. From this, two energy levels -the excited state and the ground state- are derived. The Stark energy levels of ytterbium are comprised between 0 and 800 cm^{-1} for the ground state, and between 10180 and 10800 cm^{-1} for the excited

state. Due to the overlap in energy of the $^2F_{5/2}$ level of Yb^{3+} and the $^4I_{11/2}$ level of Er^{3+}, ytterbium ions are widely used as sensitisers of erbium emissions and other lanthanides like Ho^{3+}, Tm^{3+} and Pr^{3+}. Yb^{3+} has a very high absorption cross-section, which allows for the efficient population of erbium via energy transfer (see next section).

In $KRE^{3+}(WO_4)_2$:Ln^{3+} crystals, the Yb^{3+} ion efficiently replaces RE^{3+} ions because both their charge and ionic radii match. These tungstate hosts can substitute the RE^{3+} at very high concentrations, approaching or arriving to the stoichiometric structures. Examples are the laser active $KEr(WO_4)_2$ [32, 33, 34] and $KHo(WO_4)_2$ [26, 35, 36, 37]. Some laser architectures, such as the thin disk [38, 39, 40] and waveguide designs, [41, 42] can benefit from highly doped solid-state laser materials. The stoichiometric Yb^{3+} tungstate, $KYb(WO_4)_2$, (one of the interests of this study) is advantageous for these laser concepts and is particularly suited for diode laser pumping [43, 44, 45, 46, 47].

1.2.2.2 Erbium (Er^{3+})

When erbium is embedded in a solid, it generally assumes the trivalent Er^{3+} state, which has an electronic configuration [Xe]-$4f^{11}$. The 4f-shell of the Er^{3+} ion is not completely filled, which allows for different electronic configurations with different energies due to spin-spin and spin-orbit interactions. Radiative transitions between most of these energy levels are parity forbidden for free Er^{3+} ions. When Er^{3+} is incorporated in a solid, however, the surrounding material perturbs the 4f wave functions. This has two important consequences. First, the host material can introduce odd-parity character in the Er^{3+} 4f wave functions, which makes radiative transitions weakly allowed. Second, the host material causes Stark-splitting of the various energy levels, which broadens the optical transitions. With $KRE^{3+}(WO_4)_2$:Ln^{3+}, the Er^{3+} also replaces RE^{3+} ions, like Yb^{3+}.

The energy levels of erbium, in increasing levels of energy are (by Dieke) [48]: $^4I_{15/2}$, $^4I_{13/2}$, $^4I_{11/2}$, $^4I_{9/2}$, $^4F_{9/2}$, $^4S_{3/2}$, $^2H_{11/2}$, $^4F_{7/2}$, $^4F_{5/2}$, $^4F_{3/2}$, $^2H_{9/2}$, $^4G_{11/2}$, $^2G_{9/2}$, $^2K_{15/2}$, $^2G_{7/2}$, $^2P_{3/2}$, $^2K_{13/2}$, $^2D_{7/2}$, $^2D_{5/2}$ and $^2G_{9/2}$. Figure 1.3 shows a schematic diagram of the energy levels of ytterbium and erbium ions in $KRE^{3+}(WO_4)_2$.

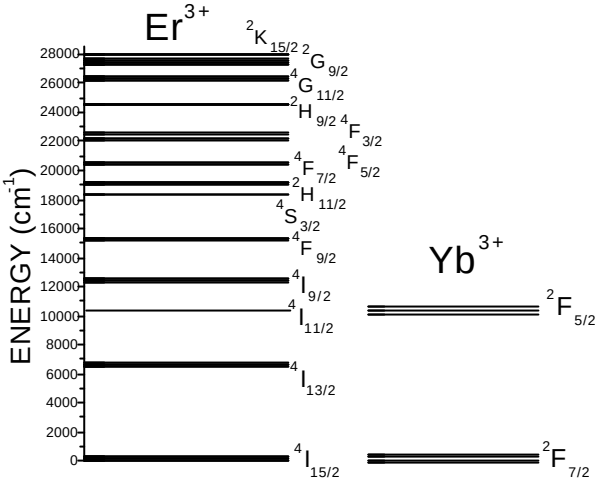

Fig 1.3 Schematic diagram of the energy levels of ytterbium and erbium in $KRE^{3+}(WO_4)_2$

Numerous studies of the absorption and fluorescence properties of erbium in various host materials have shown its potential as an active laser ion. Laser oscillation, arising from transitions between the $^4I_{13/2}$ level and the $^4I_{15/2}$, ground state of Er^{3+}, was observed mainly in the wavelength region 1.53 to 1.66 μm. Stimulated emission in the vicinity of 1.6 μm is of interest because, thanks to the great absorption of aqueous humour at this wavelength, it is safe for the eyes.

Light sources in the 2.8 μm [49] region, $^4I_{11/2} \rightarrow {}^4I_{13/2}$ transition, are particular interesting for medical applications [50, 51], thanks to the strong water absorption in this spectral region. As well as allowing from extremely precise cutting and ablation of water-containing tissues, light sources operating at 2.8 μm can reduce the burning of skin during surgery, decrease the use of anesthesia and shorten recovery time, especially in skin surgery and the cutting and removal of hard tissues such as tooth enamel and bone. Some examples of the laser action of erbium around 2.8 μm are found in [52, 53].

The green laser emission in erbium ($^4S_{3/2} \rightarrow {}^4I_{15/2}$) is also interesting for a wide range of applications, including colour displays, optical data storage, biomedical diagnostics, sensors and undersea optical communications. The population of the $^4S_{3/2}$ level is achieved by up-conversion. In general, the up-conversion is achieved via the so-called frequency up-conversion mechanism first investigated by Auzel [54]. This process involves either sequential or multiphoton stepwise excitation and energy transfer between rare-earth ions in solids and the subsequent emission of

photons with energies above those of the excitation photons. The green laser emission of erbium was achieved in references [55] [56]. Host materials of erbium have included YAG [57], YLF [58], $YAlO_3$ [59], LaF_3 [60], $CaWO_4$ [61], CaF_2 [62], and various glasses [63, 64].

For technological applications and basic research, it is important to study up-conversion phenomena in novel crystals and glasses, because they can provide compact, room-temperature light sources operating in the blue spectral region that are not available from conventional lasers. Currently there is interest in developing compact short-wavelength laser sources for display and data-storage applications. Promising approaches for these applications are wide-gap semiconductor diode lasers [65], harmonic generation by phase matching [66] or quasi-phase matching [67], and up-conversion lasers in bulk media [68] and fibres [69]. However, wide-gap semiconductors have growth and doping problems that have so far prevented practical applications at room-temperature by current injection. Harmonic generation requires critical alignment in bulk crystals and suffers reduced efficiencies in fibres and slab waveguides. Up-conversion lasers depend on complex internal dynamics to upgrade photon energy by mechanisms that are still the subject of intense study. Many questions still need to be answered due to the limitations of these various approaches. Of the various nonlinear processes that enable emissions into the visible region under an infrared excitation, the APTE process (*Addition de Photons par Transfert d'Energie*), discovered by Auzel [70, 71], is the most efficient.

In initial experiments with up-conversion lasers, efficiencies were low and they only operated at cryogenic temperatures. However, there are many up-conversion mechanisms, and highly efficient, room-temperature CW operation is undoubtedly achievable in suitable media and with suitable techniques. High efficiency and room-temperature operation have so far only been demonstrated only under separate circumstances in selected laser crystals [72, 73, 74, 75, 76] and fibres [69, 77], respectively.

1.2.2.3 Energy transfer between Yb^{3+} and Er^{3+} ions

Until the mid-1960s, all energy transfers (ETs) between rare-earth ions had the sensitiser (or donor) ion in one of its excited states, while the activator (or acceptor) ion was in its ground state. The energy accumulated by the sensitiser was therefore transferred to the activator. This conventional ET explains sensitised fluorescence as well as concentration quenching. Then, in 1966, it was proposed that ET promoting the acceptor ion in an excited state might be followed by

Excited State Absorption (ESA) of the pump photon to promote the acceptor ion into a higher excited state [70]. Or that another type of ET might occur where both the sensitiser and activator ions are in one of their excited states prior to ET [71], thus also leading to possible fluorescence at a higher frequency than the excitation beam frequency. These studies were carried out, respectively, using materials codoped with Yb^{3+}/Er^{3+} or Yb^{3+}/Tm^{3+} with the aim of producing more efficient IR quantum counters. With the same aim, other authors independently performed analogous experiments but suggested a different interpretation involving a cooperative process [71]. The different types of energy transfer up-conversion (ETU) processes described in the literature are schematised in Fig. 1.4.

Cases *a*, *b* and *c* in Fig. 1.4 did not involve any cooperative effect. Case *a* is a conventional ET between the sensitiser (excited state) and the activator (ground level) that promotes it to its excited state 2. ESA then occurs from state 2 of the acceptor ion and promotes it to the higher excited state 3. Case *b* is called Successive Energy Transfers. Here, only the sensitiser ion absorbs photons of the incident flux. After that, the activator ion is promoted to its excited state 2 by a first ET, then promoted to its excited state 3 by a second ET. Case *c* corresponds to Cross Relaxation Up-conversion. In fact, Cross Relaxation (CR) usually refers to all types of ET occurring between identical ions. If the sensitiser and the activator are identical ions, photons of the incident flux are absorbed by the sensitiser and by the activator, which lead to these two ions in their excited state 2. An ET then promotes the activator ion in its state 3 while the sensitiser goes down to a lower energy state. For these three cases (a, b and c), further ETs from the sensitiser to the activator may occur to populate higher energy levels of the activator [78].

Cooperative effects take place when more than one centre participates in the elementary process of sensitisation or luminescence. In cooperative sensitisation (case *d*), the energy accumulated by two excited ions is given in one transfer to an ion, which reaches a high excited state. If there is emission in a single process of one photon from two excited interacting ions (Fig. 1.4 (e)), there is cooperative luminescence with a virtual level.

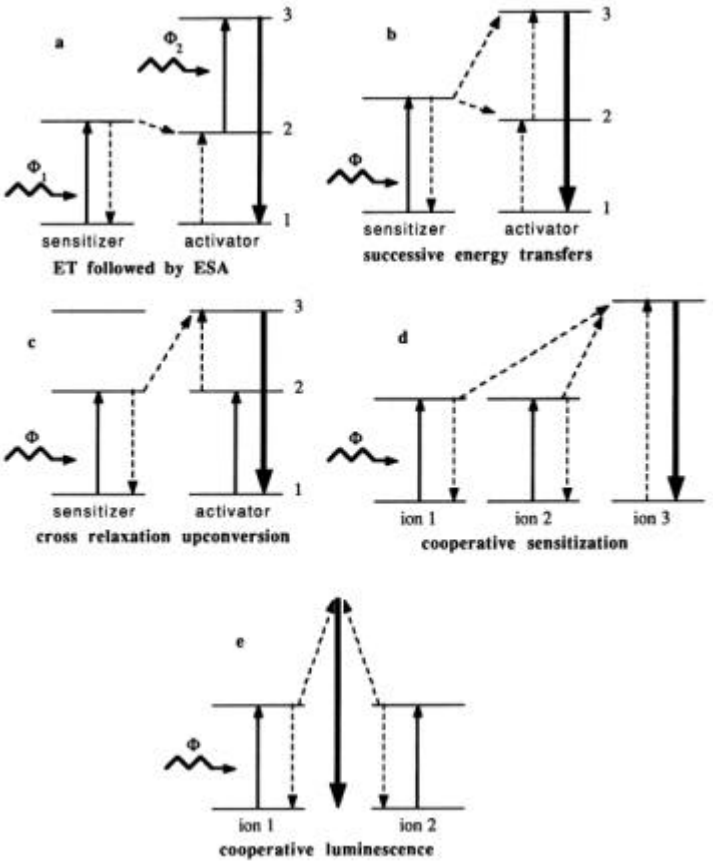

Fig 1.4 General energy schemes related to ETU processes

1.3 Overview of the Yb^{3+} and Er^{3+} -doped monoclinic $KRE(WO_4)_2$ lasers

This section is a bibliographical compilation of Yb^{3+} -doped $KRE(WO_4)_2$, Er^{3+} -doped $KRE(WO_4)_2$, and Yb^{3+},Er^{3+} -codoped $KRE(WO_4)_2$ lasers. Starting with ytterbium lasers in 1997, room-temperature lasing near 1025 nm was demonstrated in $Yb:KGd(WO_4)_2$ and $Yb:KY(WO_4)_2$, under Ti-sapphire and InGaAs diode laser under CW and pulsed laser pumping [79]. In 1999, the CW laser action of $Yb:KGd(WO_4)_2$ and $Yb:KY(WO_4)_2$ was also demonstrated at 1026-1044 nm under pumping by a 980 nm fibre-coupled InGaAs laser diode [80]. Also in 1999, the numerical simulation of Kerr lens mode locked laser operation of $Yb:KY(WO_4)_2$ determined that the

shortest pulse duration was approximately 200 fs [81]. In 2000, Demidovich et al. determined how the Yb concentration affected the laser properties of Yb:$KY(WO_4)_2$. These authors studied 5%, 10% and 20% Yb -doped crystals, achieving CW and Q-switched laser operation under diode laser pumping [82]. At the same time, Rotyliano et al. [83] investigated the laser performances of Yb:$KY(WO_4)_2$ and Yb:$KGd(WO_4)_2$ in order to optimise the Yb concentration while reducing crystal thickness.

Diode-pumped passively Q-switched Yb:$KGd(WO_4)_2$ with Cr^{4+}:YAG and V:YAG saturable absorbers were also reported in 2000. For the Cr^{4+}:YAG saturable absorber, Raman conversion of the fundamental laser emission was demonstrated and Q-switches 3.4 μJ pulses with a pulse width of 85 ns were obtained at 1033 nm fundamental wavelength and 0.4 μJ pulses with a pulse width of 20 ns were produced in a first Stokes at 1139 nm [84]. For V:YAG saturable absorber, laser emission at two wavelengths was simultaneously obtained due to Raman conversion of fundamental laser emission in the laser crystal [85]. In 2001, H. Liu et al. presented a directly diode-pumped regenerative amplifier for Yb:$KGd(WO_4)_2$ [86] and for Yb:$KY(WO_4)_2$ [87]. High power Yb:$KGd(WO_4)_2$ and Yb:$KY(WO_4)_2$ thin disk laser operation was demonstrated [88]. A pulse duration of 176 fs at 1.1 W of average output power was obtained with a mode-locked Yb:$KGd(WO_4)_2$ rod laser end-pumped by two high brightness diodes. For the first time, a self-starting mode-locked Yb:$KY(WO_4)_2$ laser based on the Kerr-lensing effect was presented [89]. In 2002, passive mode-locking was presented for Yb:$KGd(WO_4)_2$ [90]. Pulses as short as 150 fs and an average output power of 1.5 W were achieved using a 15 W fibre-coupled laser diode pumping and a semiconductor saturable absorber mirror (SESAM). For Yb:$KY(WO_4)_2$, pulses of 101 fs at an output power of 100 mW with tapered diode laser pumping were achieved [91]. Raman self-frequency conversion in Yb:$KY(WO_4)_2$ in the Q-switched regime was observed [92]. Also in 2002, a Yb:$KGd(WO_4)_2$ femtosecond system with performances that satisfied the requirement for real world applications was presented [93]. This system produced 150 μJ, 420 fs pulses at multi-kilohertz repetition rates. It used only one 2 W diode for the oscillator and one 15 W diode for the amplifier, and exhibited excellent short- and long-term stability. A highly efficient and low-threshold passively mode-locked femtosecond Yb:$KY(WO_4)_2$ laser pumped by an InGaAs narrow-stripe laser diode was demonstrated in 2003 . Near-transform limited pulses of 123 fs at 1047 nm were produced at an average mode-locked power of 107 mW for only 308 mW of

incident pump power. An optical-to-optical conversion efficiency of 35% was achieved and the corresponding electrical-to-optical efficiency exceeded 14%. CW lasing of $KYb(WO_4)_2$ crystals was presented in [45,94].

In this study, CW laser action involving Yb^{3+} in $KLu(WO_4)_2$ and pulsed laser action in stoichiometric Yb^{3+} tungstate ($KYb(WO_4)_2$) are presented as new promising laser systems.

The flash-lamp-pumped laser performance of Er^{3+} -doped $KY(WO_4)_2$ crystals is reported in the references [15, 32,95]. In 1977, A.A. Kaminskii reported [96] the laser action of Er^{3+} -doped $KY(WO_4)_2$ crystals, in which the laser wavelength was 2.7 μm. In 1978 these authors extended [15] the laser action to other wavelengths (0.85, 1.73 and 2.8 μm). In 1977, Er^{3+} -doped $KGd(WO_4)_2$ also showed laser action at 0.85, 1.73 and 2.7-2.8 μm [97]. In 1979, Er^{3+} -doped $KLu(WO_4)_2$ laser was also reported [98] at wavelengths of 1.73 and 2.8 μm.

In 1997 and 1998, co-doped Er^{3+},Yb^{3+}:$KY(WO_4)_2$ showed 1.54 μm laser action under pumping by both Ti:sapphire and InGaAs laser diodes [99, 100]. A maximum output power of 2.8 mW and a slope efficiency of about 1% was obtained at 1540 nm. The low efficiency of the 1.5 μm Er^{3+},Yb^{3+}:$KY(WO_4)_2$ -laser may be due to strong up-conversion losses. In 2003, Er^{3+},Yb^{3+}:$KGd(WO_4)_2$ was used in the CW and giant pulse train generation of diode pumped eye-safe microlasers [101].

Objectives

In the previous sections it was discussed the relative importance of the monoclinic phase $KRE(WO_4)_2$ (RE = Y^{3+} and Ln^{3+}) crystals in the field of solid-state lasers. It was also presented Yb^{3+} and Er^{3+} ions as suitable laser emitters for several interesting applications and with the advantages of diode-pumping and up-conversion mechanisms.

The objectives of this Doctoral Thesis are the crystal growth of the $KRE(WO_4)_2$ (RE = Gd^{3+}, Y^{3+}, Yb^{3+}, Er^{3+} and Lu^{3+}) un-doped, Yb^{3+} single doped, Er^{3+} single doped and Yb^{3+},Er^{3+} co-doped materials at several dopant concentrations. The intention is also to analyse the compositional, structural and morphological features of the crystals. The optical characterisation of the hosts, the spectroscopic study of the active ions and the laser action of Yb^{3+} in continuous wave and pulsed regimes are the most accurately studied objectives.

To meet the first objective, it was studied the solubility conditions. This was to establish the suitable solvent and the suitable solvent/solute ratio for crystal growth. The structure was determined with small crystals obtained by spontaneous nucleation. To grow the crystals for optical characterisation, it was used the Top-Seeded-Solution Growth method. Some of the parameters studied in the crystal growth experiments were the temperature of saturation, the cooling ratio and the introduction of dopants in the solution.

For the optical characterisation of the hosts, it was determined the transparency window of the crystals to know the spectral region in which the crystals can be transparent for exciting and emitting radiation, the principal optical axes of the crystals and the refractive indexes along the principal axes as a function of wavelength.

Spectroscopic characterisation involved optical absorption experiments with polarised light between room and cryogenic temperatures, optical emission in the ultraviolet, visible and infrared regions, also at both temperatures and the lifetime measurement of the emitting levels of both Yb^{3+} and Er^{3+} ions in the $KRE(WO_4)_2$ (RE = Gd^{3+}, Y^{3+}, Yb^{3+}, Er^{3+} and Lu^{3+}) hosts.

It was used numerical simulations to determine the interesting spectroscopic parameters such as radiative transition probabilities and the emission cross-section of the main emissions. For example, it was used the Judd-Ofelt theory to determine the probability of the radiative transitions and radiative lifetime, etc, the McUmber and Füchtbauer-Ladenburg methods to calculated the

emission cross-section of the 1.0 μm emission of Yb^{3+} and the 1.5 μm and 550 nm emissions of Er^{3+}.

Finally, the study is also motivated by the achievement of the laser action of the Yb^{3+} transition around 1.0 μm in the KYbW (pulsed laser operation) and Yb^{3+} -doped KLuW crystals (CW laser operation).

CHAPTER 2

EXPERIMENTAL TECHNIQUES

In this Chapter it is summarised the experimental techniques used in this work. It is presented an overview of the theoretical base and a description of the procedures involved in each technique. It is described the experimental equipment and illustrated the systems used to grow the crystals and characterise them optically and spectroscopically. The facilities described in this Chapter are available at FiCMA (Physics and Crystallography of Materials group of the Rovira i Virgili University, Spain), Servei de Recursos Científics (Rovira i Virgili University), Servei de Recursos Científico-Tècnics (University of Barcelona, Spain) and the Max-Born Institute for Non-linear Optics and Ultrafast Spectroscopy (Berlin, Germany).

Table of contents

2.1 Crystal growth from High-Temperature Solutions (HTS)

The greatest advantage of crystal growth from high temperature solutions (or flux growth) is that one can crystallise materials, which cannot be obtained in single crystal form by any other method. Flux growth methods, which allow the crystals to grow before the melting temperature is reached, are used when the crystals melt incongruently or when there is a phase transition before melting. The components of the final desired materials are dissolved in a solvent[102].

This method is based on the concepts of solubility and supersaturation. At a given temperature, a limited amount of a substance dissolves in a particular solvent. The amount dissolved defines the solubility at that temperature. If a saturated solution is prepared at a certain temperature and then cooled to a lower temperature, it contains more salt than is permitted by the solubility at the lower temperature. The same happens if some of the solvent is allowed to evaporate: the solution is now in the supersaturated state, which is a metastable state and, with a slightest induction, the extra salt precipitates. If a seed crystal is introduced into the solution, the substance precipitating from the solution grows around the seed crystal to form a larger single crystal. In the absence of a seed, even dust particles provide a nucleus for crystal growth. Conductive to the growth of a crystal are a slow rate of growth, the prevention of multiple nucleation and a good control of temperature.

Crystallisation can be performed in air or any other suitable atmosphere. Crystal growth is possible even if very little is known about the crystallization conditions. For this reason, this method is used as a preliminary one, to obtain new materials for the first time in single crystal form, so that their physical and chemical properties can be investigated.

2.1.1 Top-Seeded Solution Growth (TSSG)

Top-Seeded Solution Growth (TSSG) is a flux growth technique that is often used to grow crystals from high temperature solutions [103]. The difference between TSSG and other flux techniques is that crystals grow in a crystal seed placed in contact with the surface of the solution. The crystal seed can, if required, be crystallographically oriented to grow along a particular crystallographic direction. When the solution is cooled slowly, the crystal starts to grow in the supersaturated solution and continues to grow while the temperature decreases steadily. Optionally, one can pull the crystal while it grows to obtain larger crystals. To avoid secondary nucleation, the crystal seed should be at the coldest spot in the flux and convection, by rotating

either the crystal or the crucible, must be good[104]. In this study it was rotated the crystal but did not pull it. With this method, inclusion-free single crystals were obtained whose size is suitable for further investigations.

Vertical tubular furnaces with Kanthal heating elements were used. Each furnace was equipped with a temperature controller-programmer and control thermocouples. The furnaces are thermally isolated with firebricks and have a useful thermal zone 10 cm in diameter and around 50 cm in length.

Two kinds of thermocouples are used to monitor the crystal growth process. The control thermocouple usually comes with the furnace and is connected to the temperature controller, while the monitoring thermocouple can measure the temperature in various places in the heating chamber. We used an S-type thermocouple Pt / Pt - Rh 10 % located in the centre of the furnace near the heating resistances to ensure stable and reliable measurement of the temperature. The monitoring thermocouple was used to determine the difference in temperature between the control thermocouple and the surface of the solution where the crystal seed was placed. The monitoring thermocouple was also used to check the thermal axial and radial profile of the solution. The temperature gradient inside the solution is crucial to guaranteeing the quality of the crystals.

The temperature controller was connected to a thyristor to control the power supplied to the furnace. Depending on the slow-cooling program used, the furnace was controlled by a Eurotherm 818P (minimum cooling ramp of 0.1 Kh^{-1}) or a Eurotherm 903P (minimum cooling ramp of 0.01 Kh^{-1}).

The shape and material of the crucible depend on the temperature and solution used. Usually, when crystallisation takes place in the air, crucibles made of pure Pt should be used. The so-called analytical crucibles made of Pt and a small addition of Th can also be used, but their lifetime is much shorter than that of pure Pt crucibles. In the presence of O_2, pure Pt melts at 2045 K. Therefore, Pt can safely be used up to 1780 K. We used pure Pt crucible because of the extremely low reactivity with the oxides used as predecessors of the crystals. We used small conical pure Pt crucibles of 25 cm^3 for preliminary experiments to minimise the amount of chemicals needed. Once the growth strategy was well established, we used larger (125 cm^3) crucibles to obtain larger single crystals.

The crucible is supported inside the furnace by a mobile alumina column that can be displaced in order to accurately locate the crucible in the right zone of the furnace.

Figure 2.1 shows the thermal part of the crystal growth equipment.

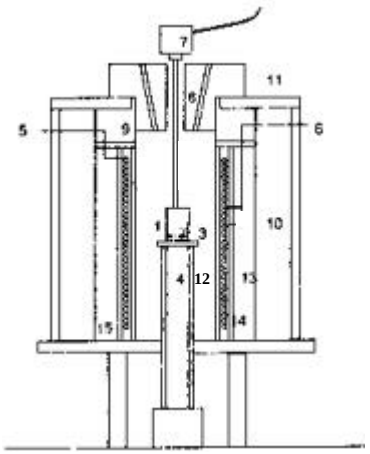

1.-Platinum crucible.
2.-Seed's support.
3 and 4.-Crucible's support.
5.-Current entrance.
6.-Control thermocouple.
7.- Seed rotor system.
8.- Furnace's topper.
9.- Thermal isolating brick.
10.-Thermal isolating wool.
11.- External steel isolating.
12 and 13.- Internal and external alumina tube.
14.- Kanthal wire.
15.- ceramic isolating.

Figure 2.1 Schematic view of the thermal part of the crystal growth system

Figure 2.2 shows the mechanical part of the crystal growth system. This comprises a vertical metal structure that is extremely rigid and stable and that enables the crystal seed to be vertically displaced and rotated. The crystal seed is attached to an alumina rod laced with Pt wire. We used a Mitutoyo micrometer to measure the changes in the length of the crystal seed to an accuracy of 0.01 mm in order to accurately determine the saturation temperature.

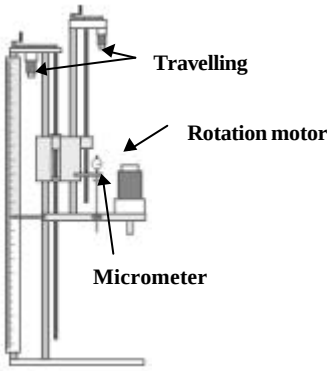

Figure 2.2 Mechanical part of the crystal growth system

These furnaces are available at the FiCMA (Physics and Crystallography of Materials group) of the Rovira i Virgili University in Tarragona (Spain).

2.2 Concentration measurement of dopant elements

The dopant concentration in the crystals was measured by Electron Probe Microanalysis (EPMA). This technique analyses the characteristic X-ray wavelengths emitted by the chemical elements under the effect of an electron beam. These are used to determine the chemical composition of very small regions in solid samples [105].

Elemental analysis with an electron probe requires measurement of the X-ray intensity of the elements. Most compounds have many elements, so a specific element's X-ray needs to be differentiated from the others. Since X-rays have wavelengths and intensity, they can be dispersed. This is similar to a prism dispersing visible light into a rainbow of wavelengths.

Electron probes can be fitted with X-ray detectors, which can discriminate either wavelength or intensity. Wavelength-discriminating X-ray detectors are the most quantitative, that is, their signal-to-noise ratio is high and they have excellent wavelength resolution. The principle behind Wave Dispersive X-ray Spectrometers (WDS) involves Bragg geometry and a crystal of known *d*-spacing. Also, the spectrometer needs to change its geometry in order to tune to a specific wavelength. Generally, an instrument has several WDS detectors installed, each of them with a different crystal, so a range of elements can be covered by the spectrometer's Bragg geometry. The crystals most often used are Lithium fluoride 200 (LIF), Pentaerythritol 002 (PET), Thallium acid phthalate 1011 (TAP) and PC1 (multi-alternating layers of light/heavy elements). With these crystals, the wavelength range covered 1-24 Å. This means that we could record *K*-lines for elements with atomic number (*Z*) between 9 and 35, *L*-lines for elements with *Z* less than 83 and all *M* lines.

Quantitative analysis requires corrections to the raw data such as deadtime, background and instrumental drift to be made before the matrix corrections for inter-element effects. The corrected intensity ratio of an element's X-ray line is not directly proportional to its concentration because the ratios are affected by X-ray absorption, secondary fluorescence, electron backscattering and the electron stopping power of the sample. Several methods take these factors into account and determine concentrations.

We used a Cameca SX-50 Microprobe Analyser operating in wavelength dispersive mode at 25 kV accelerating voltage and 40 nA beam current. This equipment is available at the *Servei de Recursos Científico-Tècnics* of the University of Barcelona (Spain).

Table 2.1 shows the measurement conditions used to analyse the dopant concentration in $KRE(WO_4)_2:Ln^{3+}$ single crystals.

Table 2.1 *Measurement standards used in EPMA analysis*

Element	Line	Spectrometer crystal	Standard
W	M_α	TAP	KREW
K	K_α	PET	KREW
Gd	L_α	LIF	KGdW
Y	L_α	LIF	KYW
Yb	M_α	TAP	REE3
Er	L_α	LIF	REE1
O	K_α	PC1	KGW
Lu	L_α	LIF	KLuW

2.3 Differential Thermal Analysis (DTA)

Differential Thermal Analysis (DTA) can be defined formally as a technique for recording the difference in temperature between a substance and a reference material against either time or against temperature as the two specimens are subjected to identical temperature regimes in an environment that is heated or cooled at a controlled rate.

In DTA, the difference in temperature between a reactive sample and a non-reactive reference is determined as a function of time and temperature. This provides useful information about the temperatures, thermodynamics and kinetics of reactions.

The key features in differential thermal analysis equipment are a sample holder comprising thermocouples, sample containers and a ceramic or metallic block, a furnace, a temperature programmer and a recording system.

The sample holder consists of one thermocouple for the sample and one for the reference, generally surrounded by a block to ensure heat is evenly distributed. The sample is contained in a small crucible designed with an identity on the base to ensure a snug fit over the thermocouple bead. The crucible can be made of materials such as Pyrex, silica, nickel or platinum, depending on the temperature and nature of the tests. Pt crucibles were used. To avoid contamination and degradation, the thermocouples should not be placed in direct contact with the sample, though in this way sensitivity may be compromised.

The furnaces should provide a stable and sufficiently large hot-zone and must have a low response time in order to accurately follow the thermal program. To obtain constant heating rates,

a temperature programmer is essential. The recording system must have a low inertial to faithfully reproduce variations in the experimental set-up.

Care must be taken when selecting the experimental parameters. For example, specimen environment, composition, size and surface-to-volume ratio all affect powder decomposition reactions but may not affect solid-state phase changes. Experiments are frequently performed on powders, so the data obtained may not be representative of bulk samples, where the transformations can be controlled by the build-up of strain energy. The packing state of any powder sample is important in decomposition reactions and can lead to large variations between apparently identical samples. The information provided by the equipment differentiates between endothermic or exothermic events that have no associated weight change (melting and crystallisation) and those that have (degradation).

We used an SDT 2960 analysis instrument from TA Instruments, available at FiCMA, operating between room temperature and 1773 K. Temperature accuracy was ±1 K, temperature precision was ±0.5 K, weight sensitivity was 0.1μg, weight accuracy was ±1% and sensitivity in temperature differences was as low as 0.001 K.

2.4 X-ray diffraction techniques

X-rays are electromagnetic radiation with wavelength of about 1 Å (10^{-10} m). The discovery of X-rays in 1895 enabled scientists to find the crystalline structure of the crystals. X-ray diffraction is used in two main areas: the determination of the crystalline structure and the characterisation of structural parameters of crystalline materials. X-ray diffraction determine how the atoms pack together in the crystalline state, and what the interatomic distance and angle are. X-ray diffraction is one of the most important characterisation tools used in solid-state chemistry and materials science [106].

2.4.1 X-ray powder diffraction

Powder diffraction is an extremely powerful non-destructive tool for identifying crystalline phases and qualitatively and quantitatively analysing mixtures. It is used to analyse unit-cell parameters as a function of temperature and pressure and to determine phase diagrams.

Compilations of the known powder diffraction patterns are maintained by the Joint Committee for Powder Diffraction Standards (JCPDS).

W.L. Bragg provided the first mathematical explanation of the positions of the X-ray diffraction spots. This expression, which is known as Bragg's law (equation 2.1), gives the permitted angles of reflection, θ, in terms of the wavelength of the radiation used λ and the spacing of the reflecting planes, d_{hkl}.

$$n\lambda = 2d_{hkl}\, sin\theta \qquad [2.1]$$

n is an integer, analogous to the order of diffraction from a grating, so that $n\lambda$ is the path difference between waves scattered from adjacent lattice planes with equivalent indices.

With a powdered crystalline specimen, many orientations of tiny crystallites are present simultaneously. When the incident beam strikes a powder sample, diffraction occurs in every possible orientation of 2θ. For any set of crystal planes, Bragg's law will be satisfied in some of the crystallites, the complete diffraction patterns will be observed for any orientation of the specimen with respect to the X-ray beam.

A Siemens D-5000 powder diffractometer was used with Bragg-Brentano parafocusing geometry and a θ-θ configuration, using a Cu source (λ_{Ka1} = 1.540560 Å), available at the *Servei de Recursos Científics* of the Rovira i Virgili University. In this system, the source, the sample and the detector occupy three consecutive positions on a circumference. This configuration guarantees the same Bragg conditions for a large area of the sample. The positions of the source and the detector vary in a synchronous way, always maintaining a symmetrical position, while the sample is always fixed.

In the thermal characterisation, we incorporated an Anton-Paar HTK10 platinum ribbon heating stage. This was connected to a thermocouple and a controller to allow different velocities for heating and cooling the sample [107].

2.4.2 X-ray single-crystal diffraction

X-ray single-crystal diffraction is the main method for determining the space group and lattice parameters, their crystalline structure and the positions of the atoms in the lattice of individual crystals.

Data collection (the result of systematically rotating the single crystal with respect to the X-ray beam) produces a complete set of data comprising a list of peak positions (*hkl* indices of the reflections) and the corresponding intensities. A first electron-density map is calculated from these results. Mathematical refinement techniques are used to improve the approximate atom coordinates obtained from the imperfectly phased Fourier synthesis. Refinement obtains final coordinates and, for each atomic position, a displacement or thermal parameter.

A Enraf-Nonius CAD-4 diffractometer with a Mo $K\alpha$ monochromatic radiation was used, available at the *Servei de Recursos Científico-Tècnics* of the University of Barcelona.

2.5 Sample preparation

To prepare the samples for optical measurements, the surface of the samples were cut and polished to make them free of scratches. First, the samples were cut with the correct orientation, depending on the experiment, using a goniometer and a Struers Accutom-50 diamond saw with disks of 0.12 and 0.25 mm thick. To eliminate the scratches, the samples were polished in a Logytech PM5 polisher with an oscillatory arm. This enables accurately rotate and pressurise the samples, depending on the hardness of the material to be polished. As abrasive substances, either alumina powders (hardness = 7 mohs) of 9, 3, 1 and 0.3 μm or diamond powder were used, depending on the quality of polish required. The quality of the polish was measured using parameters such as roughness, flatness (measured by a self-collimator) and parallelism between opposite faces of the sample (measured by the same self-collimator using the two reflections on the opposite faces of the sample). These systems are available at the FiCMA.

2.6 Principal optical axes orientation

The low temperature phase of $KRE(WO_4)_2$ belongs to the 2/m crystallographic point group. It is therefore a biaxial crystal with inversion centre. The three orthogonal principal optical axes are labelled N_g, N_m and N_p. These correspond to the directions with maximum, medium and minimum values of refractive index (n_g, n_m and n_p), respectively. In monoclinic crystals [108], one of the principal axes (in this case N_p) is always parallel to the C_2 symmetry axis that coincides with the crystallographic ***b*** axis. The other two principal axes (in this case, N_g and N_m) therefore lie in the ***a-c*** plane because the ***b*** axis is orthogonal to this plane. The orientation of the optical

indicatrix of $KRE(WO_4)_2$ was located by determining the angle between the ***c*** axis and the N_g (or N_m) principal axis in the ***a-c*** plane. This is of great interest as a first step in the optical characterisation of the samples. To do this, we used a polished sample along the *a-c* plane, which contains the principal directions with the n_g and n_m refractive indices. Note that the n_p refractive index extends along the N_p principal optical direction and is perpendicular to a natural face.

The experimental set-up consisted of two crossed polarisers that ensure the minimum transmission of light mounted on an oscillatory arm. In general, when we put an optically active crystal between the polarisers, light is transmitted unless the axis of the polarisers is parallel to one principal optical direction of the crystal. With this method, it is possible accurately determine the angle between any principal optical direction and the crystallographic axes.

Figure 2.3 illustrates the set-up used to determine the orientation of the principal optical axes.

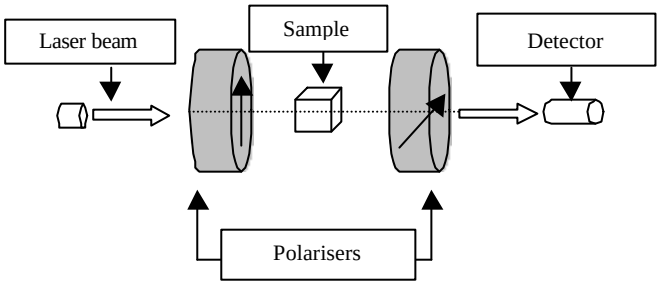

Figure 2.3 Set-up used to determine the orientation of the principal optical axes

2.7 Refractive indexes determination

The minimum deviation angle method with a slight modification was used to measure the refractive indexes of the samples [109]. Semi-prisms and the partial reflection that appeared in the second face of the prism were used. The first face of the prism was illuminated with an un-polarised laser beam. The prism was then rotated until a perpendicular incidence on the second face was achieved (in our case, a principal plane, m-g and p-g for the first and second prisms, respectively). In this way, the path of the laser beam had a symmetrical configuration and the deviation of the beam throughout the prism was minimal (see Figure 2.4). A precise goniometric table enables accurately determine the angle of the prism and the minimum deviation angle to a precision of 2 sec·arc.

The anisotropic behaviour of the crystals allows two beams with orthogonal polarisations to propagate in the crystal and the refractive indices in these orthogonal directions to be obtained. If we cut the prism in such a way that the second face of the prism is a principal plane, the measured refractive indices correspond to two principal optical axis values. Two prisms were used, one with a face parallel to the N_mN_g plane and the other with a face parallel to the N_gN_p plane. Thus, with the first prism n_m and n_g refractive indexes were measured and with the second prism n_g and n_p refractive indexes were measured. Note that as n_g is measured twice, an error in the measurements was estimated. The refractive indexes were measured at different wavelengths using the same OPO-laser system as the used for luminescence experiments and the data were fitted using Sellmeier equation.

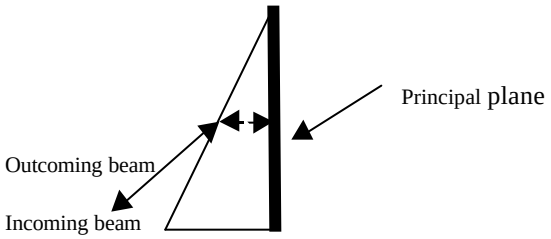

Figure 2.4 Schematic view of the beam paths inside the prisms

2.8 Spectroscopic techniques

2.8.1 Absorption and transmission measurements

Absorption spectroscopy relates the amount and type of radiant energy absorbed by a material due to its structure, identity and concentration when an incident radiation passes through the matter. According to quantum mechanics, atoms and molecules can occupy a limited number of states that correspond to distinct energy levels. To be absorbed, the energy of the incoming radiation must exactly match the difference between two of the substance's energy levels.

Also, since absorption is proportional to the concentration, spectroscopy can also be used to quantify the amount of material in the sample.

Experimental measurements are usually made in terms of transmittance (*T*), which is defined as the light intensity after it passes through the sample over the initial light intensity. Modern

spectrophotometers can usually display the data as either transmittance, or absorbance (usually called optical density). Absorbance is the negative logarithm of transmittance.

Moreover, the absorption coefficient α is the variation in the intensity of the electromagnetic radiation through a medium and is represented by the following expression:

$$I = I_0 e^{-\alpha d} \qquad [2.2]$$

where *d* is the thickness of the sample. The correlation between α and the absorbance (or Optical Density (*OD*)) can be deduced.

$$a = A\left(\frac{1}{d \log e}\right) \qquad [2.3]$$

Since α depends on the concentration of the absorbent centres, a more convenient parameter to describe the absorption process is the absorption cross-section, which is defined as the absorption coefficient over the density of absorbent centres. α is given in cm^{-1} and the concentration in atoms·cm^{-3}. Therefore, σ is in atoms·cm^2 or simply cm^2.

Absorption studies were carried out in a Varian Cary 500 Scan spectrophotometer, available at the FiCMA. This is a double-beam spectrophotometer with an effective spectral range from 0.25 to 3.00 μm with which optical densities from 0 to 10 can be measured.

Spectrophotometers consist of a stable source of radiant energy, a sample container, a device for isolating specific wavelength (monochromator), a radiation detector that converts transmitted radiation to a usable signal, and a signal processor and readout. These components are discussed below.

A radiation source for spectroscopy must generate a beam with sufficient power, wavelength range and stability to provide detectable and reproducible results. Our spectrophotometer uses a deuterium lamp for the UV range and switches to a quartz halogen source at 350 nm for the visible-IR range.

The solid sample holders are secured to the optical rails that enable the sample to be positioned anywhere in the beam, thus catering for a range of sample thicknesses. We have 1-5 mm aperture

masks supplied with the holders to allow beam collimation and measurement in small samples. Two holders can be mounted in series across both the sample and reference beams.

The monochromator has an entrance slit, a collimating lens, a dispersion diffraction grating, a focusing lens and an exit slit. Polychromatic radiation enters the monochromator through the entrance slit. The beam is collimated, then strikes the dispersing element at an angle. The beam is split into its component wavelengths by the grating. Our spectrophotometer turns the gratings around 800 nm. When the dispersing element or the exit slit moves, radiation of only one particular wavelength leaves the monochromator through the exit slit. Our spectrophotometer has two gratings with 1200 lines/mm in the UV-visible region and 300 lines/mm in the IR region.

Two kinds of detectors were used, depending on the wavelength: a photomultiplier tube (Hamamatsu R928), which is very sensitive to UV and visible radiation and an electrothermally controlled lead sulfide photocell. The first one is used up to 850 nm and the second one was used in the IR range. The IR detector was kept at 273 K by peltier cooling. This increased stability in the NIR and reduced photometric noise.

Because of the high physical anisotropy of our tungstates, we used a polariser to analyse the optical absorption with the electric field of the incident radiation parallel to each principal optical direction. The unpolarised light emitted by the lamps of the spectrophotometer is partially polarised by the instrument optics when it reaches the sample. The polarising characteristics of a spectrophotometer are affected by alignment, age and selected spectral band. The polarised optical absorption spectra were obtained with an accurately oriented Glan-Taylor polarising prism mounted in a stainless steel slide located behind the sample. Unpolarised absorption spectra were obtained using the direct light emitted by the lamps.

To study the optical absorption at low temperatures (6 K), we used a Leybold closed cycle helium RDK 6-320 cryostat, which has a controlled heater that can stabilise the temperature in the 6-100 K range to a precision of ± 3 K and in the 200-300 K range to a precision of ± 5 K.

A Varian Cary 500 Scan spectrophotometer was used to measure the transparency in the UV-visible and NIR region (300-3000 nm). A FTIR Midac Prospect spectrophotometer was used in the 3.0-10.0 μm region and a FTIR-680Plus in the 3.0-16.0 μm region. The two later spectrophotometers are available at the *Servei de Recursos Científics* of the Rovira i Virgili University.

2.8.2 Luminescence (emission and lifetime measurements)

Atoms that are excited to high energy levels after absorption can decay to lower levels by emitting energy. For atoms excited by a high-temperature energy source, this light emission is commonly called atomic or optical emission, and for atoms excited with light, it is called atomic fluorescence. Transition from a higher level to a lower level is called photoluminescence if energy is transferred to the radiation field. It is called non-radiative decay if no radiation is emitted.

The photoluminescence spectrum provides the transition energies, which can be used to determine electronic energy levels. The photoluminescence intensity provides a measure of the relative rates of radiative and non-radiative recombination. Photoluminescence was used to determine the electronic transition between the energy levels and to determine their lifetime.

Under pulsed excitation, the transient photoluminescence intensity yields the lifetime of non-equilibrium states. The intensity of the emission after excitation of the electrons declines exponentially over time. The time between the start of the emission and when its intensity decreases to $1/e$ of its initial value is called the radiative lifetime ($\boldsymbol{t}$). This important parameter characterises how an electronic level is depopulated and the dynamic mechanism of this excitation. This light can be collected and analysed to provide a wealth of information about the photo-excited material.

Our photoluminescence set-up consisted of the light source, holder, wavelength selector (monochromator), detectors and electronic facilities for processing the signal. Optical excitation was provided by a narrow linewidth BMI Vega pumped by the third harmonic of a seeded BMI SAGA YAG:Nd^{3+} laser. With this system, pulses of 7 ns and a repetition rate of 10Hz were achieved in the spectral range of 400-1700 nm. The intensity of the beam was controlled by two Glan-Taylor polarisers. Typical energies of 2mJ per pulse were used in these experiments. An electronically chopped diode laser with an output power of 750 mW at 940 and 800 nm was also used.

The excitation was driven to the sample by a prism and focused on it by a lens. The fluorescence, recorded at 90º to minimise the influence of the laser pump, was analysed spectrally with a Jobin Yvon-Spex HR460 monochromator. This had a focal length of 460 mm and a spectral resolution of 0.05 nm. For UV-Vis radiation the projecting fluorescence was detected by a Hamamatsu R928

photomultiplier, and for NIR radiation it was detected by a cooled Hammamatsu R5509-72 NIR photomultiplier. The signals were processed by a lock-in EG&G 7265DSP amplifier and the signals for lifetime measurements were treated with a computer-controlled Tektronik TDS-714 digital oscilloscope. Cryogenic temperatures for luminescence were obtained by an Oxford closed-cycle helium CCC1104 cryostat. All this equipment is available at the *FiCMA*.
Figure 2.5 illustrates the luminescence set-up.

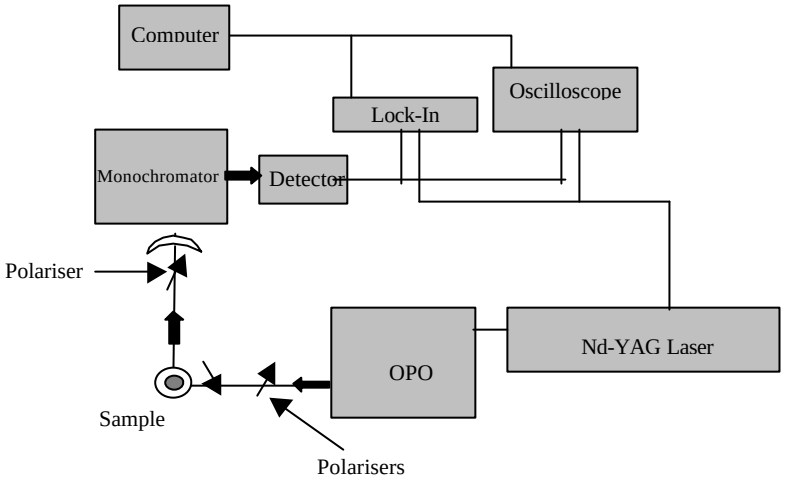

Figure 2.5 Scheme of the set-up used for luminescence experiments

2.9 Laser set-up

The laser experiments with $KYb(WO_4)_2$ and Yb^{3+} -doped $KLu(WO_4)_2$ single crystals were performed in two different resonators. For the $KYb(WO_4)_2$ experiments, a 57 cm long V-type, astigmatically compensated resonator was used. The sample, under Brewster angle, was positioned in the focal region between the folding mirror and rear mirror, which were both highly reflective in the emission spectral range and had a radius of curvature of 10 cm (Fig. 2.6). The output coupler at the other end of the cavity was a plane mirror with a transmission of 1%. The thin plane of $KYb(WO_4)_2$ was cut and oriented for propagation along the $\boldsymbol{b}(N_p)$ axis and polarisation along the N_m crystallo-optic axis. The choice of polarisation is very important for optimising the net amplification.

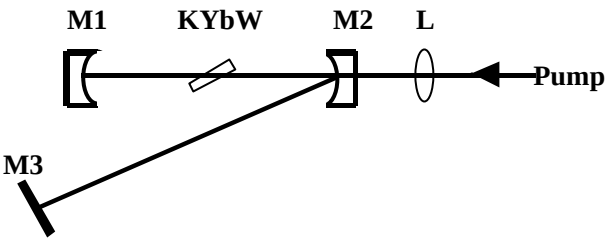

Figure 2.6 Laser set-up for the pulsed laser experiments on KYbW samples

For Yb^{3+} -doped $KLu(WO_4)_2$ crystals, the samples were also inserted under Brewster angle between the folding mirrors (radius curvature = -10 cm) of a standard astigmatically compensated *Z*-shaped resonator (Fig. 2.7). The pump radiation was focused by an AR-coated lens through one of the folding mirrors, which was highly transmitting near 980 nm. The second folding mirror was highly reflective at both the laser (l_L) and the pump (l_P) wavelengths. The latter permitted to pump the active medium from the back side in a second pass by 80% retroreflection at the total plane reflector terminating this arm of the pump radiation nonabsorbed in the first pass. No special care was taken to cool the crystal. In the other arm of the cavity, a plane output coupler (OC) with transmission (T_{OC}) from 1.5 to 10% was used.

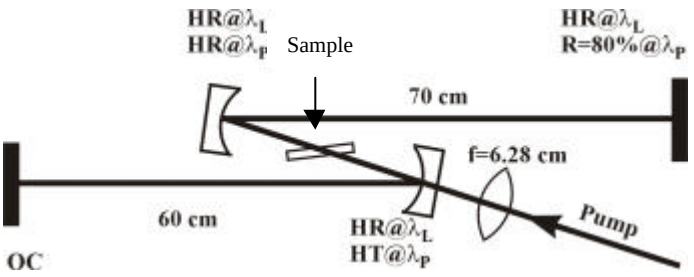

Figure 2.7 Laser set-up for the CW experiments on Yb^{3+} -doped KLuW samples

The pump sources were, on the first place, a home-made continuous wave Ti:sapphire laser optimised for operation at relatively long wavelengths. This laser was tunable between 900 and 1000 nm when pumped by 24 W (all lines) of an argon ion laser and had a maximum output

power of about 3 W between 920 and 970 nm. The pump beam was focused by a 6.3 cm lens through the folding mirror of the crystals laser cavity.

A tapered InGaAs diode laser was also used. This laser delivered up to 2 W of output power at 978 nm and was tunable between 975 and 981 nm by the temperature, with an M^2 factor for the slow axis emission of less than 3 ($1/e^2$-value). More details on this laser diode can be found elsewhere [110].

The uncoated sample plates were inclined at Brewster's angle to minimise Fresnel losses, but this did not essentially modify the polarisation or propagation directions inside the sample. No special care was taken for good thermal contact or for cooling the sample. To reduce the thermal load, a chopper with a duty cycle of 4% was used, which, for $KYb(WO_4)_2$, reduced the average powers 25 times.

All this equipment is available at the Max Born Institute for Nonlinear Optics and Ultrafast Spectroscopy (Berlin, Germany).

CHAPTER 3

MONOCLINIC $KRE(WO_4)_2$ SINGLE CRYSTALS

This Chapter focuses on the experimental results involving $KRE(WO_4)_2$ crystals, where RE denotes Gd^{3+}, Y^{3+}, Yb^{3+}, Er^{3+} and Lu^{3+}. We will refer to the papers enclosed at the end of this thesis to explain the results included in this Chapter. All these results were obtained at the Rovira i Virgili University (Spain).

Table of contents

We will refer to the following papers to explain the results included in this Chapter.

Paper I: Pujol, M.C.; **Mateos, X**.; Solé, R.; Gavaldà, Jna.; Massons, J.; Aguiló, M.; Díaz, F. "Linear Thermal Expansion Tensor in $KRE(WO_4)_2$ (RE=Gd,Y,Er,Yb) Monoclinic Crystals." *Materials Science Forum*, **378-381**, 710-717 (2001).

Paper II: Pujol, M.C.; **Mateos, X**; Solé, R.; Massons, J.; Gavaldà, Jna.; Solans, X.; Díaz, F.; Aguiló, M. "Structural, Crystal Growth and physical anisotropy. $KYb(WO_4)_2$. A new laser material." *Journal of Applied Crystallography*, **35**, 108-112 (2002).

Paper III: Pujol, M.C.; Bursukova, M; Güell, F.; **Mateos, X**.; Solé, R.; Gavaldà, Jna.; Aguiló, M; Massons,J.; Díaz, F.; Klopp, P.; Grieber, U. and Petrov, V. "Growth, optical characterization and laser operation of a stoichiometric crystal $KYb(WO_4)_2$." *Physical Review B*, **65**, 165121:1-11 (2002).

Paper IV: **X. Mateos**, R. Solé, Jna. Gavaldà, M. Aguiló, J. Massons, F. Díaz," Crystal growth, optical and spectroscopic characterisation of monoclinic $KY(WO_4)_2$ co-doped with Er^{3+} and Yb^{3+}. " *Optical Materials* (2004), in press.

3.1 Crystallisation of the monoclinic $KRE(WO_4)_2$

The group of double tungstates $KRE(WO_4)_2$ (RE = Y, Sm-Lu) (hereafter KREW) has a tetragonal structure when crystallising from a melt [111]. The monoclinic phase (called the low-temperature phase) appears below its melting point [112, 113]. KREW present polymorphism. This phase transition determines that crystallisation from high-temperature solutions is the most suitable method for growing KREW un-doped single crystals and KREW doped with lanthanide ions. The choice of solvent and the crystal growth conditions from the corresponding solutions are of definite interest. The phase transitions of the KREW were studied in [36, 114, 115, 116] and will not be treated in this study. Fig. 3.1 shows the DTA curve of KLuW. In this figure one can see that the phase transition appears at 1312 K and the melting point is 1326 K.

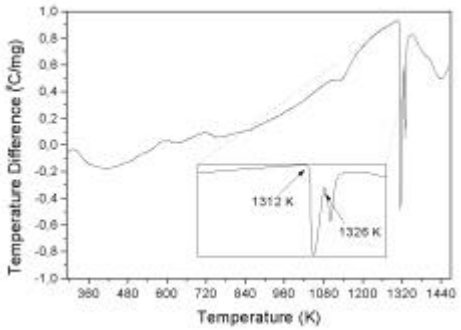

Figure 3.1 DTA curve of KLuW

The literature [117, 118, 119, 120, 121] reports the use of two high-temperature solvents of the K_2O-WO_3 system to grow KREW. These are K_2WO_4 and $K_2W_2O_7$. Both solvents contain only elements that participate in the composition of the crystals to be obtained, so foreign components will not be included. However, K_2WO_4 seems to have problems due to the long time needed to homogenise the solutions (higher viscosity than $K_2W_2O_7$ and melting temperature of 1194 K) and the relatively poor dopant distribution coefficient (see for example Nd^{3+} in [122]). On the other hand, $K_2W_2O_7$ has a melting temperature of 892 K [123] and a greater tungsten content, which minimises the viscosity of the solution. This enables the crystal to grow at relatively low temperatures, which decreases the saturation temperature and lowers viscosity. Also, because of the broad concentration and temperature ranges of crystallisation of the low-temperature phase, $K_2W_2O_7$ is

a promising high-temperature solvent for growing un-doped and doped KREW crystals. KREW has good solubility in $K_2W_2O_7$ at temperatures of the order of 1260 K, the solutions are easily homogenised, volatility is low and the tendency to creep is negligible. Finally, $K_2W_2O_7$ allows distribution coefficients of the doping agents of around 1 (depending on the dopant ion). The solubility of KREW in $K_2W_2O_7$ depends on the basic-acid behaviour of these compounds. For all the reasons mentioned above, $K_2W_2O_7$ solvent was chosen to grow the KREW crystals.

To determine the solubility curves, several solutions were prepared. Each solution was homogenised for 1 to 2 hours at about 100 K above their approached saturation temperature, T_s. A clear, transparent solution was obtained. Fast cooling was then carried out to about 20 K above T_s, followed by a slow cooling process. The crystals were obtained on a platinum wire previously immersed in the solution. It was not necessary to stir the solution. However, we will see later that it is necessary for growing larger crystals. The solution temperature was then gradually increased or decreased the solution temperature in 5 K steps every 30 minutes to more accurately determine the saturation temperature. The phase was identified by visual observation of the crystal morphology using a conventional Olympus lens (x40) and by X-ray powder diffraction analysis using the experimental equipment described in Chapter 2.

The solubility curves for KGW and KYW in $K_2W_2O_7$ and in K_2WO_4 are shown in Fig. 3.2. The solubility curves of KYbW, KErW and others in $K_2W_2O_7$ are shown in Fig. 2 of Paper I. The solubility curves of KGW and KYbW in $K_2W_2O_7$ are compared in Fig. 1 of Paper II.

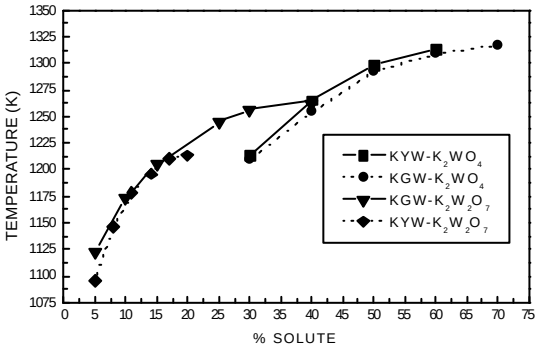

Figure 3.2 Solubility curves of KGW and KYW in K_2WO_4 and $K_2W_2O_7$ solvents

Fig. 3.2 shows that saturation temperatures are lower when the $K_2W_2O_7$ solvent is used than when the K_2WO_4 solvent is used. Using $K_2W_2O_7$ and for values up to 20 mol%, the saturation temperature increases significantly as a function of the solute concentration and increases slightly in the 20-42 % range in the case of KGW. To avoid generating inclusions and large changes in the saturation temperature due to fluctuations in temperature, the growth experiments must be performed only with solutions with a solute concentration of less than 20 mol% [124]. In the case of KYW, the solute concentration must be lower than 15 mol%. This range of solutions also performs well in terms of volatility and creeping in Pt crucibles.

If we compare the curves, including those of KGW, KYW, KYbW KErW and KLuW, one can see that the curves are nearly parallel to each other for the same solvent. There is a slight change in the saturation temperature when the rare-earth constitutional element is changed. The suitable composition range for the crystal growth of KREW is 10-15 mol% solute/90-85 mol% solvent with $K_2W_2O_7$.

The chemicals were K_2CO_3, WO_3 and the rare-earths were added as oxides. Taking into account that the K_2CO_3 decomposed to give K_2O and $CO_2\uparrow$, the reactions were:

$$K_2O + 2\ WO_3 \longrightarrow K_2W_2O_7 \quad \text{(solvent)}$$

$$K_2O + RE_2O_3 + 4\ WO_3 \longrightarrow 2\ KRE(WO_4)_2 \quad \text{(solute)}$$

In this study, the crystals were grown with a molar solute/solvent relation from 11.5/88.5% to 15/85%, respectively. The molar composition of the growth system for a solute/solvent relation of 15/85% is summarised in Table 3.1.

Table 3.1 Molar composition of the growth system (solute/solvent = 15/85%)

	K_2O (mol%)	**RE_2O_3 (mol%)**	**WO_3 (mol%)**
Solvent	33.33	----	66.67
Solute	16.67	16.67	66.67
Solution	30.83	2.5	66.67

3.2 The structure of the monoclinic $KRE(WO_4)_2$

The first information about the KREW structure appeared in 1969 when Kletsov et al. [36] solved the structure of KGW using powder diffraction and optical goniometric measurements and, reported that this crystal belongs to the monoclinic system with parameters a = 8.07 Å, b = 10.64 Å, c = 7.67 Å and β close to 94°, but did not give the space group. Later, in 2001 it was solved the structure of KGW [125] with cell parameters listed in Table 3.2 and space group C2/c, closing a period of certain confusion originated by a double form of giving the parameters that implied a change with the space group. The lattice parameters of the unit cell of KREW are summarised in Table 3.2. The data for KYW and KErW, from Paper I, are from powder diffraction and the data for KYbW, from Paper II, are from single crystal diffraction.

Table 3.2 Lattice parameters of the KREW unit cells with C2/c in Å

	a	***b***	***c***	**b (º)**	**Ref.**
$KGd(WO_4)_2$	10.652(4)	10.374(6)	7.582(2)	130.80(2)	125
$KY(WO_4)_2$	10.6313(4)	10.3452(6)	7.5547(3)	130.752(2)	P. I
$KYb(WO_4)_2$	10.590(4)	10.290(6)	7.478(2)	130.70(2)	P. II
$KEr(WO_4)_2$	10.626(1)	10.325(1)	7.541(1)	130.762(6)	P. I
$KLu(WO_4)_2$	10.592(3)	10.236(6)	7.498(1)	130.75(2)	126

The coordination figure of the tungstate anion is a distorted octahedron, WO_6, with three shorter W-O distances. Two octahedra are joined by shared edges $O2\cdots O2^{i}$ (symmetry code i = (-x,-y,1-z)) and make up a unit of two distorted octahedra. These form a double chain in the ***c*** direction by sharing vertix O4 (see Fig 3.3).

The shared edge between octahedra is the shortest $O2\cdots O2^{i}$ bond in the structure and, likewise, the second shortest edge $O2\cdots O3^{i}$ is the one shared between tungstate and rare-earth polyhedra. In fact, the oxygen anions O^{2-}, which make up the W^{6+} environment, are polarised due to the highly positive charge of the tungstate anion. This decreases the crystal field strength on the rare-earth. Because of the weak crystal field, the splitting is smaller than that of other ionic matrices [127].

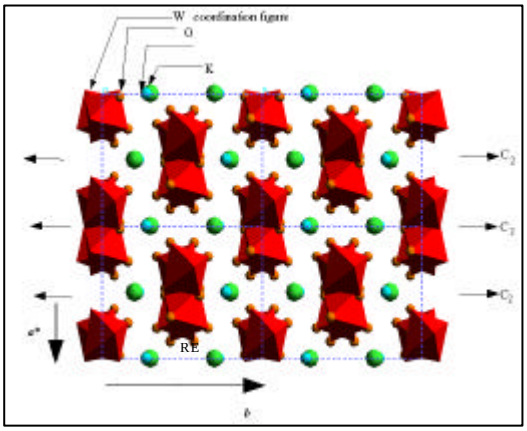

Fig. 3.3 Double chain formed by tungstate octahedra // [001]

The rare-earth polyhedron is eight-coordinated by oxygen atoms to form a square antiprism. These polyhedra form a single chain in the [101] direction by sharing edges $O3\cdots O3^{xvi}$, (symmetry code: xvi = ½-x, ½-y, 2-z), (see Fig. 3.4).

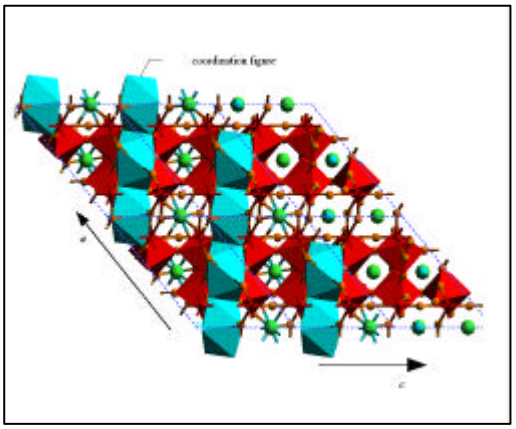

The alkali cation K^+ is twelve-coordinated by oxygens to form a distorted icosahedron. These polyhedra form a bidimensional layer formed by chains, which share edges in the [101] and [110] directions. These chains fill the holes in the framework of the rare-earth and tungstate polyhedra. All polyhedra that build the monoclinic KREW structure are strongly linked by sharing edges and corners. Crystal data and details of data collection and refinement are given in Table 1 of reference [125] for KGW and in Table 1 of Paper II for KYbW.

Atomic coordinates and interatomic distances are given in [125] for KGW and in Tables 2 and 3 of Paper II for KYbW. Data on the structure of KYW can be found in [128]. The structural resolution of KLuW is now under study.

KREW crystals show a very high physical anisotropy that is related to their remarkable crystallographic anisotropy. As this compound is an interesting laser host, it is interesting to analyse how the unit cell expands and to determine its linear thermal expansion coefficients to predict their thermal behaviour**.** In this study, the unit cell parameters of the un-doped KREW were measured as a function of temperature by X-ray powder diffraction analysis, using the equipment described in Chapter 2 for powder diffraction analysis. The cell parameters were refined with the FULLPROF program [129], using data of crystalline structure, space group, cell parameters and fractional atomic coordinates of KREW as structural model. The data for KGW, KYbW, KYW and KErW are given in Table 1 of Paper I.

Figure 3.5 shows the linear relationship between ($\Delta L/L$) of the unit cell parameters and temperature for the four hosts above. As can be seen all the crystallographic parameters increase when the temperature increases. At the moment KLuW is under study. Fig. 4 in Paper II also shows this linear relationship for KYbW. The linear thermal expansion coefficients of KREW are given in Table 2 of Paper I. The linear thermal expansion tensor at room temperature in the crystallophysical system $\mathbf{X_1//a,\ X_2//b,\ X_3//c^*}$ and in the principal system that diagonalised the linear thermal expansion tensor, $\mathbf{X'_1, X'_2//b, X'_3}$, are also given in Paper I.

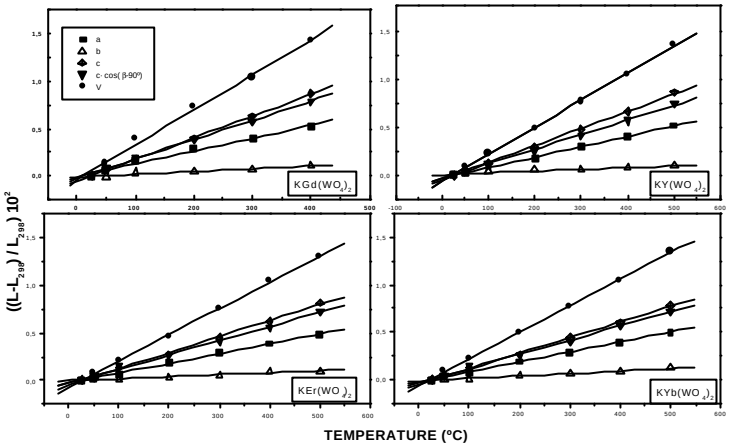

Fig. 3.5 Thermal evolution of the cell parameters and the unit cell volume for KREW

The principal axis with maximum thermal expansion, $\mathbf{X'_3}$, was found at δ by rotating anti-clockwise from the ***c*** axis with the ***b*** positive axis pointing towards the observer. The principal axis with the medium thermal expansion coefficient, $\mathbf{X'_1}$, was found at ρ by rotating clockwise from the ***a*** axis. These values are given in Table 3 of Paper I for the KREW hosts and reproduced in Fig. 3.6 with the thermal expansion ellipsoid of KREW.

Host	r (º)	d (º) =(b-90º)-r
KGW	28.77	12.00
KYW	32.18	8.57
KErW	30.51	10.25
KYbW	28.73	12.00

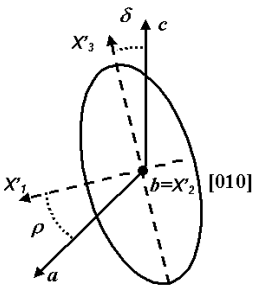

Fig.3.6 Value of the angles that locate the principal thermal axes in KREW. Thermal expansion ellipsoid of KREW in the principal system X'_1, X'_2//b, X'_3 and the crystallographic system

3.3 Crystal growth of the monoclinic $KRE(WO_4)_2$

The growth experiments were performed using the experimental set-up described in Chapter 2. Platinum cylindrical crucibles 50 mm in diameter and 60 mm high were used to prepare 200 g of solution using K_2CO_3 and WO_3 as predecessors for obtaining the KREW crystals with Gd_2O_3 for KGW, Yb_2O_3 for KYbW, Y_2O_3 for KYW, Er_2O_3 for KErW, and Lu_2O_3 for KLuW. The reagents were from Aldrich and Fluka (99.9% purity, except Yb_2O_3 for KYbW which was 99.99% pure). The composition of these solutions ranged from a solute/solvent molar ratio of 11.5/88.5% to 15/85%. Noted that previous data on the solubility curves (see section 3.1) were taken into account to select these solution compositions.

The mixtures were homogenised by maintaining the solutions at about 50 K above the saturation temperatures for 5-6 hours. Accurate saturation temperatures were then determined by observing the growth/dissolution of a seed in a contact with the free surface of the solution. The saturation temperatures for a composition of 11.5/88.5% solute/solvent were between 1178-1189 K for KGW, 1170-1175 K for KYbW, 1164-1170 K for KYW, 1183-1189 K for KErW and 1146-1162 K for KLuW. The growth processes began on a parallelepipedic-oriented seed of KGW to grow KGW single crystals, and one of KYW to grow KYW, KErW, KYbW and KLuW single crystals. For later crystal growth experiments, we used KYbW and KLuW seeds to grow KYbW and KLuW single crystals, respectively. The seed orientations were mainly along the ***b*** direction and provided crystals with good quality. However, in the first steps of the investigation, some ***c***-oriented and some ***a****-oriented (***a**** = reciprocal axis) directions were used. Unfortunately, for the two latter directions, the crystals sometimes showed inclusions and cracks. The typical seed dimensions were 10 x 2 x 2 mm^3.

Although different thermal conditions can be achieved simply by varying the position of the crucible inside the furnace, the axial thermal difference in the solution used was ususally 3-4 K and the bottom of the solution was hotter than the surface. The radial difference was about 2 K and the crucible wall was hotter than the centre of the solution. Supersaturation was achieved by

slow cooling from the saturation temperature of the solution at a rate of 0.1 K/h for KYbW and KLuW, 0.1 K/h for the first two degrees of the cooling interval, and 0.05 K/h for the second ten degrees of the cooling interval for KGW, KYW and KErW. For example, KGW showed a strong relationship between the cracks and the cooling rate. So, for example, if the cooling rate is 0.1 K/h, the crystals will grow with a large number of inclusions and cracks.

The crystal rotation (without pulling) was kept constant at 60 rpm for KGW and at 40 rpm for the other crystals. This ensured a volumic growth in the presence of a forced convective flow near the crystal. To minimise thermal shocks, the single crystals were removed slowly from the solution at a rate of 1mm/5min. and, after the crystals lost contact with the solution, we cooled to room temperature at a rate of 50ºC/h. An optical microscope (x40 magnification) was used to observe the macrodefects (inclusions and cracks) in the crystals but they were generally inclusion- and crack-free.

The weight of the crystals was independent of the host between 1.2 and 5.5 g. All of these un-doped crystals are colourless except KErW, whose colour is un-saturated red or pink due to the absorption of the hypersensitive transition of erbium near 530 nm ($^4I_{15/2} \rightarrow {}^2H_{11/2}$), with a green spectral colour.

Crystal dimensions were usually between 10 and 15.6 mm for the ***c*** crystallographic axis, between 5 and 8.50 mm for ***b*** and between 8 and 11.30 mm for ***a****.

The conditions and results of crystal growth experiments are found in [130] for KGW, in Papers II and III for KYbW and in Paper IV for KYW.

By way of example, Fig. 3.7 shows a photograph of KYW and KYbW single crystals. The single crystals were large enough to perform our optical studies.

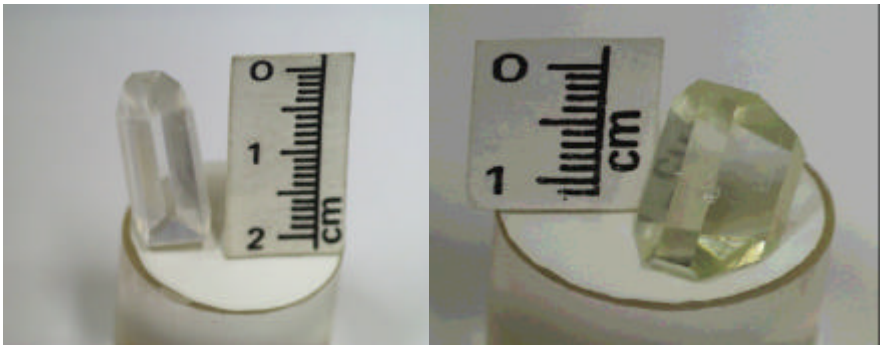

Fig. 3.7 Photographs of KYW (left) and KYbW (right) single crystals grown at FiCMA

3.4 Morphology of the monoclinic $KRE(WO_4)_2$

$KRE(WO_4)_2$ crystals have a crystalline habit that is formed by the {110}, {-111}, {010}, {130} and {310} faces. The first two faces are more developed than the lasts. In general the {010} face is more developed in KGW than with the other tungstates in this work. On the other hand, generally KLuW did not show this face. However, when changes to the growth conditions for the thermal environment of the crystal were applied, the {010} face developed without having at this moment explanation for this.

Pujol et al. [125] used the Hartman-Perdok theory to study the morphology of KGW. This theory states that crystal morphology is governed by the presence of periodic bond chains (PBCs).

In general, but not for all grown crystals, the dimension along the ***c*** crystallographic axis is approximately two times larger than the other two dimensions, except for KGW which appears a square. Also, the ***c*** axis and the [101] direction of the crystals grown appear as natural edges. The [101] direction from the *c* axis is located 85.59º for KGW [131] and 85.92º for KYbW, with the ***b*** positive axis directed towards the observer (see Papers II and III).

Fig. 3.8 shows the morphology of KYbW crystals with faces indexed (see Fig. 1 of Paper III). For KGW crystals, see Fig. 1 of Paper I.

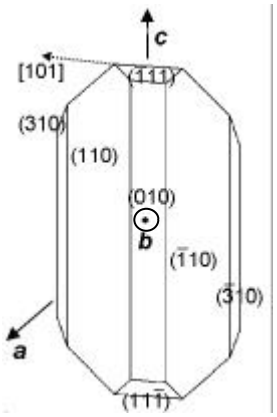

Fig.3.8 Morphology of un-doped KYbW single crystal

3.5 Optical characterisation

3.5.1 Transparency window

It is important to know the optical transparency of the hosts because, as it is mentioned in Chapter 1, crystals must be transparent at both pump and laser wavelengths. To determine the spectral range in which KREW are transparent, their optical transmission was measured in the 0.3 - 10.0 μm range, with samples of around 0.2 mm thick except for KYbW, which, because of Yb's high absorption band, was 0.1 mm. For the case of KLuW the sample was 1 mm thick. All of these measurements were taken without considering the anisotropy of the crystals.

The measured transmission of KYW is shown in Fig. 3.9. The UV cut-off wavelength was 315 nm (31.746 cm^{-1}) and the clear transparency for this thickness for the KREW was roughly between 320 and 5400 nm. The flat transparency region narrowed to approximately 500-4700 nm when samples over 0.2 mm thick were used. The cut-off wavelength of the UV band edge is related to a charge transfer $RE^{3+} \rightarrow O$ transition, while the cut-off wavelength in the infrared region is related to the $2\nu_1$ overtone [132] peak of the tungstate group fundamental vibration (ν_1 = 931 cm^{-1}). The transparency window of KYbW is shown in Fig. 2 of Paper III.

Fig.3.9 Transmission range of the KYW single crystals

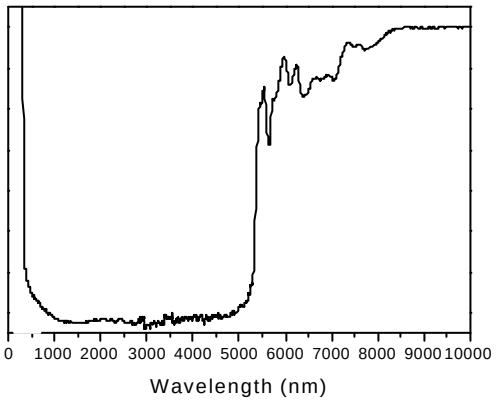

3.5.2 Optical indicatrix

The physical behaviour of many crystalline substances depends on the direction in which a certain external agent varies. In the case of optical properties, this implies a change in the refractive index depending on the direction of the vibration of the light inside the material.

As, for most crystals, the refractive index varies with the direction of the vibration of the light waves, it is helpful to visualise the values of the refractive index for all directions of vibration and relate them to the directions of propagation, which are perpendicular. The resulting geometric figure is called the optic indicatrix. Indicatrices represent the values of the refractive index for all the directions of vibration of a crystal.

If we represent the minerals in this way, we find three types of geometric shapes. For cubic materials, the optic indicatrix is a sphere. This is the case of isotropic materials. For uniaxial materials, it is an ellipsoid of revolution (with two principal axes) and for biaxial materials it is an ellipsoid with three principal axes.

The local symmetry of the monoclinic KREW is C2. The optical indicatrix is a triaxial ellipsoid with two circular sections and, therefore, two privileged wave normal directions for which there is no double refraction. These are the optical axes. The biaxial indicatrix is described by three refractive indices n_g, n_m and n_p, which define the lengths of the principal (semi-) axes of the indicatrix [133].

According to Neumann´s principle of crystal physics, one of the three orthogonal principal axes of the indicatrix must coincide with the C2 symmetry axis, which defines the ***b***-crystallographic axis of the KREW structure. This is the only axis of the indicatrix that is fixed in space for every wavelength of the electromagnetic spectrum. The direction of the other two orthogonal axes of the indicatrix generally depends on the wavelength of the light that propagates in the crystal. This well-known phenomenon in crystal physics is called *dispersion of the optical axes*, and it applies to all crystals of the monoclinic and triclinic system [134].

N_g, N_m and N_p was used to denote the direction of the highest, medium and smallest refractive indices, respectively. The orientation of the principal crystallo-optic axes was determined at λ= 632.8 nm using two crossed Glan-Taylor polarisers, as described in Chapter 2. The principal axis N_g, is located at κ with respect to the ***c*** crystallographic axis, where the angle of rotation κ is

measured in the clockwise direction when the positive end of the ***b*** axis is pointing towards the observer. The values for κ are shown in Fig. 3.10. This figure also shows the optical ellipsoid of KREW. The optical ellipsoid of KYbW and KYW can be found in Fig. 3 of Paper III and in Fig. 3 of Paper IV.

Host	k°
KGW	20
KYW	18.5
KEW	18.5
KYbW	19
KLuW	18.5

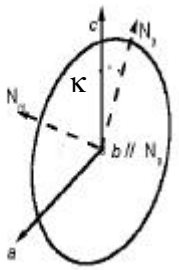

Fig.3.10 Optical ellipsoid corresponding to KREW single crystals

Therefore, the optical tensor can also be localised in the same way as the thermal tensor. The diagonalised optical tensor is shown in Paper II for KYbW.

3.5.3 Refractive index determination and dispersive chromatic curves

We determined the dispersion of the three refractive indices labelled $n_g > n_m > n_p$ and measured the thermo-optic coefficients. The dispersion of the principal values of the refractive indices was measured between 450 and 1500 nm by the minimum deviation method, as described in Chapter 2.

Figure 3.11 shows the dispersion of the refractive indices (dispersive chromatic curves) in the visible and near-infrared spectral regions of KYbW. As can be seen KREW possesses significant birefringence and the three refractive indices are almost equidistant. This figure is reproduced from Fig. 4 of Paper III.

We fitted the data points in Figure 3.11 using a Sellmeier equation. A brief description of the Sellmeier calculations is given in Paper III. Table 1 of Paper III summarises the Sellmeier coefficients obtained for KYbW at room temperature. How the refractive indices behave was studied with temperature in the 293-473 K range using a microfurnace with temperature control and taking care to homogenously heat the samples. The thermo-optic coefficients estimated at λ =

632.8 nm are also given in Table 1 of Paper III. Data on the values of the refractive indices as a function of wavelength can be found in reference [131] for KGW and in reference [135] for KGW, KYW and KErW.

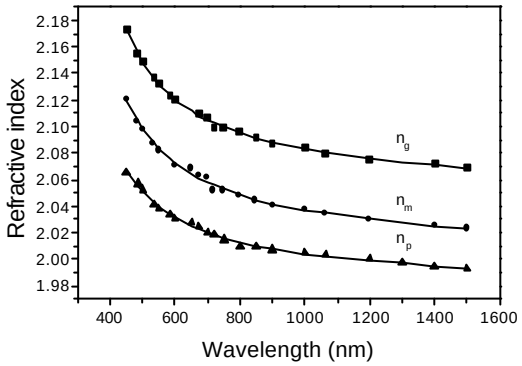

Wavelength	n_g	n_m	n_p
532	2,1413	2,0814	2,0433
630	2,112	2,058	2,016
1064	2,0815	2,0282	1,9939

Fig. 3.11 Dispersive chromatic curves of KYbW and some values (Table) of refractive indices of KLuW

CHAPTER 4

Ln^{3+} -DOPED MONOCLINIC $KRE(WO_4)_2$ SINGLE CRYSTALS

In this Chapter we summarise the experimental results on the effects of doping the crystals. These results focus on the changes in crystallisation, structure, crystal growth and morphology. The main part of this chapter is devoted to active ion spectroscopy, which forms the basis for the laser properties and concerns the optical absorption, optical emission and lifetime measurements of Yb^{3+} and Er^{3+} ions.

Table of contents

We will refer to the following papers to explain the results included in this Chapter.

Paper III: Pujol, M.C.; Bursukova, M; Güell, F.; **Mateos, X**.; Solé, R.; Gavaldà, Jna.; Aguiló, M; Massons,J.; Díaz, F.; Klopp, P.; Grieber, U. and Petrov, V. "Growth, optical characterization and laser operation of a stoichiometric crystal $KYb(WO_4)_2$." *Physical Review B,* **65**, 165121:1-11 (2002).

Paper IV: **X. Mateos**, R. Solé, Jna. Gavaldà, M. Aguiló, J. Massons, F. Díaz," Crystal growth, optical and spectroscopic characterisation of monoclinic $KY(WO_4)_2$ co-doped with Er^{3+} and Yb^{3+}. " *Optical Materials* (2004), in press.

Paper V: **X. Mateos**, C. Pujol, F. Güell, M. Galán, R. Solé, Jna. Gavaldà, M. Aguiló, J. Massons and F. Díaz. "Erbium spectroscopy and 1.5 μm emission in in $KGd(WO_4)_2$:Er,Yb single crystals." *IEEE Journal of Quantum Electronics*, **40**, 759-770 (2004).

Paper VI: **X. Mateos**, V. Petrov, M. Aguiló, R. Solé, Jna. Gavaldà, J. Massons, F. Díaz, U.Griebner, "Continuous Wave Laser Oscillation of Yb^{3+} in Monoclinic $KLu(WO_4)_2$." *IEEE Journal of Quantum Electronics*, **40**, 1056-1059 (2004).

Paper VII: **X. Mateos**, F. Güell, M.C. Pujol, M. A. Bursukova, R. Solé, Jna. Gavaldà, M. Aguiló, F. Díaz and J. Massons, "Green luminescence of Er^{3+} in stoichiometric $KYb(WO_4)_2$ single crystals." *Applied Physics Letters*, **80**, 4510 (2002).

Paper VIII: **X. Mateos**, M.C. Pujol, F. Güell, R. Solé, Jna. Gavaldà, J. Massons, M. Aguiló and F. Díaz. "Infrared-to-green up-conversion in Er^{3+},Yb^{3+} -doped monoclinic $KGd(WO_4)_2$ single crystals." *Optical Materials* (2004) in press.

Paper IX: **X. Mateos**, M. C. Pujol, F. Güell, R. Solé, Jna. Gavaldà, M. Aguiló, F. Díaz and J. Massons. "Sensitization of Er^{3+} emission at 1.5 μm by Yb^{3+} in $KYb(WO_4)_2$ single crystals" *Physical Review B*, **66**, 214104:1--12 (2002).

Paper X: **X. Mateos**, R. Solé, Jna. Gavaldà, M. Aguiló, J. Massons, F. Díaz, U. Griebner and V. Petrov, "Crystal growth, spectroscopic investigations and laser operation of Yb^{3+} -doped potassium lutetium tungstate.", *Optical Materials* (2004) submitted.

Paper XI: **Mateos, X**; Solé, R.; Gavaldà, Jna.; Aguiló, M; Massons,J.; Díaz. "Ultraviolet and visible emissions of Er^{3+} in $KY(WO_4)_2$ single crystals co-doped with Yb^{3+} ions." *Journal of Luminescence*, (2004) submitted.

Paper XII: **X. Mateos**, R. Solé, Jna. Gavaldà, M. Aguiló, J. Massons and F. Díaz. Ultraviolet and visible emissions of Er^{3+} in monoclinic $KYb(WO_4)_2$ single crystals." *IEEE Journal of Quantum Electronics*, (2004) submitted.

Paper XIII: P. Klopp, U. Griebner, and V. Petrov, **X. Mateos**, M. A. Bursukova, M. C. Pujol, R. Solé, Jna. Gavaldà, M. Aguiló, F. Güell, J. Massons, T. Kirilov, and F. Diaz. "Laser operation of a new stoichiometric crystal $KYb(WO_4)_2$", *Applied Physics B*, **74**, 185 (2002).

4.1 Crystallisation of monoclinic $KRE(WO_4)_2$ as a function of the dopant concentration

As our group has wide experience with the $K_2W_2O_7$ solvent, and as K_2WO_4 solvent, as it is described in Chapter 3, has problems related to the homogeneisation and distribution coefficient of the dopants, the crystallisation of the Ln^{3+} -doped KREW with K_2WO_4 solvent was performed. The solubility curves for several Nd^{3+} concentrations in KGW are shown in Fig 4.1 reproduced from [124]. As can be seen, these are almost parallel to each other. Note that in all cases the saturation temperature sharply increases as the solution concentration in the low concentration region, and after that, this increase begins to be more gradual.

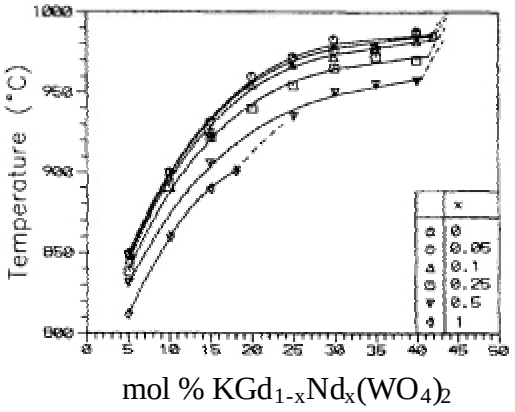

Figure 4.1 Solubility curves of the system $KG_{1-x}Nd_x(WO_4)_2$ -$K_2W_2O_7$ from reference [124]

It was found that increasing the dopant concentration led to an increase in solubility. At the same time, however, the concentration and temperature regions became narrower as the dopant concentration increased, especially when the substitution was above 50%.

The greater solubility of KGW in the $K_2W_2O_7$ solvent when the Gd^{3+} was partially substituted by Nd^{3+} may be due to the fact that the basic-acid behavior of these three compounds changes in the order $K_2W_2O_7$ > $KNd(WO_4)_2$ > $KGd(WO_4)_2$. $KNd(WO_4)_2$ is nearer to $K_2W_2O_7$ as a more basic compound than $KGd(WO_4)_2$. At the same time, the decrease in the stability regions of $KGd_{1-x}Nd_x(WO_4)_2$ as the Nd^{3+} concentration increased is probably related to the fact that the Nd^{3+} ion is larger than the Gd^{3+} ion, which makes the crystalline structure less stable. Moreover, $KNd(WO_4)_2$ has different struture to that of $KGd(WO_4)_2$.

The study to other lanthanides (Ln^{3+} = Er^{3+}, Eu^{3+} and Ho^{3+}) -doped KGW in $K_2W_2O_7$ solvent was extended in reference [136].

4.2 The structure of the Ln^{3+} –doped monoclinic $KRE(WO_4)_2$

It is interesting to know the structural changes that led to the substitution of the rare-earth for doping ions. The evolution of the crystallographic cell parameters was studied as a function of the Nd^{3+} content of the crystal in KGW. Figure 4.2 shows that the cell parameters and the unit-cell volume increased as the Nd^{3+} content of the crystal increased. This was expected because the ionic radius of Nd^{3+} is larger than the ionic radius of Gd^{3+}.

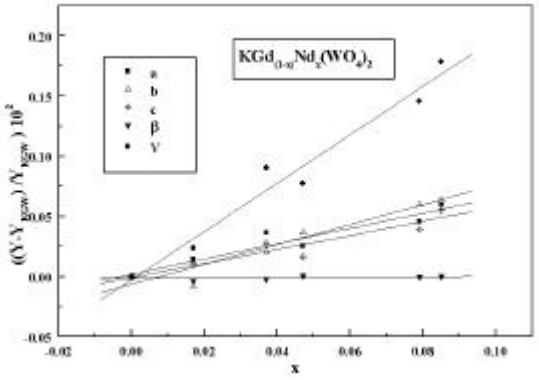

Figure 4.2 Evolution of the cell parameters as a function of the Nd^{3+} concentration from reference [130]

The work to other lanthanide ions was extended in reference [125] and concluded that the structure of the crystal expands when the lanthanide ionic radius is larger. The lattice parameters of the cases Er^{3+}- and Tm^{3+} -doped crystals increased without linear behaviour. Data for the cell parameters of the lanthanides in KGW are summarised in Table 3.14 of reference [137].

4.3 Crystal growth of the Ln^{3+} –doped monoclinic $KRE(WO_4)_2$. Measurement of the dopant concentration.

The suitable conditions for growing inclusion-free single crystals of Ln^{3+} (Ln^{3+} = Er^{3+} and Yb^{3+}) -doped KREW (Yb^{3+} -single doped, Er^{3+} -single doped and Yb^{3+}, Er^{3+} co-doped KREW) was

studied at several dopant concentrations. We substituted RE_2O_3 by Ln_2O_3 in the solution and Ln_2O_3 was added as oxides (Yb_2O_3 and Er_2O_3) to the mixture of reagents. The single crystals were grown by the TSSG method, initially using the same growth conditions as for un-doped KREW (see Section 3.3 of Chapter 3). In agreement with previous results [124, 136], it was found that, for all the lanthanide substitutions the saturation temperature tended to decrease slightly as the substitution level increased, except with Yb^{3+} substitution.

As for the un-doped KREW, the seed orientation was along the ***b*** crystallographic direction. Typically, the cooling rate was also 0.1 K/h for Ln -doped KYbW and KLuW, 0.1 K/h for the first two degrees of the cooling interval and 0.05 K/h for the second ten degrees of the cooling interval for Ln -doped KGW and KYW. KErW crystals were not doped. In some experiments, the second cooling interval was slightly changed as a function of the aspect of the crystal. When the growth rate was higher, the cooling interval decreased. The rotation rate of the seed during crystal growth was 40 rpm for Ln -doped KGW and 60 rpm for the other of Ln -doped tungstates.

Table I of Paper V provides information about crystal growth for KGW (dopant solution composition, cooling rate, cooling interval, crystal dimensions, etc). Table 1 of Paper IX provides this information for KYbW and Table 1 of Paper IV for KYW.

The substitution of the rare-earth in KREW for lanthanide ions was limited in the case of KGW by Yb^{3+} at 10%, when cracks began to appear. On the other hand, KYW accepted a substitution level of up to 100%, which allowed the crystal growth of the stoichiometric KYbW. This was also observed in the case of KLuW and is due to the difference between the ionic radii. For as accurate study of how crystal growth changes as the dopant concentration in KGW changes, see reference [137].

The composition of the single crystals was measured by EPMA (electron probe microanalysis), as described in Chapter 2, and the distribution coefficients of the various lanthanides in KREW were determined by

$$K_{Ln^{3+}} = \frac{(moles\ Ln^{3+}/(moles\ Ln^{3+} + moles\ RE^{3+}))_{crystal}}{(moles\ Ln^{3+}/(moles\ Ln^{3+} + moles\ RE^{3+}))_{solution}} \qquad [4.1]$$

A distribution coefficient of the dopant ions around unity meant that the stoichiometry of the solute in the crystal was conserved. The distribution coefficient was generally close to unity when

the crystals were doped with only one dopant. The distribution coefficients of co-doped samples, mainly Yb^{3+} as dopant, were less than unity, (see Table 1 of Paper IV). EPMA results are given in Table 1 of Paper VIII for KGW, in Table 1 of Paper IV for KYW and in Table 2 of Paper IX for KYbW. By way of example, Table 4.1 shows the EPMA results in the case of Yb^{3+} single-doped KLuW crystals.

Substituting the RE_2O_3 for Ln_2O_3 is easier when the ionic radius of Ln^{3+} is similar to that of RE^{3+}.

Table 4.1 Mol% of Yb^{3+} in the solution, distribution coefficients [K_{Lu} and K_{Yb}], dopant concentration [Yb^{3+}] and stoichiometric formula of Yb^{3+} single doped KLuW single crystals

% sol Yb	K_{Lu}	K_{Yb}	[Yb](cm^3)	Formula
0.5	0.99	1.66	$5.287x10^{19}$	$KLu_{0.9917}Yb_{0.0083}(WO_4)_2$
5	0.98	1.35	$4.300x10^{20}$	$KLu_{0.932}Yb_{0.068}(WO_4)_2$
10	0.96	1.29	$8.258x10^{20}$	$KLu_{0.8700}Yb_{0.1299}(WO_4)_2$

Figure 4.3 shows a KGW:Yb,Er crystal and its morphology. The crystals are large enough to perform our spectroscopic studies.

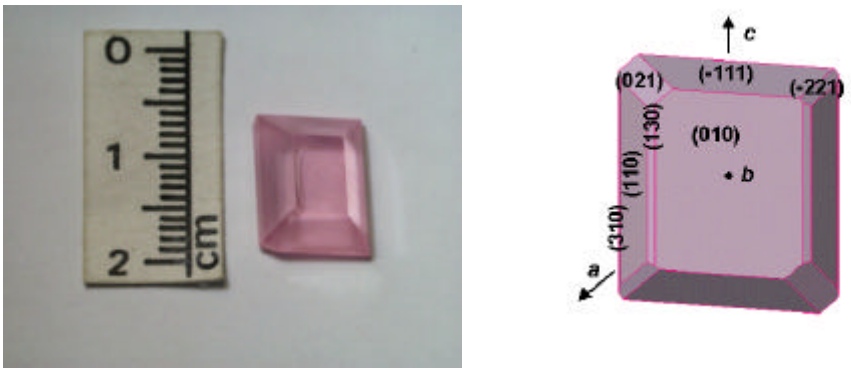

Figure 4.3 Photography of a KGW:Yb,Er single crystal

4.4 Morphology of the lanthanide –doped monoclinic $KRE(WO_4)_2$

Introducing lanthanides into the monoclinic KREW structure also affects the morphology. The habit of the un-doped monoclinic KREW crystals obtained in the experiments is basically made up of the {110}, {$\bar{1}$11}, {010}, {130} and {310} faces as described in Chapter 3.

New faces, {021} and {$\bar{2}$21} appeared in some cases when KREW were doped with lanthanides (Er^{3+} and Yb^{3+}).

Figure 4.4 shows the morphology of KYW doped with Yb^{3+}. The {-1-10}, {-1-11}, {0-10}, {-3-10}, {0-21} and {-2-21} faces appear.

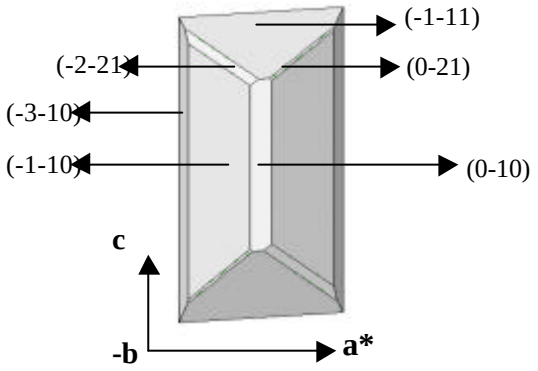

Figure 4.4 Morphology of KYW:Yb oriented with -b axis pointing towards the observer

4.5 Spectroscopic characterisation

4.5.1 Ytterbium spectroscopy

The most promising ion that can be used in a non-Nd^{3+} laser in the same range of emission wavelength is Yb^{3+}. The Yb^{3+} ion has several advantages as a laser-emitting centre over the Nd^{3+} ion because of its simple energy level scheme. This is made up of only two levels: the $^2F_{7/2}$ ground state and the $^2F_{5/2}$ excited state. There is no excited state absorption (ESA), cross relaxation or up-conversion, and there is no absorption in the green, which is very favourable for self-frequency doubling lasers (SFD). These processes, which are present for other rare-earth ions commonly used as lasing ions, can reduce laser efficiencies because alternate paths for energy transfer exist. The Yb^{3+} ion also has a low quantum defect, which, due to the energy mismatch

between the pump and laser wavelengths, leads to a low thermal load. The intense Yb^{3+} absorption lines are well suited for laser diode pumping near 981 nm and the small Stokes shift between absorption and emission reduces the thermal loading of the material during laser operation. The disadvantage of Yb^{3+} is that the final laser level is thermally populated (quasi-three-level laser), which increases the threshold.

4.5.1.1 Optical absorption

The study of the optical absorption allowed us to determine the character of the transitions between the energy levels and their energy position. The energy position of the Stark levels was determined by extending the study to low temperatures.

The absorption spectra were obtained for several polarisation configurations, N_g, N_m and N_p. These correspond to the case of the light beam parallel to the principal optical axes as described in Section 3.5.3 of Chapter 3.

We studied the polarised optical absorption of Yb^{3+} -doped KGW, KYW and KLuW and the stoichiometric KYbW. We used nanometers (nm) or wavenumbers (cm^{-1}) without distinction to denote the wavelength or the energy of the levels of the transitions. The conversion from one to the other is 1 nm = $(1/cm^{-1})*10^7$ and vice-versa. The spectra are shown in Fig. 5 of Paper V for KGW, Fig. 4 of Paper IV for KYW, Fig. 6 of Paper III for KYbW, Fig. 1 of Paper VI and Fig. 1 of Paper X for KLuW. Yb^{3+} has a clear absorption band between 11494 and 9500 cm^{-1} (870-1053 nm) for all these tungstates and there are slight differences between them. This band is associated with the ytterbium transition $^2F_{7/2} \rightarrow {}^2F_{5/2}$. Enough signal-to-noise ratio in the spectra was achieved by sewing curves measured with more than one sample. The Yb^{3+} concentration and thickness of the sample were lower around the maximum of absorption and the Yb^{3+} concentration and the thickness of the sample were higher in the wings of the spectra. The two parameters are reported in the above Papers. This is because of the high absorption cross-section in the maximum of absorption and the low absorption cross-section in the wings of the spectra, where a reasonable resolution is required to accurately calculate the emission cross-section shown later.

By way of example, Fig. 4.5 shows the polarised absorption spectra of Yb^{3+} -doped KYbW at room temperature with the schematic representation (inset) of the transitions corresponding to each peak.

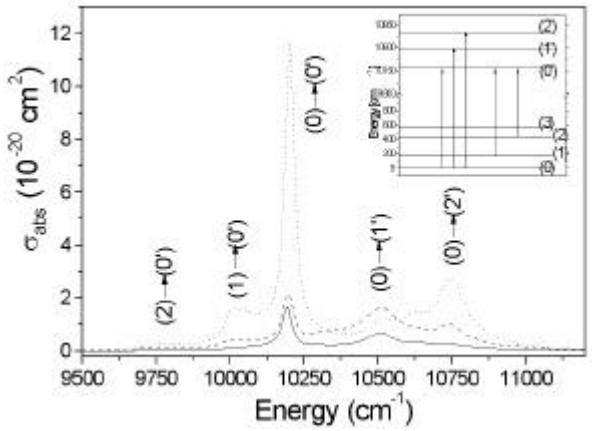

Figure 4.5 Polarised room temperature optical absorption of Yb^{3+} in KYbW. E//N_g (solid line), E//N_m (dotted line) and E//N_p (dashed line)

Note that optical absorption strongly depends on the light polarisation and is maximal for E//N_m and minimal for E//N_g. Room temperature absorption is characterised by three main peaks, which are labelled (0) → (0'), (0) → (1') and (0) → (2'), and two less intensive peaks, labelled as (1) → (0') and (2) → (0'). The three main peaks correspond to the transition from the lower sublevel of the ground state to the three sublevels of the excited state. The other two bands are related to the transitions from the second and third sublevels of the ground state to the lowest sublevel of the excited state (see inset).

The maximum absorption cross-section around 981 nm was of the order of 1.17×10^{-19} cm^2 for E//N_m with a linewidth of 3.6-4 nm. These values are higher than those reported for stoichiometric YbAG [138] but similar to those reported for KREW (RE= Y and Gd) with 5 at. % Yb^{3+} doping [139, 140].

The absorption length (1/e level) for KYbW calculated from the absorption at 981 nm (room temperature) was only 13.3 μm for polarisation parallel to the N_m principal axis due to the high quantity of Yb^{3+}. Such short absorption lengths are useful for the thin disk laser concept.

To accurately determine the Stark levels of Yb^{3+} in these crystals, the optical absorption spectra were measured at 6 K. Since Yb^{3+} has an odd number of electrons in the 4f shell, polarisation-dependent selection rules for the electronic transitions are not expected. This means that the number and positions of the absorption peaks must be independent of polarisation but the intensity of the peaks associated with the three polarisations may still change. As an example, Fig. 4.6 shows the low-temperature absorption of Yb^{3+} in KLuW ($E//N_m$) at 6 K. The spectra can be found in Fig. 7 of Paper V for KGW, Fig. 4 of Paper IV for KYW and Fig. 7 of Paper III for KYbW. Since at low temperature the most populated Stark level is the lowest of the ground state $^2F_{7/2}$ (0), the bands at 6 K can be associated with transitions from this sublevel to the three Stark levels of the excited state $^2F_{5/2}$.

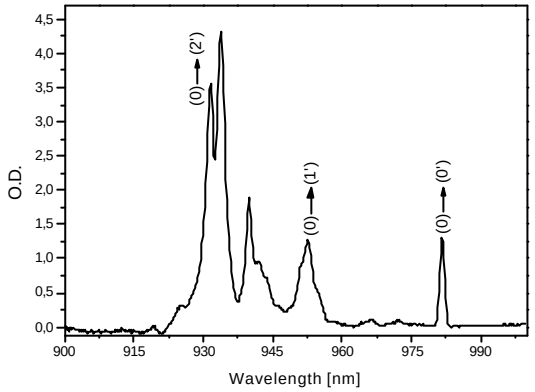

Figure 4.6 Low temperature absorption of Yb^{3+} in KLuW ($E//N_m$)

The values of the excited Stark level ($^2F_{5/2}$) of Yb^{3+} in KREW were determined at low temperature. These are summarised in Table 4.2.

Table 4.2 Stark levels of $^2F_{5/2}$ of Yb^{3+}determined at 6K

Host	Energy position (cm^{-1})
KGW	10196, 10487, 10686
KYW	10187, 10490, 10728
KYbW	10188, 10500, 10734
KLuW	10187, 10498, 10735

The value of the energy position of the Stark levels of the ground state, determined by emission experiments at low temperature, will be presented in the Optical Emission section.

Inspection of the low temperature absorption reveals a certain substructure. This substructure may be related to strongly phonon-electron-coupled transitions. This effect is more pronounced for RE^{3+} ions at the beginning and the end of the lanthanide series. The role of the Van-Vleck (one-phonon) process in the formation of the phonon sidebands for RE^{3+} ions has already been reported [141]. For this reason, it was studied between room temperature and 6 K only for the case of KYbW (see Fig. 4.7 from Fig. 7 of Paper III).

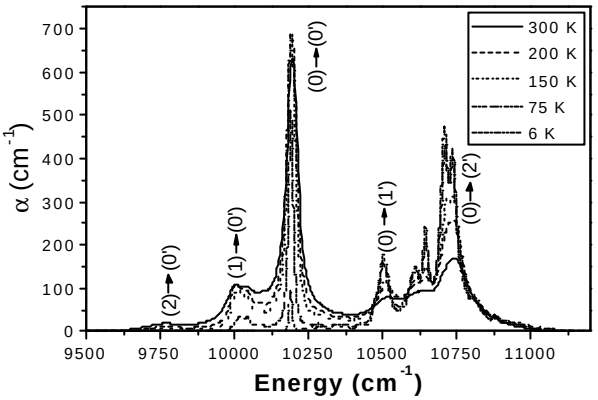

Figure 4.7 Evolution of the optical absorption with temperature in KYbW

The maximum absorption of the (0) → (0') transition around 981 nm (10193 cm^{-1}) decreases dramatrically when the temperature falls, though this effect is masked at higher temperatures by population redistribution among the sublevels of the ground state. On the other hand, the most pronounced vibronic features in the 6 K spectrum, which are between 10600 and 10650 cm^{-1} and near 10710 cm^{-1}, increase in amplitude at lower temperature. This behaviour can be attributed to resonant interactions involving the (0) → (0') transition and some Raman modes (ν_4^-, ν_4^0, ν_4^+ from Table 2 of Paper III). Note that additional resonances of other Raman modes also from Table 2 (E_g and E_u) with the (0) → (1') line may also contribute to this effect. Another explanation for the substructure observed near 10710 cm^{-1}, however, could be, the resonance of the Stark sublevel separation of 234 cm^{-1} between $^2F_{5/2}$ (1') and $^2F_{5/2}$ (2') with the 239 cm^{-1} B_g

phonon from Table 2 of Paper III, leading to resonant splitting of the $^2F_{5/2}$ (2') sublevel due to electron-phonon interaction [142].

The behaviour of the absorption line at 10019 cm^{-1} when the temperature reached 300 K was unusual: up to 150 K, the intensity of this line increased linearly with temperature but this dependence saturated at higher temperatures. This is unlike with the normal thermal behaviour of the absorption process. The saturation effect was attributed at 300 K to resonant interaction between ytterbium ions in the $^2F_{7/2}$ (1) sublevel (168 cm^{-1} energy) and the A_u vibration mode associated with $[WO_4]^{2-}$, as reported in Table 2 of Paper III.

The greater intensity of the zero line around 10190 cm^{-1} in the 150-200 K temperature range may be limited by the dynamic range of the spectrophotometer even for a sample thickness as low as 50 μm, as we used.

The Reciprocity method was used to calculate the emission cross-section from the absorption cross-section for all three polarisations of the $^2F_{5/2} \rightarrow {}^2F_{7/2}$ transition at room temperature (see for example Fig. 1 of Paper X). There is a brief explanation of the Reciprocity method calculations in Paper IX and a fuller explanation in references [138,143].

4.5.1.2 Optical emission

We studied the emission spectra to determine the emission channels and the Stark energy levels of the ground state of Yb^{3+} in KREW. Figure 4.8 shows, for example, the emission spectra of Yb^{3+} in KLuW at room and low temperatures by exciting at 940 nm. These consist of four main bands labelled in the spectra as (0') → (0), (0') → (1), (0') → (2) and (0') → (3), which can be associated with the transitions from the lowest sublevel of the excited $^2F_{5/2}$ state to each of the four levels of the $^2F_{7/2}$ fundamental state. The peak at 981 nm, which coincides with the lower energy peak in the absorption spectra, is due to the transition from the lowest sublevel of the excited state, $^2F_{5/2}$ (0'), to the lowest sublevel of the ground state, $^2F_{7/2}$ (0).

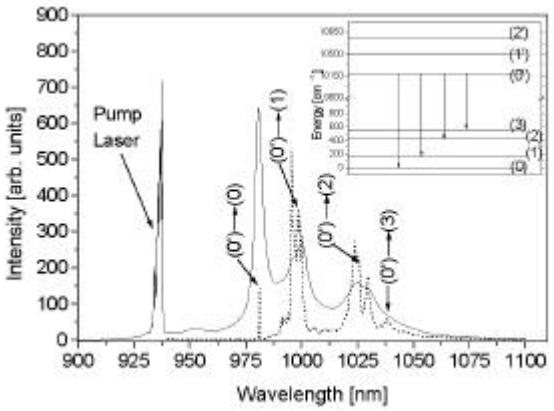

Figure 4.8 Room temperature (solid line) and low temperature (dotted line) emissions of Yb^{3+} in KLuW after 940 nm excitation

The values of the Stark levels of the ground state of Yb^{3+} in KREW were determined at low temperature. These are summarised in Table 4.3, determined from Table III of Paper V for KGW, Fig. 5 of Paper XI for KYW, Fig. 7, 8 and 9 of Paper III for KYbW and Fig. 1 of Paper VI and Fig. 2 of Paper X for KLuW.

Table 4.3 Stark levels of $^2F_{7/2}$ of Yb^{3+} in KREW determined at 10 K

Host	Energy position (cm^{-1})
KGW	0, 163, 385, 535
KYW	0, 165, 410, 542
KYbW	0, 168, 438, 555
KLuW	0,175, 435, 559

Strong changes were detected when the low-temperature and room-temperature emission spectra were compared. As Fig. 4.8 shows, at room temperature the bands were significantly broader. Figure 4.8 also shows the appearance of new bands, which emerge due to the thermal population of the excited sublevels of the $^2F_{5/2}$ state. The new line that appears at 952.5 nm may be associated with the transition from the $^2F_{5/2}$ (1') excited sublevel to the $^2F_{7/2}$ (0) lowest sublevel of the fundamental state.

At this point, it is important to note that the relative intensities of the emission lines may be different from those shown in the spectra in Fig. 4.8. According to our studies (see Paper III), the reabsorption phenomena of photoluminescence are important in the case of Yb^{3+}-doped materials and influence the shape of the emission spectra. Even if the experimental conditions used in this study minimise reabsorption, the size of this effect is difficult to estimate. Reabsorption may be important for the peak around 981 nm and for transitions originated from thermally populated sublevels of the $^2F_{5/2}$ state, so the actual intensity of the peak at 981 nm and of the energetically close-lying bands may be higher than those of Fig. 4.8.

4.5.1.3 Lifetime measurements

It is important to measure the lifetime of Yb^{3+} to characterise Yb^{3+} -doped KREW as laser materials. The lifetime was measured after pumping at 980 or 940 nm without distinction (the difference in pump wavelength had no effect on the lifetime values). To obtain accurate values of the lifetime in Yb^{3+} -doped KREW, radiation trapping must be taken into account because Yb^{3+} has a great deal of overlap between the absorption and emission bands. Because part of the emitted radiation from one Yb^{3+} ion can be reabsorbed by a neighbouring Yb^{3+} ion, the measured lifetime of a bulk sample does not generally indicate the true intrinsic emission lifetime. This is an important problem in highly doped KREW and therefore in KYbW, which is characterised by a large number of Yb^{3+} centres with very short distances between the Yb^{3+} ions. Also, the KREW refractive index is approximately 2 (see Fig 3.11), which leads to total internal reflection (TIR) of all radiation that impinges the sample-air interface greater than a certain angle (30º). TIR increases the emission pathlength in the crystal and artificially lengthens the observed lifetimes. To eliminate this effect, optically thin samples should be used for lifetime measurements. The problem of eliminating these effects is widely discussed in the literature and several solutions have been proposed [82,144, 145, 146].

The lifetime values of Yb^{3+} for the different hosts are given in Table 4.4 for very low concentration of Yb^{3+} to minimise radiation trapping.

Table 4.4 Experimental lifetime of Yb^{3+} in KREW

Host	Lifetime (ms) (bulk)
KGW	300
KYW	300
KYbW	600
KLuW	375

Note the high value of 600 μs for KYbW. This is due to radiation trapping because of the 100% content of Yb^{3+} and TIR effects. We tried to eliminate radiation trapping and TIR for KYbW because of the high concentration of Yb^{3+}, which considerably increased the lifetime. To do this, fine-powder KYbW was used with 25-60 μm in diameter and ethylene-glycol (EG) for refractive-index-matching.

The results of these experiments are in Paper III for KYbW. Yb^{3+} -doped KLuW was measured in bulk, but at a low Yb^{3+} concentration to minimise radiation trapping (see Paper X).

The shortest lifetime found for KYbW in diluted samples (200 μs) suggests that TIR and radiation trapping were efficiently eliminated and makes us confident that it is close to the intrinsic single-ion lifetime. This value is closer to, but still below, the recently measured 300 μs for KYW crystals with a low doping concentration of Yb^{3+} [82].

4.5.2 Erbium spectroscopy

4.5.2.1 Optical absorption

We performed the polarised optical absorption of Er^{3+} in KREW at room and cryogenic temperatures. The experiments were carried out with polarised light along the principal optical axes and the samples were oriented as described in Chapter 2. The spectral range measured from 300 to 1650 nm. 300 nm was the lower limit because the tungstates are non-transparent below this wavelength (see section 3.5.1 of Chapter 3) and 1650 nm was the upper limit because erbium does not absorb at longer wavelengths (see Fig. 1.3 of Chapter 1).

The spectra, the concentration of the ions and the thickness of the samples are given as results in the various Papers: the results for KGW are in Paper V, the results for KYW are in Paper IV and the results for KYbW are in Paper IX. The optical absorption of erbium in KLuW is currently

under study. From these experiments we determined the energy levels of erbium in this range: in order of increasing energy these were $^4I_{13/2}$, $^4I_{11/2}$, $^4I_{9/2}$, $^4F_{9/2}$, $^4S_{3/2}$, $^2H_{11/2}$, $^4F_{7/2}$, $^4F_{5/2}$, $^4F_{3/2}$, $^2H_{9/2}$, $^4G_{11/2}$, $^4G_{9/2}$ and $^2K_{15/2}$.

The same experiments were done at low temperatures to determine the Stark levels of the excited state. The spectra at low temperature are also shown in the various Papers.

Table 4.5 summarises the energy positions of the Stark levels of the excited states of erbium in KREW (from Papers IV, V and IX). The case of Er^{3+} in KLuW is currently under study. The sublevels of the $^4I_{11/2}$ level of Er^{3+} in KYbW were not determined because of the overlap with the $^2F_{5/2}$ level of Yb^{3+} and the high concentration of Yb^{3+} in this crystal.

The Judd-Ofelt analysis was performed from the room-temperature polarised optical absorption of the Er^{3+} -doped KYbW system and calculated the experimental and theoretical oscillator strength, the Judd-Ofelt parameters, the radiative transition probabilities (A_{ij}), the branching ratios (β_j) and the radiative lifetimes (τ_r). A brief explanation of the calculations is given in Paper IX and a fuller explanation of the Judd-Ofelt theory is published in references [147, 148]. The Judd-Ofelt parameters agree well with those for other tungstates such as KGW [131] and KYW [100], though they are slightly bigger due to the influence of the crystal field.

The energy position of the centre of gravity of each multiplet of Er^{3+} was compared in KGW, KYW and KYbW hosts. The difference between these centres of gravity is smallest for KYbW. Parallel to this, the splitting of each energy level into its sublevels is slightly greater in KYbW crystals than in KGW and KYW crystals (10 cm^{-1} on average for all energy levels). From these two observations, it is possible to conclude that the crystal field of KYbW is stronger than that of KGW, which agrees well with the smaller interatomic distances for KYbW [149] compared to those for KGW [125]. The Judd-Ofelt parameters of erbium in KYbW are larger than those in KGW [131] and KYW [100] (see Paper IX), and demonstrate this influence of the crystal field. On average, the values for KYbW are twice as large as those for KGW. The splitting of each energy level into its sublevels for KYW was more or less the same as for KGW (see Table 4.5) but we did not calculate the Judd-Ofelt parameters.

Table 4.5 Energy positions of the Stark levels of the excited energy levels of Er^{3+} in KREW

Host	Energy levels	Energy position (cm^{-1})
KGW Paper V	$^4I_{13/2}$	6517, 6547, 6574, 6603, 6662, 6713, 6725.
	$^4I_{11/2}$	10197, 10223, 10237, 10267, 10290, 10296
	$^4I_{9/2}$	12337, 12438, 12467, 12499, 12557.
	$^4F_{9/2}$	15170 15200, 15218, 15288, 15333.
	$^4S_{3/2}$	18327, 18388.
	$^2H_{11/2}$	19050, 19072, 19139, 19178, 19213, 19224.
	$^4F_{7/2}$	20441, 20485, 20510, 20577.
	$^4F_{5/2}$	22122, 22153, 22189.
	$^4F_{3/2}$	22469, 22556.
	$^2H_{9/2}$	24501, 24533, 24551, 24582, 24619.
	$^4G_{11/2}$	26231, 26344, 26401, 26438, 26449, 26454.
KYW Paper IV	$^4I_{13/2}$	6516, 6545, 6571, 6603, 6666, 6719, 6732.
	$^4I_{11/2}$	10188, 10213, 10229, 10261, 10284, 10290
	$^4I_{9/2}$	12335, 12434, 12467, 12497, 12557.
	$^4F_{9/2}$	15193, 15209, 15332, 15341, 15368.
	$^4S_{3/2}$	18316, 18380.
	$^2H_{11/2}$	19041, 19061, 19132, 19172, 19207, 19220.
	$^4F_{7/2}$	20430, 20477, 20501, 20573.
	$^4F_{5/2}$	22112, 22143, 22182.
	$^4F_{3/2}$	22459, 22552.
	$^2H_{9/2}$	24491, 24527, 24545, 24585, 24613.
	$^4G_{11/2}$	26219, 26235, 26333, 26390, 26440, 26462.
	$^4G_{9/2}$	27274, 27288, 27328, 27355, 27370.
	$^2K_{15/2}$	27496, 27563, 27650, 27776, 27940, 27983, 28008.
KYbW Paper VIII and Paper IX	$^4I_{13/2}$	6515, 6543, 6570, 6603, 6670, 6723, 6737.
	$^4I_{9/2}$	12336, 12441, 12468, 12498, 12556.
	$^4F_{9/2}$	15201, 15280, 15332, 15341, 15366.
	$^4S_{3/2}$	18308, 18376.
	$^2H_{11/2}$	19035, 19056, 19128, 19170, 19205, 19219.
	$^4F_{7/2}$	20421, 20471, 20497, 20573.
	$^4F_{5/2}$	22104, 22136, 22177.
	$^4F_{3/2}$	22450, 22551.
	$^2H_{9/2}$	24484, 24523, 24569, 24584, 24609.
	$^4G_{11/2}$	26208, 26223, 26326, 26386, 26434, 26457.
	$^4G_{9/2}$	27267, 27293, 27320, 27361, 27378.
	$^2K_{15/2}$	27484, 27568, 27641, 27735, 27936, 27978, 28000.
KErW Ref. [150]	$^4I_{13/2}$	6516, 6544, 6570, 6600, 6666, 6718, 6730.
	$^4I_{11/2}$	10188, 10213, 10229, 10260, 10284, 10290
	$^4I_{9/2}$	12392, 12436, 12466, 12497, 12557.
	$^4F_{9/2}$	15200, 15215, 15285, 15330, 15365.
	$^4S_{3/2}$	18314, 18378.

4.5.2.2 Optical emission

The luminescence of erbium was analysed in the above-mentioned tungstates for the infrared 1.5 μm emission, and for the visible and ultraviolet emissions in the 300-1650 nm range. The pump wavelength was 940 or 980 nm, without distinction, and 798 nm (resonant to the $^4I_{9/2}$ level of erbium).

The Reciprocity method was also used to calculate the emission cross-section for all three polarisations of the $^4I_{13/2} \rightarrow {}^4I_{15/2}$ transition, from the absorption cross-section spectra at room temperature. These spectra are shown in Fig. 3 of Paper V for KGW, Fig. 5 of Paper IV for KYW and Fig. 5 of Paper IX for KYbW. Er -doped KLuW crystals are currently under study. By way of example, the experimental emission and the calculated emission spectra (average of the three polarised spectra) were compared in Fig. 4.9 in the 1.425 – 1.625 μm (7018 - 6154 cm^{-1}) range. The maximum absorption cross-section for the polarisation parallel to the N_m principal optical direction, which corresponds approximately to the 1.534 μm (6519 cm^{-1}) signal, was around $2.6x10^{-20}$ cm^2. This absorption cross-section led to a calculated emission cross-section of $2.7x10^{-20}$ cm^2, which is similar to those published by Kuleshov et al. [100]. The maximum calculated emission cross-section corresponded to the 1.534 μm (6519 cm^{-1}) energy position.

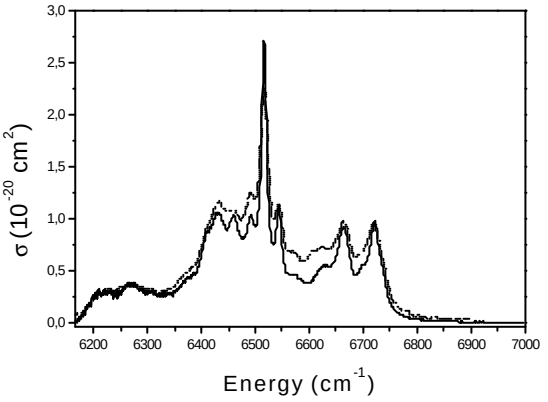

Figure 4.9 Room-temperature 1.5 mm emission cross-section of Er^{3+} in KYbW. Experimental curve (dotted line) and calculated curve (solid line)

The Fuchtbauer-Ladenburg (F-L) method was used to compare the experimental unpolarised infrared emission ($^4I_{13/2} \rightarrow {}^4I_{15/2}$ transition) with the spectrum calculated with the Reciprocity method by taking into account the average of the three spectra for each polarisation and the spectrum calculated with the F-L method for Er:KYbW (see Fig. 6 of Paper IX). A brief description of the F-L calculations is given in Paper IX and a fuller description of the method is given in references [138, 143]. The experimental spectrum was rescaled to match the calculated spectra and compare its shape. The main conclusion was that all three spectra were very similar, except at short wavelengths, because the reabsorption effect is greater and the Reciprocity method does not consider this.

The fluorescence of the 1.5 μm emission was also recorded at 10 K to determine the splitting of the ground state of Er^{3+} after 980 nm pumping. The spectra consisted of eight main signals, corresponding to the transitions from the lowest sublevel of the $^4I_{13/2}$ of erbium to the eight sublevels of the ground state. Other peaks, related to the transition from the second and third sublevels of the excited estate to the eight sublevels of the ground state, appeared. These were shown in Fig. 4.10. This is observed due to the coincidence between the sublevels of the excited $^4I_{13/2}$ level and the sublevels of the ground state. Figure 4.10 shows the low temperature 1.5 μm emission of Er^{3+} in KGW at 10 K.

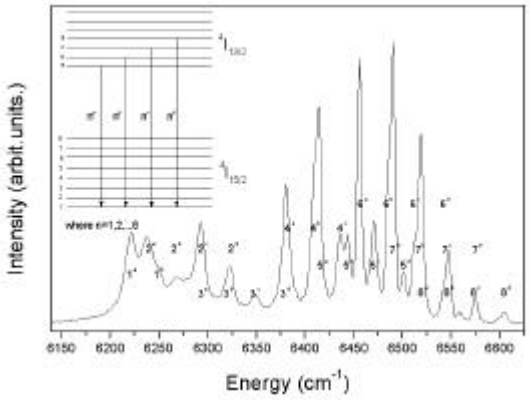

Figure 4.10 Low temperature 1.5 mm emission of Er^{3+} in KGW

This emission can be used to determine the splitting of the ground state of erbium due to the $^4I_{13/2} \rightarrow {}^4I_{15/2}$ transition. This is shown in Table 4.6 from Fig. 9 of Paper V for KGW, Fig. 10 of Paper IV for KYW and Fig. 7 of Paper IX for KYbW.

Table 4.6 Splitting of the ground state ($^4I_{15/2}$) of erbium for the KREW

Host	Energy position (cm^{-1})
KGW	0, 29, 64, 105, 139, 227, 282, 298
KYW	0, 28, 62, 106, 137, 235, 291, 307
KYbW	0, 26, 61, 106, 138, 239, 298, 311
KErW	0, 27, 60, 103, 133, 230, 288, 302

Figure 4.11 shows schematically the generation of the 1.5 μm in co-doped samples.

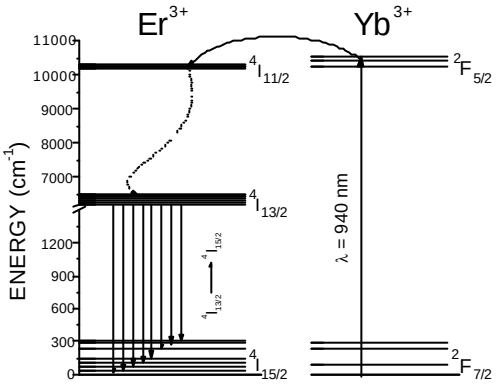

Figure 4.11 Scheme of the pump-emission and energy transfer for the generation of the 1.5 mm emission of Er^{3+} in KREW co-doped with Yb^{3+}

The green emission of erbium ($^4S_{3/2} \rightarrow {}^4I_{15/2}$ transition) was also analysed in the 18518-17857 cm^{-1} (540-560 nm) range after pumping at 980 or 940 nm. Figure 4.12 shows the absorption and emission cross-section spectra of the $^4I_{15/2} \rightarrow {}^4S_{3/2}$ transition and the $^4S_{3/2} \rightarrow {}^4I_{15/2}$ transition, respectively, for KGW. The F-L method was used to calculate the emission cross-section. Note that a maximum emission cross-section value of 1.85×10^{-20} cm^2 was calculated at 553 nm (18083 cm^{-1}). This was close to the value in Er:YLF at 561 nm, which was the first up-conversion laser in the green spectral range, and also close to the value in Er:YAG at 561 nm [56]. The gain cross-section for this transition was calculated from the expression, $\sigma_{gain} = P\sigma_e - (1-P)\sigma_{abs}$, where σ_{gain} is

the gain cross-section, σ_e is the calculated emission cross-section, σ_{abs} is the absorption cross-section and P is the population inversion rate. The inset to Fig. 4.12 shows the gain cross-section for several inversions of population rates (40%, 50% and 60%). Note that for a 60% rate, a positive gain was expected for wavelengths between 545 nm (18349 cm^{-1}) and 564 nm (17730 cm^{-1}), with a maximum gain cross-section of 0.94×10^{-20} cm^2 at 553 nm (18083 cm^{-1}).

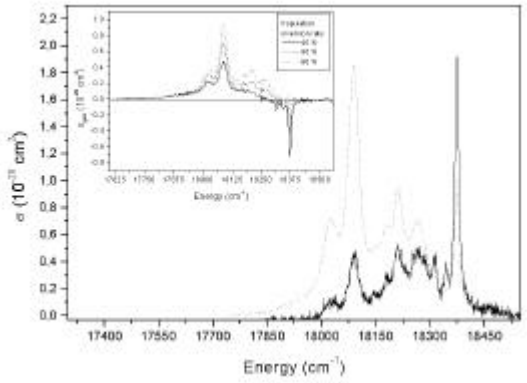

Figure 4.12 Absorption (solid line) and emission (dotted) cross-section of the green emission of Er^{3+} in KGW

The green emission of Er^{3+} was systematically recorded at low temperature determining again the splitting of the ground state of erbium due to the $^4S_{3/2} \rightarrow {}^4I_{15/2}$ transition. The values agreed with those obtained using the 1.5 μm emission. The spectra are shown in Fig. 3 of Paper VIII for KGW, Fig. 4 of Paper X for KYW and Fig. 1 of Paper VII for KYbW.

Figure 4.13 shows the green emission of Er^{3+} in KYbW at 10 K. As with the 1.5 μm emission, the spectrum is also dominated by eight main signals corresponding to the transitions from the lowest sublevel of the excited $^4S_{3/2}$ level to the eight sublevels of the ground state. Other signals appear at an energy difference corresponding to that between the two excited sublevels of $^4S_{3/2}$.

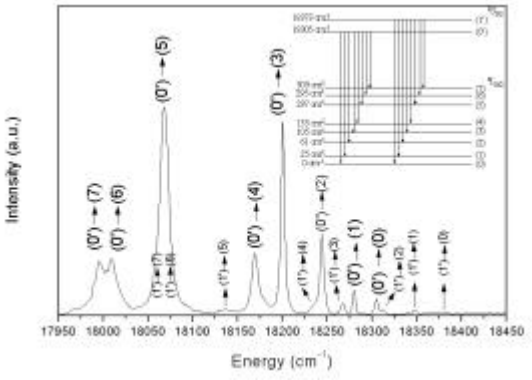

Figure 4.13 Low temperature green emission of Er^{3+} in KYbW

The ultraviolet and the other visible emissions were analysed and their transitions assigned. In this way, the $^4G_{11/2} \rightarrow {}^4I_{15/2}$ is for the 383 nm emission, $^2H_{9/2} \rightarrow {}^4I_{15/2}$ is for 407 nm, $^4F_{5/2} \rightarrow {}^4I_{15/2}$ is for 457 nm, $^2K_{15/2} \rightarrow {}^4I_{13/2}$ is for 474 nm, $^2H_{11/2} \rightarrow {}^4I_{15/2}$ is for 525 nm, $^4S_{3/2} \rightarrow {}^4I_{15/2}$ is for 552 nm (described previously), $^4F_{9/2} \rightarrow {}^4I_{15/2}$ is for 652 nm, $^2H_{9/2} \rightarrow {}^4I_{11/2}$ is for 696 nm, $^2P_{3/2} \rightarrow {}^4S_{3/2}$ is for 772 nm, $^4I_{9/2} \rightarrow {}^4I_{15/2}$ is for 801 nm, $^2H_{9/2} \rightarrow {}^4I_{9/2}$ is for 814 nm, and $^4S_{3/2} \rightarrow {}^4I_{13/2}$ is for 848 nm. The spectra are shown in Fig. 1 of Paper XII for KYbW and in Fig. 1 of Paper XI for KYW. Figure 4.14 shows the ultraviolet and visible emission of erbium in KYbW at room temperature and at 10 K. These transitions were corroborated by the difference in energy between the sublevels of the emitting and arrival energy levels (see Table 4.5).

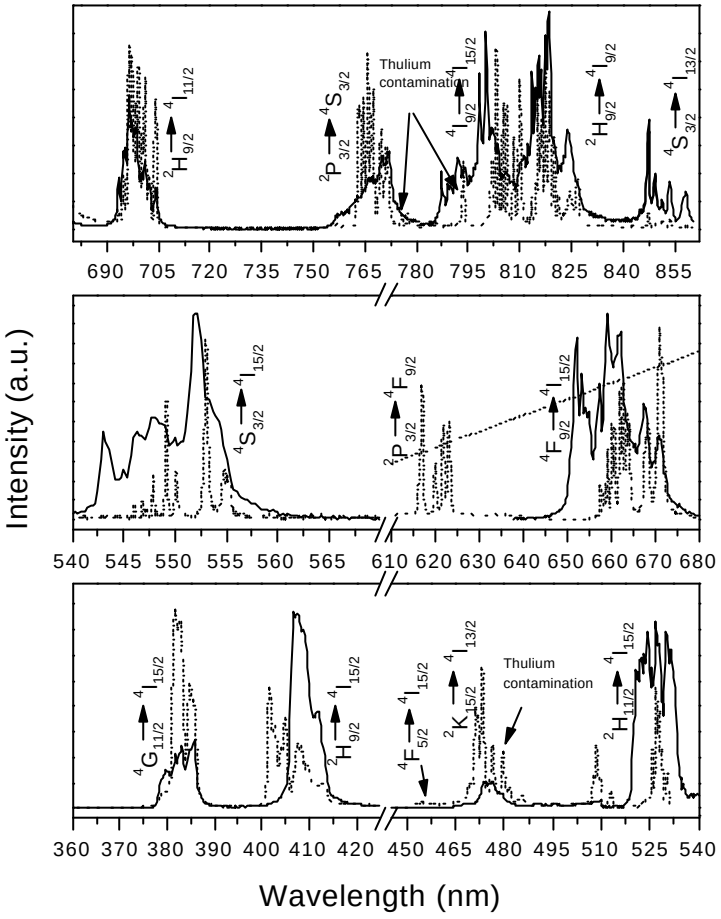

Figure 4.14 Room temperature (solid line) and low temperature (dotted line) visible and ultraviolet emissions of Er^{3+} in KYbW

Figure 4.15 shows a schematic diagram for the generation of the ultraviolet and visible emissions in Er^{3+} -doped KREW co-doped with Yb^{3+}.

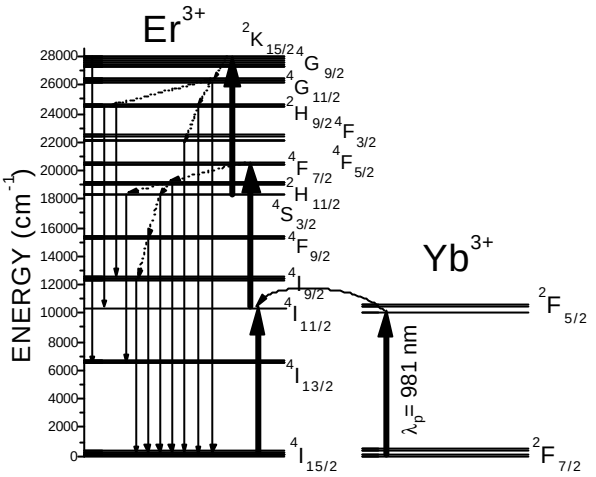

Figure 4.15 Scheme of the pump-emission and energy transfer for the generation of the ultraviolet and visible emissions of Er^{3+} in KREW co-doped with Yb^{3+}

We also pumped the erbium -doped crystals in the case of KYW at 798 nm resonantly to the $^4I_{9/2}$ level of erbium without direct ytterbium excitation and found an emission in the 960-1065 nm that corresponded to ytterbium. This is clear proof of the back-energy transfer from erbium to ytterbium. Figure 5 of Paper XI shows this emission at RT and 10 K, from where the Stark levels of the ground were deduced. These were 0, 165, 410 and 542 cm^{-1}.

4.5.2.3 Lifetime measurements

The lifetimes of the above-mentioned emissions of Er^{3+} depended strongly on the dopant concentration. These values are given in the various Papers: Table 4 of Paper V shows the lifetime of the $^4I_{13/2}$ level of Er^{3+} in KGW at several dopant concentrations (Er^{3+} and Yb^{3+}); Table 4 of Paper IX shows the lifetime of the $^4I_{13/2}$ level at several Er^{3+} concentrations in KYbW. Table 1 of Paper VIII shows the lifetime of the $^4S_{3/2}$ level of Er^{3+} in KGW at several Yb^{3+} concentrations. Table 1 of Paper XI shows the lifetime of the visible and ultraviolet emissions for KYW and Table 1 of Paper XII shows the lifetime of the visible and ultraviolet emissions for KYbW. Figure 3 of Paper VII shows the decay curves of the $^4S_{3/2}$ level due to the sensitisation of Yb^{3+} in KYbW.

CHAPTER 5

CONTINUOUS-WAVE AND PULSED LASER OPERATION OF $KYb(WO_4)_2$ AND Yb^{3+}:$KLu(WO_4)_2$ SINGLE CRYSTALS

In this Chapter, the results on the laser operation of Yb^{3+} in KLuW and KYbW crystals are briefly presented. The laser operation of Yb:KLuW was performed in continuous-wave regime and that of KYbW was performed in pulsed regime.

Table of contents

We will refer to the following papers to explain the results included in this Chapter.

PAPER III: Pujol, M.C.; Bursukova, M; Güell, F.; **Mateos, X**.; Solé, R.; Gavaldà, Jna.; Aguiló, M; Massons,J.; Díaz, F.; Klopp, P.; Grieber, U. and Petrov, V. "Growth, optical characterization and laser operation of a stoichiometric crystal $KYb(WO_4)_2$." *Physical Review B*, **65**, 165121:1-11 (2002).

PAPER VI: **X. Mateos**, V. Petrov, M. Aguiló, R. Solé, Jna. Gavaldà, J. Massons, F. Díaz, U.Griebner, "Continuous Wave Laser Oscillation of Yb^{3+} in Monoclinic $KLu(WO_4)_2$." *IEEE Journal of Quantum Electronics*, **40**, 1056-1059 (2004).

PAPER XII: P. Klopp, U. Griebner, and V. Petrov, **X. Mateos**, M. A. Bursukova, M. C. Pujol, R. Solé, Jna. Gavaldà, M. Aguiló, F. Güell, J. Massons, T. Kirilov, and F. Diaz, "Laser operation of a new stoichiometric crystal $KYb(WO_4)_2$", *Applied Physics B*, **74**, 185 (2002).

5.1 Yb^{3+}: $KRE(WO_4)_2$, a quasi-three level gain medium

The term quasi-three-level is sometimes used to be distinguished from true three-level lasers. In quasi-three-level lasers, the lower laser level is partially occupied in thermal equilibrium and such lasers have properties that are intermediate between true three-level systems and four-level lasers. In the case of Yb^{3+} ions in monoclinic double tungstates, the system configures a quasi-three-level laser as can be seen in Fig. 5.1 for a pump wavelength corresponding to the maximum of absorption ≈ 980 nm.

Laser action occurs most readily in the strong emission transition around 1070 nm for KYbW and around 1040 for Yb:KLuW between the lowest Stark level of the $^2F_{5/2}$ manifold at 10188 cm^{-1} for KYbW and 10187 cm^{-1} for Yb:KLuW, and the highest Stark level of the ground $^2F_{7/2}$ manifold (555 cm^{-1} for KYbW and 559 cm^{-1} for Yb:KLuW). At

room-temperature, the lowest Stark level contains an important thermal population. Thus, near room temperature, the Yb^{3+} laser has a quasi-three-level character.

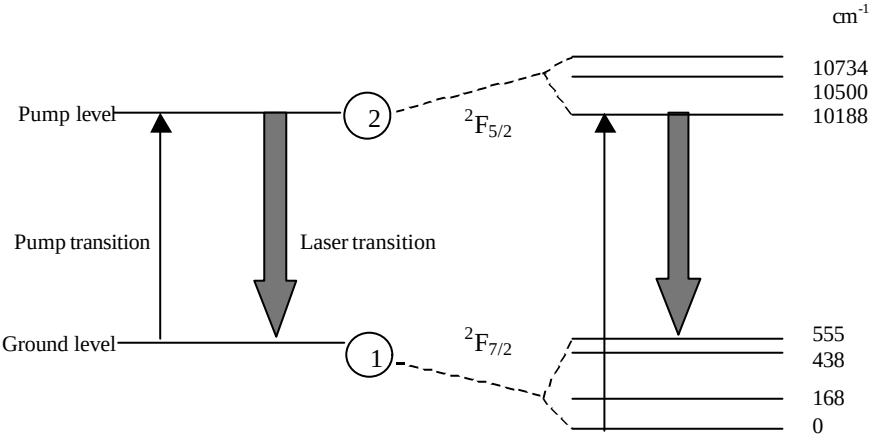

Figure 5.1 Simplified energy-level diagram of Yb^{3+} in KYbW. A quasi-three-level laser

The pump around 960 and 920 nm conforms the schemes depicted in Fig. 5.2 according to the absorption spectrum of Yb^{3+} in monoclinic double tungstates (see Fig. 4.5).

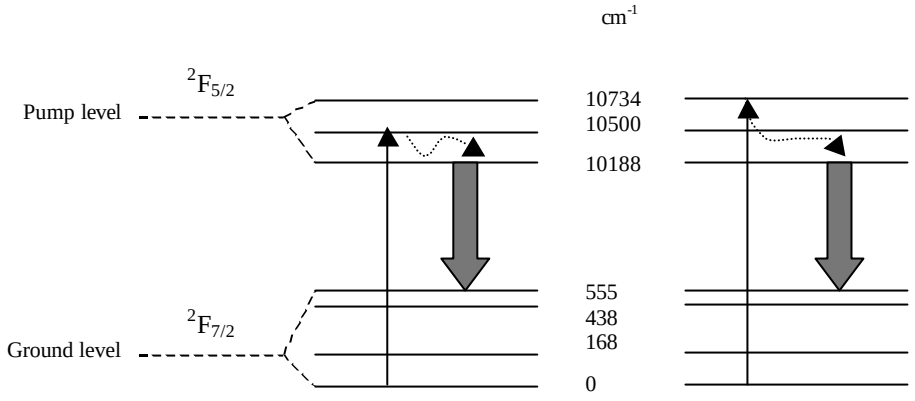

Figure 5.2 Pump-laser schemes of Yb^{3+} in KYbW at two pump wavelengths, at 963 nm (left) and at 922 nm (right)

Lower heat generation can be achieved by pumping at longer wavelengths, for example at 1025 nm, where the electrons are excited from the third Stark level of the ground state to the lower Stark level of the excited $^2F_{5/2}$ level. In this way it was published this material to provide the smallest laser quantum defect [151].

The steady-state photon rate equation predicts that, above threshold, the inversion density and the gain of a laser are clamped at their threshold values; the round-trip gain of the cavity is equal to the round-trip loss. With increased pumping, the gain remains fixed while the photon number and the output of the laser increase.

Because the photon number and the output intensity of the laser are linear functions of the pump rate, the efficiency of a laser is often discussed in terms of the slope efficiency η_s. Slope efficiency is defined as the ratio of the change in output power to the change in pump power of a laser once it has reached threshold, and is determined by five factors: the pump efficiency η_p, the area efficiency η_a, the inversion efficiency η_i, the quantum efficiency η_q, and the output-coupling efficiency η_0. Mathematically, $\eta_s=\eta_p\eta_a\eta_i\eta_q\eta_o$. The pump efficiency is the ratio of the energy absorbed by the gain medium to the energy of the pump source. In an optically pumped laser, part of the incident optical energy may be reflected by the gain medium and part may be transmitted.

Both of these effects decrease the pump efficiency. The area efficiency is a measure of how well the pumped volume is used by the oscillating mode. If the cross-section of the pumped volume is much larger that the cross-section of the lasing mode, only a small portion of the pumped volume contributes to the gain of the system, and the area efficiency will be low. For a longitudinally pumped laser, the area efficiency can often be approximated by $\eta_a = 1/((r^2_p/r^2_m) + 1)$, where r_p is the radius of the pump beam and r_m is the radius of the oscillating mode. The inversion efficiency is the ratio of the energy of a photon created during lasing to the energy required to invert one active ion. In an optically pumped system, the inversion efficiency is the ratio of the energy of a photon at the oscillating frequency to the energy of an absorbed pump photon. The difference between the energies of the absorbed and emitted photons is referred to as the quantum defect. The quantum efficiency is the fraction of the inverted ions that emit a photon into the oscillating mode. For an optically pumped system, 100% quantum efficiency implies that each absorbed pump photon results in one photon at the oscillating frequency. Finally, the output-coupling efficiency is the ratio of the output coupling to the total round-trip loss of the laser cavity.
The total efficiency of a laser (power out divided by power in) is dependent on the slope efficiency and the laser threshold. For a constant slope efficiency

$$\eta = \eta_s (1-(P_{th}/P_p)) \qquad [5.1]$$

where P_p is the total pump power and P_{th} is the pump power required to reach threshold.

5.2 Continuous-wave (CW) laser operation of Yb^{3+}:KLuW single crystals

To generate laser radiation from Yb^{3+}-doped KLuW crystals, we tested 5 and 10 mol % Yb^{3+}-content in the solution samples. The thickness of the 5 and 10% Yb:KLuW samples were 2.8 and 2.2 mm, respectively. All samples were cut and polished with their parallel faces normal to the N_p-principal optical axis and polarisation along the N_m principal optical axis, as described in Chapter 2. The choice of polarisation is important because it guarantees maximum emission cross-section and amplification. The samples were inserted under Brewster angle between the folding mirrors (described in Section 2.9 of Chapter 2) of a resonator (illustrated in Fig. 2.7 of Chapter 2).

The crystals were pumped by the two pump sources also described in Chapter 2, a Ti:sapphire laser and a diode (InGaAs) laser. Conversion efficiencies as high as 50% and output powers of the order of 1 W without actively cooling the crystal around 1 μm were achieved from Yb^{3+} under Ti:sapphire pump source. The results obtained at the optimum λ_P with the two Yb:KLuW samples are shown in Fig. 5.3 for two values of T_{OC}: 2.8% (a, c) and 5% (b, d). The complete procedure and results of the CW laser operation of Yb^{3+} in KLuW are reported in Paper VI and Paper X.

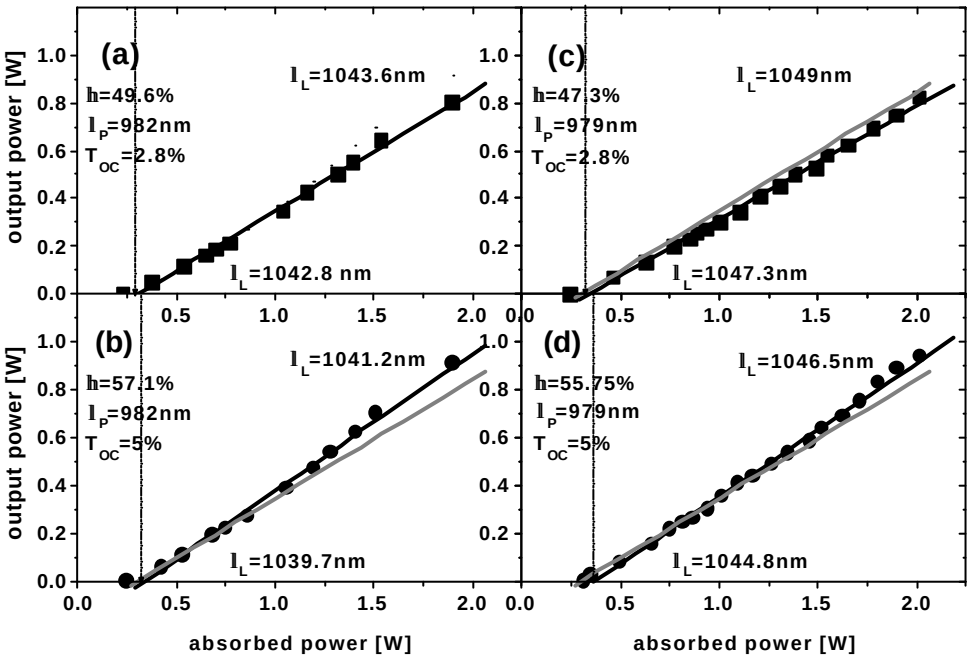

Figure 5.3 Output power P_{out} versus absorbed power P_{abs} in double pass (symbols) obtained at the corresponding optimum λ_P and linear fits (black lines) for calculation of the slope efficiency η for the 5% (a, b) and 10% (c, d) Yb-doped KLuW samples and two different output couplings (T_{OC}). The wavelength λ_L is indicated both at threshold (bottom values) and at maximum P_{out} (top values). The gray lines in (b), (c) and (d) are only guiding and have the same slope as the black line in (a). The thin vertical lines indicate the extrapolated thresholds.

Diode pumping at 980 nm was also demonstrated. Pumping with the laser diode was applied only to the 5% Yb^{3+}-doped KLuW sample because of the lower absorption of this sample. Output power versus absorbed power was recorded at the optimum pump wavelength (980 nm) (see Fig.

5.3). No saturation of the absorption took place in this case because of the low pump intensity. The total pump power incident on the sample was absorbed in the first passage through the crystal. This increased reabsorption losses, and therefore reduced slope and maximum efficiencies, and increased oscillation thresholds.

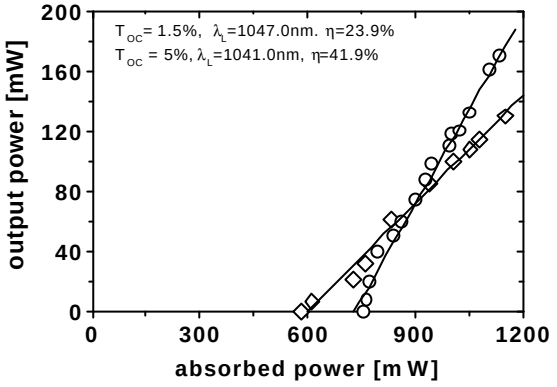

Figure 5.4 Slope efficiencies of the diode-pumped Yb:KLuW laser for T_{oc} (Transmission of the output coupler) of 1.5 (rhombuses) and 5% (circles)

5.3 Pulsed laser operation of KYbW single crystals

The sample used for laser experiments in the pulsed regime was a 0.5 mm thin KYbW crystal with a resonator design (also described in Section 2.9 of Chapter 2 and illustrated in Fig. 2.6 of Chapter 2). The thin plane of KYbW was cut and oriented for propagation along the $\boldsymbol{b}(N_p)$ axis and polarisation along the N_m principal optical axis, as with Yb^{3+} -doped KLuW crystals. The pump source was the CW Ti:sapphire laser reported above.

Lasing on the $^2F_{5/2} \rightarrow {}^2F_{7/2}$ transition of Yb^{3+} at room temperature was achieved near 1074 nm with >41% slope efficiency (>26% maximum conversion efficiency).

This new laser material holds great promise for diode-pumped high-power lasers, thin disk and waveguide designs, and for ultrashort (ps/fs) pulse laser systems.

Figure 5.5 shows the output power of the KYbW laser measured at 1074 nm as a function of the absorbed pump power for two pump wavelengths (922 and 963 nm). The first of these lies on the short wavelength wing of the absorption curve, and the second lies in the dip of the absorption

curve. The maximum output power corresponded to a conversion efficiency of 26-27% with respect to the absorbed pump power. The slope efficiency with respect to the absorbed power estimated from Fig. 5.5 was 41% for pumping at 963 and 44% for pumping at 922 nm. These values were greater than the slope efficiency (27 %) recently reported in a similar quasi-CW regime with stoichiometric YbAG [6]. Note that in our case the free-running wavelength was 1074 nm, which was far from the maximum of the fluorescence curve and can be explained by reabsorption effects at shorter wavelengths.

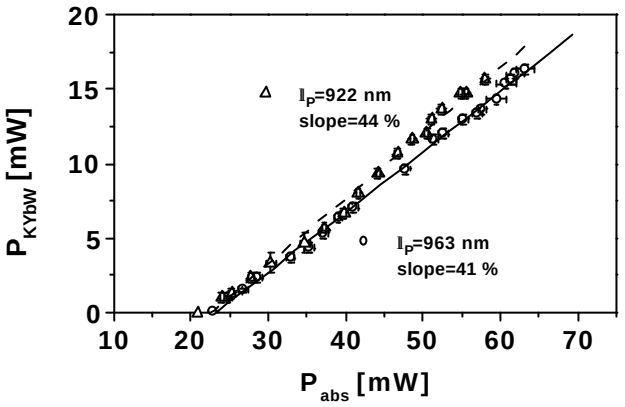

Figure 5.5 Slope efficiencies of KYbW laser at two pump wavelenghts (922 and 963 nm)

Full descriptions of the procedure and results of the pulsed laser operation of KYbW are given in Paper III and Paper XII.

Such highly Yb^{3+}-doped materials are potentially interesting for thin film laser designs which profit from the relaxed requirements to the pump laser beam quality and the possibility for efficient transversal cooling, especially in the high power regime, thanks to the small quantum defect and the absence of excited state absorption and up-conversion processes characteristic of the Yb^{3+}-ion. Monoclinic double tungstates possess the additional advantage of exceptionally large absorption and emission cross sections, however, their poor thermo-mechanical properties set a challenge for the manufacturing of active elements with a thickness less than 100 µm corresponding to the absorption length. Epitaxial growth of doped/undoped composites is a promising solution to this problem, however, the crystal lattice mismatch of KYW and KYbW

seems to be the basic limitation on the achievable interface quality. The study of KLuW as a new host for the Yb^{3+}-ion was motivated on the first place by the closer unit cell parameters of KYbW and KLuW (0.02…0.5% differences against 0.4…1% between KYbW and KYW), which is seen as a prerequisite for the growth of high quality KYbW/KLuW epitaxies and, in second place because of the close refractive indexes of KYbW and KLuW crystals, making more homogeneous the light path.

The relatively broad transition width of the 1070 nm (KYbW) and 1040 nm (Yb:KLuW) emission should allow for the generation of subpicosecond duration pulses from the Yb:KREW gain media. Ultrashort pulses with pulse widths in the picosecond or femtosecond regime are obtained from solid-state lasers by mode locking. Employing this technique, which phase-locks the longitudinal modes of the laser, the pulse width is inversely related to the bandwidth of the laser emission. The mode-locking experiments on KLuW:Yb is now under study also in collaboration with the laboratories of the *Max-Born Institute for Non-linear Optics and Ultrafast Spectroscopy.*

FINAL CONCLUSIONS

FINAL CONCLUSIONS

The most important results from this study are, firstly, the obtention of the monoclinic phase of the tungstates in a single crystal form that belong to the family of $KRE(WO_4)_2$, where RE denotes Y^{3+}, Gd^{3+}, Yb^{3+}, Er^{3+} and Lu^{3+}, doped with Yb^{3+} and Er^{3+} ions at several concentrations, and secondly, the characterisation of such materials from the compositional, structural, morphological and optical points of view. These studies were extended not only to un-doped materials but also to Yb^{3+} -single doped, Er^{3+} -single doped and Yb^{3+}, Er^{3+} co-doped materials. The generation of laser radiation from Yb^{3+} was also investigated.

The double tungstates were obtained in their monoclinic phase using the high-temperature crystal-growth method known as Top-Seeded-Solution Growth and using potassium pyrotungstate, $K_2W_2O_7$ as solvent. The solvent was used because the direct cooling from the melt of the predecessor materials leads to the crystallisation of the undesired tetragonal phase. The solvent decreased the crystallisation temperature and the desired monoclinic phase therefore appeared.

X-ray powder and single crystal X-ray diffraction have led to the resolution and refinement of the crystalline structure of the tungstates. By varying the temperature, the crystalline cell parameters change and the linear thermal expansion tensor was determined for each host.

Basically, the optical characterisation of such materials involved the study of three important optical parameters. The first one, was the range of the wavelengths in which the materials present optical transparency, (also called the optical transparency window), which is necessary to determine whether the materials are transparent, and in which degree they are in the excitation and emission wavelengths. The second one, was orientation of the principal optical axes and the third was the dispersive chromatic curves. The results indicated a high degree of optical anisotropy.

The spectroscopic characterisation of the active ions was carried out in terms of the optical absorption between the room temperature and the cryogenic temperature (6K) in order to determine the energetic positions of the electronic levels of the ions, the energetic positions of the Stark levels of the electronic levels of the ions and, the changes in electronic population of the Stark levels with temperature. This study was applied to Yb^{3+} and Er^{3+} in all matrices with polarised light parallel to the three principal optical directions. Moreover, the luminescence generated by the active ions was studied, which involved the optical emission and the lifetime measurements of the emitting levels of fluorescence. The emission was also studied between the

room temperature and the cryogenic temperature to determine the most important emissions of the Yb^{3+} and Er^{3+} ions. In this way, he Stark levels of the ground or fundamental state of such ions were determined for each host. The lifetime, which was measured at room temperature, was used to characterise the emitting levels of fluorescence. The most important emissions were studied because of their potential applications. These were 1.0 μm for Yb^{3+} and 1.5 μm and 550 nm for Er^{3+}. Some parameters such as the emission cross-section and the gain cross-section of the above-mentioned emissions were determined.

For the samples containing Yb^{3+} and Er^{3+}, the energy transfer between the two ions was studied by determining the changes in the lifetimes of their emissions as the concentration of dopants changed. The spectroscopic results indicated that these are very promising materials, specially the Yb:tungstates, which have a high degree of absorption and emission cross-sections, and lifetimes that are suitable for population inversion, which is necessary for laser generation. Er^{3+} ions presented good spectroscopic properties for its 1.5 μm emission.

Finally, laser radiation was successfully generated from Yb^{3+} in KYbW and KLuW crystals, with highly promising properties. These experiments were carried out in the laboratories of the *Max-Born Institute for Nonlinear Optics and Ultrafast Spectroscopy* in Berlin (Germany). Laser radiation was generated in continuous wave regime for Yb^{3+} in KLuW and in pulsed regime for KYbW. Two pump lasers, a Ti:sapphire laser and a diode (InGaAs) laser, were used. These two new laser materials have great promise for diode-pumped high-power lasers, thin-disk and waveguide designs and ultrashort (picosecond/femtosecond) pulse laser systems.

REFERENCES

[1] A.L. Schawlow, C.H. Townes, *Phys. Rev.*, **112**, 1940 (1958).

[2] T.H. Maiman, *Nature*, **187**, 493 (1960).

[3] P.P. Sorokin, M.J. Stevenson, *Phys. Rev. Lett.*, **5**, 557 (1960).

[4] E. Snitzer, *Phys. Rev. Lett*., **7**, 444 (1961).

[5] L.F. Johnson, L. Nassau, *Proc. IRE*, **49**, 1704 (1961).

[6] J.E. Geusic, H.M. Marcos, L.G. Van Uitert, *Appl. Phys. Lett*., **4**, 182 (1964).

[7] W.F. Krupke and L.L. Chase, *Opt. Quantum Electron*., **22**, pp. S1-S22 (1990).

[8] Mool C. Gupta, 1997. *Handbook of Photonics*, CRC Press LLC. Boca Raton, Florida.

[9] William P. Risk, Timothy R. Gosnell and Arto V. Nurmikko, 2003. *Compact blue-green lasers*, Cambridge University Press. U.K.

[10] William F. Krupke, *IEEE J. on selected topics in Q. Electron*. **6**, 1287-1296, 2000.

[11] Tso Yee Fan and R. L. Byer, *IEEE J. of Q. Electron*, **24**, 895-912 (1988).

[12] F. D. Patel, E. C. Honea, J. Speth, S. A. Payne, R. Hutcheson, and R. Equal, *IEEE J. Quantum Electron*. **37**, 135 (2001).

[13] K. Nassau, A. M. Broyer, *J. Appl. Phys.*, **33**, 3064 (1962).

[14] A.A. Kaminskii, P. V. Kletsov, L. Li and A.A. Pavlyuk, *Kvantovaya Elektron.* (Moscow), **4**, 113 (1971).

[15] A.A. Kaminskii, A.A. Pavlyuk, I.F. Bolashov, V.A. Berenberg, V,V, Lyubchencko, V.A. Federov, T.I. Butaeva and L.I. Bobovich, *Izv. Akad. Nauk SSSR Neorg. Mater.*, **14**, 2256 (1978).

[16] A.A. Kaminskii, A.A. Pavlyuk, P.V. Kletsov, I. F. Bolashov, V. A. Berenberg, S. E. Sarkisov, V. A. Fedorov, M. V. Petrov and V. V. Lyubchenko, *Izv. Akad. Nauk SSSR Neorg. Mater*, **13**, 582 (1977).

[17] A.A. Mak, V.A. Fromzel and A.A. Shcherbakov, *Izv. Akad. Nauk SSSR Ser. Fiz.*, **48**, 1466 (1984).

[18] I.I. Kuratev, *Izv. Akad. Nauk SSSR Ser. Fiz*., **48**, 1564 (1984).

[19] A.A. Kaminskii, H.R. Verdun, W. Koechner, F.A. Kuznetsov and A.A. Pavlyuk, *Kvantovaya Electron.* (Moscow), **19**, 941 (1992).

[20] K. A. Stankov and Marawsky, *Appl. Phys. B*., **61**, 213 (1995).

[21] A.M. Ivanyuk, M.A. P.A. Schachverdov, V.D. Belyaev, Ter-Pogosyan and V.L. Ermolaev, *Opt. Spektrosk*., **62**, 961 (1985) [*Opt. Spectrosc.* (USSR) **58**, 589 (1985)].

[22] A.A. Kaminskii, N.S. Ustimenko, A.V Gulin, S.N. Bagaev ann A.A. Pavlyuk, *Dokl. Akad. Nauk*, **359**, 179 (1998) [*Sov. Phys. JETP* **43**, 148 (1998)].

[23] L. D. Deloach, S. A. Payne, L. L. Chase, L. K. Smith, W. L. Kway, and W. F. Krupke, *IEEE J. Quantum Electron.* **29**, 1179 (1993).

[24] X. Zou and H. Toratani, *Phys. Rev. B* **52**, 15889 (1995).

[25] W. F. Krupke, IEEE J. Sel. Topics Quantum Electron. **6**, 1287 (2000).

[26] V. Petrov, U. Griebner, D. Ehrt and W. Seeber, *Opt. Lett*., **22**, 408, (1997).

[27] C. Hönninger, F. Morier-Genoud, M. Moser, U. Keller, L.R. Brovelli and C. Harder, *Opt. Lett*, **23**, 126 (1998).

[28] C. Hönninger, R. Paschotta, M. Graf, F. Morier-Genoud, G. Zhang, M. Moser, S. Biswal, J. Ness, A. Braun, G. Mourou, I. Johnannsen, A. Giesen, W. Seeber and U. Keller, *Appl. Phys. B*, **69**, 3 (1999).

[29] C. Hönninger, G. Zhang, U. Keller and A. Giesen, *Opt. Lett*., **20**, 2402 (1995).

[30] F. Brunner, G. J. Spühler, J. Aus der Au, L. Krainer, F. Morier-Genoud, R. Paschotta, N. Lichtenstein, S. Weiss, C. Harder, A. A. Lagatsky, A. Abdolvand, N. V. Kuleshov and U. Keller, *Opt. Lett*, **25**, 1119 (2000).

[31] F. Druon, F. Balembois, P. Georges, A. Brun, A. Courjaud, C. Hönninger, F. Salin, A. Aron, F. Mougel, G. Aka and D. Vivien, *Opt. Lett.*, **25**, 423 (2000).

[32] A. A. Kaminskii, A. A. Pavlyuk, T. I. Butaeva, L. I. Bobovich, and V. V. Lyubchenko, *Inorg. Mat.* **15**, 424 (1979) [transl. from *Izvestiya Akademii Nauk SSSR, Neorganicheskie Materialy* **15**, 541 (1979)].

[33] T. Zayarniuk, M. T. Borowiec, V. P. Dyaknonov, H. Szymczak, e. Zubov, A. A. Pavlyuk and M. Baranski, *Conference on solid State Crystals 2000, Proc. SPIE*, **4412**, 280 (2001).

[34] T. Zayarniuk, M. T. Borowiec, V. P. Dyaknonov, K. Wozniak, L. Dobrzycki, I. Krynetski, E. Michalski, A. Szewczyk, A. Jedrzejczak, A. V. Prochorov, E. E. Zubov, Y. Bukhantsev, B. Kundys and H. Szymczak, *Conference on solid State Crystals 2002, Proc. SPIE*, **5136**, 109 (2003).

[35] A. Majchrowski, M.T. Borowiec, E. Michalski, J. Zmija, V. Dyakonov, H. Szymczak, T. Zayarnyuk and M. Baranski, *Cryst. Res. Techn.*, **36**, 283 (2001).

[36] P. V. Klevtsov, L. P. Kozeeva, *Soviet Physics - Doklady* **14**, 185 (1969) [transl. from *Doklady Akademii Nauk SSSR* **185**, 571 (1969)].

[37] M.T. Borowiec, A. Majchrowski, V. Domuchowski, V. P. Dyakonov, E. Michalski, T. Zayarniuk, J. Zmija and H. Szymczak, *Conference on solid State Crystals 2002, Proc. SPIE*, **5136**, 20 (2003).

[38] A. Giesen, H. Hügel, A. Voss, K. Wittig, U. Brauch and H. Opower, *Appl. Phys. B*, **58**, 365 (1994).

[39] U. Brauch, A. Giesen, M. Karszewski, C. Stewen and A. Voss, *Opt. Lett*, **20**, 713 (1995).

[40] K. Contag, M. Karszewski, C. Stewn, A. Giesen and H. Hügel, *Quant. Electron*., **29**, 697 (1999).

[41] C. L. Bonner, T. Bhutta, D.P. Sheperd and C. Tropper, *IEEE J. Quant. Electron*, **36**, 236 (2000).

[42] D. Pelenc, B. Chambaz, I. Chartier, B. Ferrand, C. Wyon, D. P. Sheperd, D. C. Hanna, A. C. Large and A. C. Tropper, *Opt. Commun.*, **115**, 491 (1995).

[43] M. C. Pujol, M. A. Bursukova, F. Güell, X. Mateos, R. Sole, J. Gavalda, M. Aguilo, J. Massons, F. Diaz, P. Klopp, U. Griebner, and V. Petrov, *Phys. Rev. B* **65**, 165121 (2002).

[44] P. Klopp, U. Griebner, V. Petrov, X. Mateos, M.A. Bursukova, M.C. Pujol, R. Sole, Jna. Gavaldà, M. Aguiló, F. Güell, J. Massons, T. Kirilov and F. Díaz, *Appl. Phys. B*. **74**, 185 (2002).

[45] P. Klopp, V. Petrov, U. Griebner, V. Nesterenko, V. Nikolov, M. Marinov, M. A. Bursukova and M. Galan, *Opt. Lett.* **28**, 322 (2003).

[46] A. Aznar, R. Sole, M. Aguilo, F. Diaz, U. Griebner, R. Grunwald, and V. Petrov, *Appl. Phys. Lett.* (2003), submitted.

[47] P. Klopp, V. Petrov and U. Griebner, *Jpn. J. Appl. Phys.*, **42**, L246 (2003).

[48] G. H. Dieke, 1968. *Spectra and Energy Levels of Rare Earth Ions in Crystals*, Wiley, New York.

[49] D.F. de Sousa, L.F. C. Zonetti, M.J.V. Bell, J.A. Sampaio, L.A.O. Nunes, M.L. Baesso, A.C. Bento and L.C.M. Miranda, *Appl. Phys. Lett.*, **74**, 908 (1999).

[50] R.M. Dwyer and M. Bass, 1977. *Lasers in Medicine*, Academic, New York, Vol, 3, p. 107, and references therein.

[51] K. Kincade, *Laser Focus World*, **73**, August (1996).

[52] G.J.Kintz, R. Allen and L. esterowitz, *Appl. Phys. Lett*., **50**, 1553 (1987).

[53] S. A. Pollack and M. Robinson, *Electron. Lett.*, **24**, 320 (1988).

[54] F.E. Auzel, *Proc. IEEE*, **61**, 758 (1973).

[55] P.E.-A. Möbert. E. Heumann and G. Huber. *Opt. Let*., **22**, 1412 **(**1997).

[56] T. Danger, J. Koetke, R. Brede, E. Heumann, G. Huber and B.H.T. Chai, *J. Appl. Phys*, **76**, 1413 (1994).

[57] L.F. Johnson, J.E. Geusic, L.G. Van Uitert, *Appl. Phys. Lett.*, **7**, 127 (1965).

[58] E.P.Chicklis, *Appl. Phys. Lett.*, **19**, 119 (1971).

[59] M.J. Weber, M. Bass, G.A. deMars, *J. Appl. Phys.*, **42**, 301 (1971).

[60] W.F. Krupke, J.B. Gruber, *J. Chem. Phys.*, **41**, 1225 (1964).

[61] Z. J. Kiss, R.C. Duncan, *Proc. IRE*, **50**, 1531 (1962).

[62] S.A. Pollack, *Proc. IEEE*, **51**, 1793 (1963).

[63] E. Snitzer, *Appl. Phsy. Lett.*, **6**, 45 (1965).

[64] K.O. White, E. H. Holt, *The erbium doped glass laser. Report ECOM-5294, U.S. Army,Fort Monmouth, NJ* (1970).

[65] M. Haase, J. Qiu, J. DePuydt and H. Cheng, *Appl.Phys. Lett.*, **59**, 1272 (1991).

[66] L. Goldberg and M.K. Chun, *Appl. Phys. Lett.*, **55**, 218 (1989).

[67] A. Feisst and P. Koidl, *Appl. Phys. Lett.* 47, 1125 (1985).

[68] L. F. Johnson and H.J. Guggennheim, *Appl. Phys. Lett.*, **19**, 44 (1971).

[69] J. Y. Allain, M. Monerie and H. Poignant,*Electron. Lett.*, **26**, 168 (1989).

[70] F. Auzel, *C.R. Acad. Sci. Paris*, **262**, 1016 (1966).

[71] F. Auzel, *C.R. Acad. Sci. Paris*, **263**, 819 (1966).

[72] A. J. Silversmith, W. Lenth and R. M. Macfarlane, *Appl. Phys. Lett*., **51**, 1977 (1987).

[73] R. M. Macfarlane, F. Tong, A. J. Silversmith, and W. Lenth, *Appl. Phys. Lett*., **52**, 1300 (1988).

[74] R. Brede, E. Heumann, J. Koetke, T. Danger, G. Huber and B. Chai, *Appl. Phys. Lett.*, **63**, 2030 (1993).

[75] R.A. McFarlane, *J. Opt. Soc. Am. B*, **11**, 871 (1994).

[76] T. Sandrock, E. Heumann, G. Huber and B.H.T. Chai, *Adv. Sol. Stat.* Laser, **1**, 550 (1996).

[77] D.S. Funk, J. G. Eden, J. S. Osinski and B. Lu, *Electron. Lett*., **33**, 1958 (1997).

[78] M.-F. Joubert, *Opt. Mat.* **11**, 181 (1999).

[79] N.V. Kuleshov, A.A. Lagatsky, A.V. Podlipensky, V. P. Mikhailov, E. Heumann, A. Diening and G. Huber, *OSA Proceedings on Advanced Solid State Lasers*, **10**, 415 (1997).

[80] A.A. Lagatsky, N.V. Kuleshov and V. P. Mikhailov, *Opt. Comm.*, **165**, 71 (1999).

[81] V.L. Kalashnikov, F. Mejid, I.G. Poloyko and V. P. Mikhailov, *Proc.SPIE – The International Society for Optical Engineering*, **3613**, 289 (1999).

[82] A.A. Demidovich, A. N. Kuzmin, G.I. Ryabsev, M.B. Danailov, W. Strek and A. N. Titov, *J. Alloys and Comp.*, **300-301**, 238 (2000).

[83] S. Rotyliano, V. Mikhailov, S. Schulz and A. Cable, *OSA Proceedings on Advanced Solid State Lasers*, **34**, 569 (2000).

[84] A.A. Lagatsky, A. Abdolvand and N.V. Kuleshov, *OSA Proceedings on Advanced Solid State Lasers*, **34**, 116 (2000).

[85] A.A. Lagatsky, A. Abdolvand and N.V. Kuleshov, *Conference on Lasers and Electrooptics Europe*, 1 (2000).

[86] H. Liu, J. Ness, G. Mourou, G. J. Spuhler, U. Keller and N. V. Kuleshov, *Conference on Lasers and Electrooptics*, **1,** 554 (2001).

[87] H. Liu, J. Ness and G. Mourou, *Conference on Lasers and Electrooptics, Postconference Technical Digest*, 335 (2001).

[88] S. Erhard, J. Gao, A. Giesen, K. Contag, A.A. Lagatsky, A. Abdolvand, N. V. Kuleshov, J. Aus der Au, G.J. Spuhler, F. Brunner, R. Paschotta and U. Keller, *Conference on Lasers and Electrooptics, Postconference Technical Digest*, 333 (2001).

[89] H. Liu, J. Ness and G. Mourou, *Conference on Lasers and Electrooptics, Postconference Technical Digest*, 30 (2001).

[90] A. Courjaud, N. Deguil and F. Salin, *Conference on Lasers and Electrooptics*, **1,** 501 (2002).

[91] P. Klopp. V. Petrov, U. Griebner and G. Erbert, *Opt. Express*, **10**, 108 (2002).

[92] A. S. Grabtchikov, A. N. Kuymin, V.A. Lisinetskii, V.A. Orlovich, A.A. Demidovich, M.B. Danailov, h.J. Eichler, A. Bednarkiewicz, W. Strek and A. N. Titov, *App. Phys. B.*, **B75**, 795 (2002).

[93] A. Courjaud, R. Maleck-Rassoul, N. Deguil, C. Honninger and F. Salin, *Conference on Lasers and Electrooptics*, **1,** 62 (2002).

[94] P. Klopp, V. Petrov, U. Griebner, V. Nikolov, V. Nesterenko and T. Kirilov, *Conference on solid State Laser XII, Proc. SPIE* **4968**, 46 (2003).

[95] B.Z. Malkin, A.A. Kaminskii, N.R. Agamalyan, L.A. Bumagina and T.I. Butaeva, *Phys. Status Solidi B*, **110**, 417 (1982).

[96] A.A. Kaminskii, A.A. Pavlyuk, P.V. Kletsov, I. F. Balashov, V. A. Berenberg, S. E. Sarkisov, V. A. Fedorov, M. V. Petrov and V.V. Lyubchenko, *Izv. Akad. Nauk SSSR , Neorg. Mat* **13**, 582 (1997).

[97] A. Kaminskii, A.A. Pavlyuk, T. I. Butaeva, V. A. Fedorov, I. F. Balashov, V. A. Berenberg and V.V. Lyubchenko, *Izv. Akad. Nauk SSSR , Neorg. Mat* **13**, 1541 (1997).

[98] A. A. Kamiskii, A.A. Pavlyuk, N.R. Agamalyan, L.I. Bobovich, A. V. Lukin and V.V. Lyubchenko, *Inorg. Mat.* **15**, 1182 (1979).

[99] N.V. Kuleshov, A.A. Lagatsky, V.G. Shcherbitsky, V. P. Mikhailov, E. Heumann, T. Jensen, A. Diening and G. Huber, *Appl. Phys. B*, **64**, 409 (1997).

[100] N.V. Kuleshov, A.A. Lagatsky, A.V. Podlipensky, V.P. Mikhailov, A.A. Kornienko, E.B. Dunina, S. Hartung and G. Huber, *J. Opt. Soc. Am.*, **15**, 1205 (1998).

[101] A. Majchrowski, Z. Mierczyk, K. Kopczynski, E. Michaski, M. Kwasny and J. Zmija, *Conference on Lasers and ElectroOptics (CLEO)* Poster Session, (2003).

[102] D. Elwell and H.J. Scheel, 1975. *Crystal growth from high-temperature solutions*. Academic Press.

[103] D.T.J. Hurle, 1994. *Handbook of crystal growth. Bulk crystal growth. 2a Basic Techniques*. Elsevier.

[104] D.T.J. Hurle, 1994. *Handbook of crystal growth. Bulk crystal growth. 2b Basic Techniques*. Elsevier.

[105] S.J.B. Reed, 1993. *Electron Microprobe Analysis*. Cambridge University Press.

[106] Michael M. Woolfson, second edition, 1997. *An introduction to x-ray crystallograpy*. Cambridge University Press.

[107] B.D. Cullity, 1978. *Elements of X-ray diffraction*. Addison-wesley publishing.

[108] J.F. Nye, 1985. *Physical Properties of Crystals*, Oxford: Clarendon.

[109] Tso Yee Fan, C.E. Huang, B.Q. Hu, R.C. Eckanrdt, Y.X. Fan, Robert L. Byer and R.S. Feigelson, *Appl. Opt.* **26**, 2390 (1987).

[110] P. Klopp, V. Petrov, U. Griebner, and G. Erbert, *Opt. Exp.* **10**, 108-113 (2002).

[111] P.V. Kletsov, L.P. Kozeeva, L. Yu, Kharchenko, A.A. Pavlyuk, *Kristallografiya* **19**, 552 (1974).

[112] V.I. Spitsyn, V.K. Trunov, *Dokl. Akad. Nauk SSSR* **183**, 129 (1968).

[113] P.V. Klevtsov, R.F. Klevtsova, *Zh. Strukt. Khim*. **18**, 419 (1977).

[114] P.V. Kletsov, L.P. Kozeeva, L. Yu, Kharchenko, *Sov. Phys. Crystallogr.* **20**, 732 (1976).

[115] C. Tu, Y. Huang, Z. Luo and G. Chen, *J. Crystal Growth* **135**, 636 (1994).

[116] G. Metrat, N. Muhlstein, A. Brenier and G. Boulon, *Opt. Mat.* **8**, 5 (1997).

[117] R.J.H. Gelsing, *Rec. Trav. Chim. Pays-Bas Belg.* **84**, 1452 (1965).

[118] P. Caillet, *Bul. Soc. Chim. Fr.*, **12**, 4750 (1967).

[119] R. Guerin, P. Caillet, *ACC Fig.* 4274, 85 (1970).

[120] G. Wang and Z. Luo, *J. Cryst. Growth*, **102**, 765 (1990).

[121] G. Wang and Z. Luo, *J. Cryst. Growth*, **116**, 505 (1992).

[122] C. Tu, Z. Luo, G. Chen, T. Zhao, *J. Crystal Growth* **152**, 235 (1995).

[123] R. Guerin, P. Caillet, *C.R. Acad. Sci*. **271C**, 815 (1970).

[124] R. Solé, V. Nikolov, X. Ruiz, Jna. Gavaldà, X. Solans, M. Aguiló and F. Díaz, *J. Cryst. Growth.*, **169**, 600 (1996).

[125] M .C. Pujol, R. Solé, J. Masons, Jna. Gavaldà, X. Solans, C. Zaldo, F. Díaz and M. Aguiló, *J. Appl. Cryst.* **34**, 1 (2001).

[126] L. I. Yudanova, O. G. Potapova, and A. A. Pavlyuk, *Inorg. Mat.* **23**, 1657-1660 (1987), [transl. from *Izv. Akad. Nauk SSSR, Neorg.Mat.* **23**, 1884-1887 (1987)].

[127] Mironov, V.S. & Li, L.E. *J. of Alloys and Compounds*, **279**, 83 (1998).

[128] S. V. Borisov and R.F. Kletsova, *Soviet Phys. Cryst.*, **13**, 420 (1968), [transl. from *Kristallografiya*, **13**, 517 (1968)].

[129] J. Rodriguez-Carvajal. Fullprof. Laboratoire Leon Brillouin (CEA-CNRS) Centre d'Etudes de Salley 91191 Gif-Sur-Yvette Cedex (France), 1996.

[130] C. Pujol, M. Aguiló, F. Díaz and C. Zaldo, *Opt. Mat.* **13**, 33 (1999).

[131] M.C. Pujol, M. Rico, C. Zaldo, R. Solé, V. Nikolov, X. Solans, M. Aguiló and F. Díaz, *Appl. Phys. B.*, **68**, 187 (1999).

[132] N. Weinstock, H. Shulze and A. Müller. *J. Chem. Phys.*, **59**, 5063 (1973).

[133] I.V. Mochalov, *J. Opt. Tech.*, **62**, 746 (1995).

[134] N. H. Hartshorne and A. Stuart, 1970. *Crystals and the Polarising Microscope* London: Arnold.

[135] B. M. Ayupov, V. I. Protasova, A. A. Pavlyuk and L. Yu. Kharchenko, *Izv. Akad. Nauk SSSR, Neorg. Mater*, **22**, 1156 (1986).

[136] N. Manuilov, V. Nikolov, G. Gentscheva, P. Peshev, *J Cryst. Growth*., **196**, 181 (1999).

[137] M.C. Pujol. 2000. *Doctoral Thesis. Obtenció i caracteritzacio de cristalls monoclinics de* $KGd(WO_4)_2$ *substituits amb lantànids.*

[138] F. D. Patel, E. C. Honea, J. Speth, S. A. Payne, R. Hutcheson, and R. Equal, *IEEE J. Quantum Electron*. **37**, 135 (2001).

[139] A. A. Lagatsky, N. V. Kuleshov, V. P. Mikhailov, *Opt. Commun.* **165**, 71 (1999).

[140] N. V. Kuleshov, A. A. Lagatsky, A. V. Podlipensky, V. P. Mikhailov, and G. Huber, *Opt. Lett*. **22**, 1317 (1997).

[141] V. V. Ovsyankin, A. A. Kaplyanskii, R. M. Macfarlane (eds.), 1987. *Spectroscopy of solids containing rare earth ions*, Elsevier, Amsterdam.

[142] A. Lupei, V. Lupei, V. N. Enaki, C. Presura, A. Petraru, *Spectrochim. Acta A* **55A**, 773 (1999).

[143] L. D. Deloach, S. A. Payne, L. L. Chase, L. K. Smith, W. L. Kway, and W. F. Krupke, *IEEE J. Quantum Electron.* **29**, 1179 (1993).

[144] D. S. Sumida and T. Y. Fan, *Opt. Lett.*, **19,** 1343 (1994).

[145] H. P. Christensen, Dr. R. Gabbe andH. P. Jenssen, *Phys. Rev. B*, **25**, 1467 (1982).

[146] M. P. Hehlen, *J. Opt. Soc. Am. B*. **14,** 1312 (1997).

[147] B.R. Judd. *Phys. Rev*. **127**, 750 (1962).

[148] G.S. Ofelt. *J. Chem. Phys.* **37**, 511 (1962).

[149] M. C. Pujol, X. Mateos, R. Solé, J. Massons, Jna. Gavaldà, X. Solans, F. Díaz and M. Aguiló. *J. Appl. Cryst.* **35**, 108-112 (2002).

[150] A.A. Kaminskii, 1996. *Crystalline lasers: Physical Processes and Operating Schemes* CRC Press.

[151] P. Klopp, V. Petrov and U. Griebner, *Jpn. J. Appl. Phys.*, **42**, L246 (2003).